2023

Phenomenology from Lattice Field Theory Simulations

Sinha Ray, Gaurav

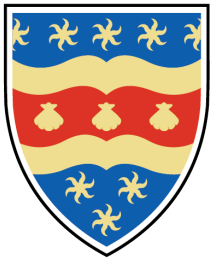

UNIVERSITY OF
PLYMOUTH

Phenomenology from Lattice Field Theory Simulations

by

Gaurav Sinha Ray

A thesis submitted to the University of Plymouth
in partial fulfilment for the degree of

DOCTOR OF PHILOSOPHY

School of Computing, Electronics and Mathematics

January 2023

Acknowledgements

Four years is a long time to spend on a single body of work, and while there is a certain allure to being able to claim that my development as a researcher is the result of my hard work alone, that would be untrue and a disservice to many friends and colleagues. There are many people I must thank for their support, in big ways and small, directly and indirectly, during my time at the University of Plymouth.

Conversations and emails with other members of the Theoretical Physics group have directly helped my understanding of some of the topics mentioned in this thesis. I should like to thank Vincent and Antonio in particular for their support and advice. Special mention must go to the other former and current PhD students, Lauren, Laurence, and Steph, with whom I feel a certain comradeship. Thank you to Argia for helping with the proofreading of the first two chapters, and to James and Martin for career advice and other insights.

I also should thank the various inhabitants of 22 Bedford Park, over the years they provided me much needed respite from the academic grind, particularly during the long months of lockdown. Thank you to my friends and family for always being there for me, particularly my parents for putting a roof over my head for the past few months as I have been completing this thesis.

Lastly, but absolutely not leastly, I must thank my supervisor Dr Craig McNeile. By his example I now understand what it means to research a topic as a theoretical physicist. If I can now say that I am a physicist, it is in large part because of his patience and encouragement over the past four years.

Author's Declaration

At no time during the registration for the degree of Doctor of Philosophy has the author been registered for any other University award.

Work submitted for this research degree at the University of Plymouth has not formed part of any other degree either at the University of Plymouth or at another establishment.

Publications:

Determination of hybrid charmonium meson masses
Gaurav Ray and Craig McNeile
PoS LATTICE2021 (2022) 240

Presentations at conferences:

Determination of hybrid charmonium meson masses
38th International Symposium on Lattice Field Theory
July 2021

Calculating the QED correction to the hadronic vacuum polarisation on the lattice
39th International Symposium on Lattice Field Theory
August 2022

Word count of main body of thesis: 22,863

Signed.....  .....

Date.....31/01/2023.....

Phenomenology from Lattice Field Theory Simulations

Gaurav Sinha Ray

Abstract

Lattice QCD is a well-established *ab initio* probe of the Strong interaction in the low energy nonperturbative regime. As a systematically improvable numerical tool it has proven an effective means of validating the Standard Model against observations from particle physics experiments. In this thesis two topics of phenomenological importance are studied on lattices generated with the $N_f = 2+1+1$ Highly Improved Staggered Quark action, the spectroscopy of hybrid charmonium mesons, and the hadronic vacuum polarisation.

Chapters 1 and 2 serve as a brief introduction to the lattice and provide the relevant background on the theoretical concepts. Basic ingredients such as the discretisation of QCD, the Staggered fermion formulation, and the latticisation of QED are described. The procedure for generating gauge fields and measuring correlators is outlined and the statistical concepts behind the extraction of physical information from the correlators are explained.

Over the last two decades many resonances have been observed that do not fit within the longstanding Quark Model. Hybrid mesons ($q\bar{q}g$), mesons with an excited gluonic component, have been proposed as part of the solution to this mismatch. Chapter 3 describes the construction and study of hybrid mesons in the charmonium sector on the lattice. Results are presented for the mass of the $J^{PC} = 1^{-+}$ state at multiple lattice spacings, and the mass and decay constant of the $J^{PC} = 1^{--}$ state at one lattice spacing.

In the decade since the discovery of the Higgs boson few signs of beyond the SM physics have been observed. Of those the anomalous magnetic moment of the muon has garnered the most attention. Chapter 4 describes work done to include the effects of quenched QED on the leading order hadronic vacuum polarisation contribution to the anomaly. Blinded results for the QED corrections to the light and strange connected hadronic vacuum polarisation are presented.

Contents

List of Figures

List of Tables

Chapter 1

Quantum Field Theories on the Lattice

In this chapter and the next we review the concepts that form the basis of the results described in chapters 3 and 4 of this work. We highlight relevant elements of the Standard Model (SM) of particle physics and describe how gauge theories, Quantum Chromodynamics (QCD) in particular, are put on the lattice. The doubling problem arising from the transition to the lattice is described and used to motivate the different ways in which fermions can be put on the lattice. The staggered transformation is defined and its consequences are discussed. We also discuss some aspects of renormalisation of QFTs on the lattice. We end with a brief overview of the different ways that QED can be put on the lattice, and introduce the $\mathrm{QED_L}$ formulation.

The material in this chapter is by no means original and more detailed expositions can be found in the literature [1, 2, 3, 4, 5].

1.1 QCD on the Lattice

The SM of particle physics is our current best description of the ordinary matter that makes up the universe and the forces (excluding gravity) that mediate their interactions. Developed during the second half of the twentieth century to explain the 'particle zoo' uncovered at various colliders, it has remained remarkably resilient to new experimental particle data. Nevertheless we are confident that a theory exists which will supersede the SM and explain phenomena such as dark matter and dark energy, for which there is plentiful cosmological evidence [6, 7, 8, 9]. The work in this thesis has as its broad aim the testing of one part of the SM, QCD, in order to tease out possible discrepancies between the SM and the real world, and point us towards an improved theory of nature.

QCD, developed during the 60's and 70's, is one of the pillars of the SM, describing the Strong force in terms of quarks and gluons [10, 11, 12, 13, 14, 15]. QCD is a Yang-Mills theory with non-abelian gauge group SU(3). The quarks are spin-1/2 matter fields, represented by Dirac spinors, ψ, in the fundamental representation of SU(3). They have a colour charge under SU(3), and an electric charge under U(1). The gluons have a colour charge and are massless neutral gauge bosons that mediate the strong interactions between the quarks. The quarks come in six flavours, $\{u, d\}\{s, c\}\{b, t\}$, of varying masses arranged into three generations, see table 1.1. The u, d, s quarks are referred to as the light quarks and the c, b, t are referred to as the heavy quarks.

The QCD Lagrangian is

$$\mathcal{L}_{\text{QCD}} = \overline{\psi}\left(i(\gamma^{\mu}D_{\mu}) - m\right)\psi - \frac{1}{4}G^{a}_{\mu\nu}G^{\mu\nu}_{a} \tag{1.1}$$

where $\psi, \overline{\psi}$ are the quark and antiquark fields respectively, and $G^{a}_{\mu\nu}$ is the SU(3) field strength tensor formed from the gluon fields A^{a}_{μ} and labelled with a colour index, a. The gauge covariant derivative, $D_{\mu} = \partial_{\mu} - igA^{a}_{\mu}T^{a}$, where T^{a} are the generators of SU(3) in the fundamental representation, sets the strength of the quark-gluon coupling via g. The last term of equation 1.1 encodes the fact that gluons have colour charge and so may self-interact, in contrast to the electrically neutral photons.

flavour	mass (MeV)	charge (e)
up (u)	2.16(49)	2/3
down (d)	4.67(48)	-1/3
strange (s)	93.4(8.6)	-1/3
charm (c)	$1.27(2)\times10^{3}$	2/3
bottom (b)	$4.18(3)\times10^{3}$	-1/3
top (t)	$172.69(30)\times10^{3}$	2/3

Table 1.1: The masses and electric charges of the quarks of the SM. Quark masses are in the $\overline{\text{MS}}$ scheme. The light quark masses are at a scale of $\mu = 2$ GeV, the c, b quark masses are evaluated as $m_q(\mu = m_q)$, and the t quark mass is measured directly [16].

The extra non-abelian term gives rise to the phenomenon of Asymptotic freedom. Asymptotic freedom is used to describe the fact that the coupling strength is small over short distances (or equivalently large energies) and grows as the distance increases (or the energy decreases) [13, 14]. This means perturbative expansions in the coupling break down at distances $\sim$1 fm.

The Strong interactions dynamically generate a characteristic energy scale, $\Lambda_{\mathrm{QCD}} \sim 200$ MeV, at and below which nonperturbative effects are expected to dominate. Behaviour like hadron formation is nonperturbative in nature, so theoretical methods that work in this regime are crucial for validating and understanding QCD.

Wilson showed how to put QCD on a discrete spacetime lattice while preserving gauge invariance in 1974 [17]. In Wilson's formulation quarks live on the sites of the lattice and gluons are associated with gauge fields that link adjacent sites of the lattice, see figure 1.1. The lattice acts as a regulator, imposing a UV cutoff, and thus makes the necessary integrals calculable. In practice these computations have to be carried out on High Performance Computing (HPC) clusters. The first numerical calculations were carried out by Creutz in 1980 (in SU(2) though, not SU(3)) [18]. In the intervening years huge strides have been made, algorithmically, computationally, theoretically, to bring the calculations closer to the real world. Lattice QCD is an important tool because it is an *ab-initio* nonperturbative probe of QCD.

1.1.1 Path Integral Formulation of QCD

Lattice QCD calculations are a nonperturbative implementation of QCD using Feynman's path integral approach. In a continuum gauge theory the basic object in the path integral approach is the partition function $\mathcal{Z}$, which is given by a functional integral over configuration

space,

$$\mathcal{Z} = \int \mathcal{D}A\mathcal{D}\psi\mathcal{D}\overline{\psi}\; e^{-S}, \tag{1.2}$$

where the A are the gauge fields, ψ are the fermion fields, and S is the QCD action in Euclidean coordinates.

S can be split into a gauge part and a fermion part, $S = S_G + S_F$. Since $\psi, \overline{\psi}$ are Grassmann-valued fields they can be integrated out, leaving only an integral over background gauge configurations,

$$\mathcal{Z} = \int \mathcal{D}A\ \mathrm{det}M\ e^{-S_G}, \tag{1.3}$$

in which the fermionic contribution $\mathrm{det}M$ is highly non-local. Taking this determinant into the exponential we can write the action as

$$S = S_G + S_F = \int d^4x\ \frac{1}{4}F_{\mu\nu}F^{\mu\nu} - \sum_i \log\det M_i, \tag{1.4}$$

where i labels the quark flavour and $F_{\mu\nu}$ is the field strength tensor in Euclidean spacetime.

What we are generally interested in calculating are expectation values of operators, $\mathcal{O} = \mathcal{O}[A, \psi, \overline{\psi}]$, that can be any combination of time-ordered products of gluon and quark fields. In the path integral approach these expectation values are integrals of $\mathcal{O}$ over the gauge fields, weighted by a Boltzmann factor, e^{-S_G},

$$\langle\mathcal{O}\rangle = \frac{1}{\mathcal{Z}}\int \mathcal{D}A\ \mathrm{det}M\mathcal{O}e^{-S_G}. \tag{1.5}$$

If the action is in Minkowski spacetime the Boltzmann factor is in-

stead a phase factor, e^{iS}. The presence of an oscillating exponential, also called the sign problem, makes numerical evaluation of the path integral very difficult. This is why lattice QCD calculations are done in Euclidean spacetime.

The Euclidean theory is connected to the Minkowski theory by analytic continuation,

$$\begin{aligned} x_0 \equiv t &\to -i\tau \\ p_0 \equiv E &\to ip_4, \end{aligned} \tag{1.6}$$

where τ, p_4 are the Euclidean time and energy, and this transformation is referred to as a Wick rotation. This name comes from the clockwise rotation by $\pi/2$ radians in the complex plane caused by multiplication by $-i$.

1.1.2 Discretising the Gluon action

On the lattice we must discretise equation 1.5, we consider the gauge action first. Wilson was motivated by the idea of a gauge field as a path-dependent phase factor. In his formulation the degrees of freedom are group elements associated with straight-line paths between adjacent lattice sites. The group element associated to an extended path through the lattice is equal to the product of the individual links along the path. We write the basic link fields like so,

$$U_{x,\mu} = \exp\left(iagA^c_{x,\mu}T_c\right), \tag{1.7}$$

where it is understood that the link field $U_{x,\mu}$ joins the adjacent lattice points $x, x + \hat{\mu}$. Observing that the non-abelian field strength is a

generalised curl of the potential, suggesting integrals of A_μ around small closed contours, Wilson proposed the following lattice gauge action,

$$S_G[U] = \frac{2}{g^2} \sum_{\text{plaquettes}} \text{Re Tr}[1 - P_{\mu\nu}(n)], \tag{1.8}$$

where $P_{\mu\nu} = U_{x,\mu} U_{x+\hat{\mu},\nu} U^\dagger_{x+\hat{\nu},\mu} U^\dagger_{x,\nu}$ are oriented products of closed gauge loops called plaquettes, see figure 1.1.

Under a local gauge transformation the link fields transforms like so

$$U_{x,\mu} \to V_x U_{x,\mu} V^\dagger_{x+\mu}, \tag{1.9}$$

where the V are SU(3) fields, same as the link fields. From this definition it is easy to show that the $P_{\mu\nu}$ are gauge invariant objects. This important property of the plaquette is inherited by Wilson's lattice action, and is the main symmetry preserved in the lattice discretisation procedure.

By expanding equation 1.7 in the lattice spacing one can show that equation 1.8 reduces to the gluon part of the QCD action in the $a \to 0$ limit.

1.1.3 Discretising the Dirac action

In the continuum the action for a free fermion, mass m, is

$$S = \int d^4x \ \left(\overline{\psi}(x) \gamma^\mu \partial_\mu \psi(x) + m \overline{\psi}(x) \psi(x) \right). \tag{1.10}$$

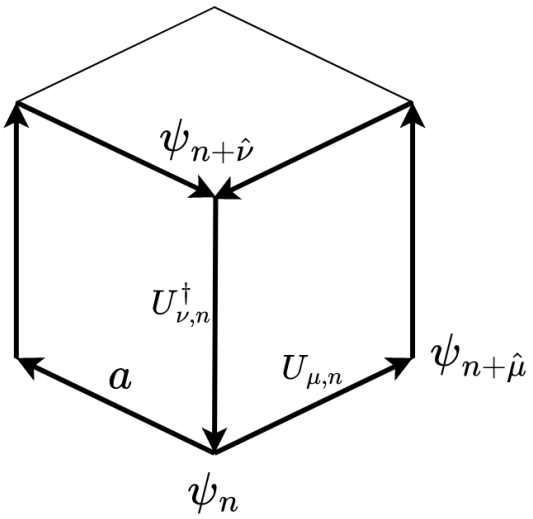

Figure 1.1: Unit cell of a cubic lattice with spacing a. The quark, and gluon fields are labelled by their positions. The gluon link fields are represented by arrows and are also labelled by their direction.

Moving from the continuum to discrete spacetime on a lattice requires that derivatives are replaced by finite differences,

$$\partial_\mu \psi(x) \to \frac{1}{2a}[\psi(x + a\hat{\mu}) - \psi(x - a\hat{\mu})], \tag{1.11}$$

and integrals are replaced by sums over lattice points, $\int d^4x \to \sum_x$, leaving the action

$$S = -\frac{1}{2a}\sum_{x,\mu}[\overline{\psi}(x)\gamma^\mu\psi(x + a\hat{\mu}) - \overline{\psi}(x)\gamma^\mu\psi(x - a\hat{\mu})] + \sum_x m\overline{\psi}(x)\psi(x). \tag{1.12}$$

With a suitable redefinition the fermion fields can be made dimensionless, $\psi_n = a^{3/2}\psi(x)$, where now the subscript n labels points on the lattice. Inserting gauge links, $U_{\mu,n}$, to connect neighbouring sites and preserve gauge invariance we arrive at the discretised action in

Euclidean spacetime,

$$S = -\frac{1}{2a}\sum_{n,\mu}[\overline{\psi}_n\gamma_\mu U_{\mu,n}\psi_{n+\hat{\mu}} - \overline{\psi}_n\gamma_\mu U^\dagger_{\mu,n}\psi_{n-\hat{\mu}}] + \sum_n m\overline{\psi}_n\psi_n. \quad (1.13)$$

Gauge-invariant objects may be formed either through closed loops of link fields, such as plaquettes, or a quark-antiquark pair connected by links.

The top quark, the most massive quark, is never included in lattice simulations because it is too massive. In any case, the top is phenomenologically irrelevant as it decays weakly before it can hadronise. The other heavy quarks, the charm and bottom, have discretisation errors of $\mathcal{O}(am_q)$, leading to large errors on typical lattices where $2\text{ GeV} \leq 1/a \leq 5\text{ GeV}$. The bottom quark is usually omitted from lattice simulations because of its large mass. Only on very fine ensembles, not available till very recently, is $am_b \lesssim 1$ and simulation directly at the physical bottom quark mass possible [19].

1.1.4 The doubling problem

The free fermion propagator obtained by a Fourier transform is

$$S(p) = \begin{cases} a(i\gamma_\mu \sin p_\mu a + am)^{-1} & \text{on the lattice,} \\ (i\gamma_\mu p_\mu + m)^{-1} & \text{in the continuum.} \end{cases} \quad (1.14)$$

The lattice spacing acts as a UV cutoff with lattice momenta restricted to $p_\mu \in [\frac{-\pi}{a}, \frac{\pi}{a}]$. The continuum fermion propagator is large around small values of p. In contrast, because of the periodic sine function, the

lattice fermion propagator is large not only when $ap \sim (0,0,0,0)$, but also $(\pi,0,0,0),(0,\pi,0,0)\ldots(\pi,\pi,\pi,\pi)$. These 16 momenta occupy the corners of the Brillouin zone associated with the lattice, and are associated to 16 fermions. This unwanted multiplicity, 16 instead of 1, of fermions brought about by the discretisation process is called the 'doubling problem' [20].

One solution is to ignore this artefact of the lattice and say that the theory automatically generates multiple fermion 'flavours'. Real quarks do come in several flavours but it does not seem credible to have them generated as a byproduct of lattice discretisation. Many different ways of solving the doubling problem have been developed by lattice theorists and we shall now briefly mention some of these solutions before focusing on the staggered fermion formulation.

Wilson's method works by adding a momentum dependent mass term, which disappears in the continuum limit to the action, which raises the masses of the unwanted doublers to the order of the cutoff, thereby suppressing those states [21]. As originally proposed by Wilson this term was $\sim \overline{\psi} D^2 \psi$ in the free theory. The propagator of the modified action then becomes

$$\frac{1}{a}S(p) = \left(i\gamma_\mu \sin p_\mu a + am + r\sum_\mu (1-\cos p_\mu a) \right)^{-1}, \qquad (1.15)$$

where r is generally chosen to be 1. Close to zero momentum the (1-cos) term vanishes and we recover the usual lattice propagator. When $ap_\mu \sim \pi$, corresponding to the unwanted doublers, the cosine term increases the mass by $2r/a$. As $a \to 0$ these masses go to infinity with

only the $ap_\mu = 0$ species, mass m, surviving.

While this is a simple method that is convenient for calculation, a significant drawback is the destruction of the chiral symmetry of the action. Intuitively this is because the added term is like a mass term for the unwanted fermions.

There are deep connections between the doublers and chiral symmetries of the action, via the anomaly. However this would be straying beyond the scope of this work and so it suffices to mention that there is a famous 'no-go' theorem by Nielsen and Ninomiya that describes when a lattice fermion action can be undoubled, chiral, and local [22].

Other fermion formulations on the lattice, the domain-wall and overlap fermions, preserve exact chiral symmetry with the drawback of relatively expensive simulations [23, 24, 25, 26].

1.2 Staggered Quarks

Staggered fermions have a rich and storied history in the field of LQCD [27, 28, 29, 30, 31, 32, 33, 34]. It was observed that the doubling problem may be ameliorated by defining the following local 'staggering' transformation,

$$\begin{aligned} \psi_n &\longrightarrow \Omega_n \psi'_n \\ \overline{\psi}_n &\longrightarrow \overline{\psi}'_n \Omega_n^\dagger \end{aligned} \tag{1.16}$$

where the 16 staggering matrices Ω_n are defined as

$$\Omega_n = \gamma_0^{n_0} \gamma_1^{n_1} \gamma_2^{n_2} \gamma_3^{n_3} \,. \tag{1.17}$$

From the rules of the γ algebra one can show that $\Omega_n^\dagger \Omega_n = 1$, and that

$$\Omega_n^\dagger \gamma_\mu \Omega_{n+\hat{\mu}} = (-1)^{n_0+n_1+\cdots+n_{\mu-1}} \equiv \theta_\mu(n), \tag{1.18}$$

allowing us to write S_F, equation 1.10, like so,

$$S_F = \frac{1}{2a} \sum_{n,\mu} \overline{\psi}'_n \theta_\mu(n) (U_\mu(n) \psi'_{n+\hat{\mu}} - U_\mu^\dagger(n-\hat{\mu}) \psi'_{n-\hat{\mu}}) + m \sum_n \overline{\psi}'_n \psi'_n, \tag{1.19}$$

with the phase $\theta_\mu(n)$ inserted. The absence of the γ matrices mean this action is diagonal in spinor space, with the four components of the spinor ψ'_n independent and identical in form. Therefore we may get rid of any three of the components of ψ'_n, and call the resulting one-component field χ_n the staggered field with one-component action

$$\begin{aligned} S &= \frac{1}{a} \overline{\chi} M(U) \chi \\ &= \frac{1}{2a} \sum_{n,\mu} \overline{\chi}_n \theta_\mu(n) (U_\mu(n) \chi_{n+\hat{\mu}} - U_\mu^\dagger(n-\hat{\mu}) \chi_{n-\hat{\mu}}) + m \sum_n \overline{\chi}_n \chi_n. \end{aligned} \tag{1.20}$$

By this transformation we have reduced the number of doublers by a factor of four, from sixteen to four. The four remaining doublers are referred to as 'tastes'. A single staggered fermion corresponds to four tastes of continuum fermions.

From equation 1.18 it is useful to define $x_\mu^< = \sum_{\nu<\mu} x_\nu$ such that the phase $\theta_\mu(n) = (-1)^{x_\mu^<} = \pm 1$ depending on whether $x_\mu^<$ is even or odd. This suggests the 2^4 hypercube as the natural unit cell of the staggered fermion field.

The one-component staggered action (1.20) is invariant, at zero

quark mass, under a modified U(1) chiral transformation,

$$\begin{aligned} \chi &\longrightarrow e^{i\Gamma_5\theta}\chi \\ \overline{\chi} &\longrightarrow \overline{\chi}e^{i\Gamma_5\theta}, \end{aligned} \tag{1.21}$$

where Γ_5 is diagonal in the site and colour indices and depends on the evenness of $\sum_\mu n_\mu$,

$$\Gamma_{5,n} = \begin{cases} +1, & n \text{ even} \\ -1, & n \text{ odd.} \end{cases} \tag{1.22}$$

At non-zero mass the action satisfies,

$$M^\dagger(U) = \Gamma_5 M(U) \Gamma_5. \tag{1.23}$$

This remnant chiral symmetry of the staggered action produces a natural Goldstone boson and enforces multiplicative quark mass renormalisation. The spectrum of $M^\dagger M$ is bounded from below by $(am)^2$, so that staggered simulations at small quark mass are not as costly as with other actions. In fact staggered simulations were the first to be done at pion masses close to the physical point [35].

1.2.1 Taste breaking effects

Each flavour of quark carries four tastes. Taste is an unphysical quantum number. Different tastes of quark have the same mass, whereas different flavours do not. However mathematically taste and flavour can be described with the same algebra and so we may use γ matrices to describe taste assignments as well. A unitary change of basis helps

us see this clearly. Label the sixteen sites of the hypercube with four component vectors η with $\eta_\mu = 0$ or 1. We define a four-taste Dirac field, ψ,

$$\psi_y^{\alpha,t} = \frac{1}{8}\sum_\eta \Omega_\eta^{\alpha,t}\chi_{2y/t+\eta}, \tag{1.24}$$

where α labels the four spinor components, t the four taste components. ψ lives on the hypercube with origin at $2y$. In this new spin-taste basis the action becomes,

$$S = \sum_{y,\mu} b^4\overline{\psi}_y[(\gamma_\mu \otimes I)\Delta_\mu + \frac{1}{2}b(\gamma_5 \otimes \gamma_\mu^*\gamma_5)\Box_\mu]\psi_y + mb^4\sum_y \overline{\psi}_y(I\otimes I)\psi_y \tag{1.25}$$

where, the difference operators are defined as

$$\begin{aligned}\Delta_\mu\psi_y &= \frac{1}{2b}(\psi_{y+b\hat{\mu}} - \psi_{y-b\hat{\mu}}) \\ \Box_\mu\psi_y &= \frac{1}{b^2}(\psi_{y+b\hat{\mu}} - 2\psi_y + \psi_{y-b\hat{\mu}}),\end{aligned} \tag{1.26}$$

and we use the tensor product notation, (spin $\otimes$ taste), to make explicit the taste content of the operators in the action.

Equation 1.25 can be written in a way that makes clear the first order taste breaking contribution contains fermion bilinears of dimension five, so that even in the interacting theory only irrelevant operators break the taste symmetry. The most obvious effect of this taste symmetry breaking is the splitting of the pion mass spectrum according to taste, with the $\gamma_5 \otimes \gamma_5$ pion being the lightest of the taste multiplet.

1.2.2 Highly Improved Staggered Quarks

All lattice actions that lie in the same universality class as the desired action will describe the same physics in the limit of zero lattice spacing. At non zero lattice spacing scaling violations will break the universality with different lattice actions having discretisation effects that scale differently. Clearly the smaller these scaling violations are the coarser the lattices one can use and the more desirable the action. Given a particular lattice action, Symanzik showed how to systematically improve the action through the addition of irrelevant operators with coefficients chosen so as to cancel the lowest order lattice artefacts [36, 37]. These extra terms vanish in the continuum limit and so don't change the physical content of the theory. The coefficients must be determined, either perturbatively or non-perturbatively, by reference to some condition, and the cost of the simulation will increase.

Having seen how the naive staggered action is formulated we will now recount how the HPQCD collaboration used perturbative Symanzik improvement to create a new staggered quark action with greatly reduced discretisation effects [38]. The resulting $\mathcal{O}(a^2)$ improved action, meaning there are no tree level $\mathcal{O}(a^2)$ discretisation errors, is called the Highly Improved Staggered Quark, or HISQ, action, and is the workhorse behind the results described in this thesis.

There are two sources of $\mathcal{O}(a^2)$ discretisation errors in the naive staggered action; the finite difference approximation to the derivatives, and taste-exchange interactions between quarks. In the late 80s Naik [39] had shown that the accuracy of the finite difference approximation

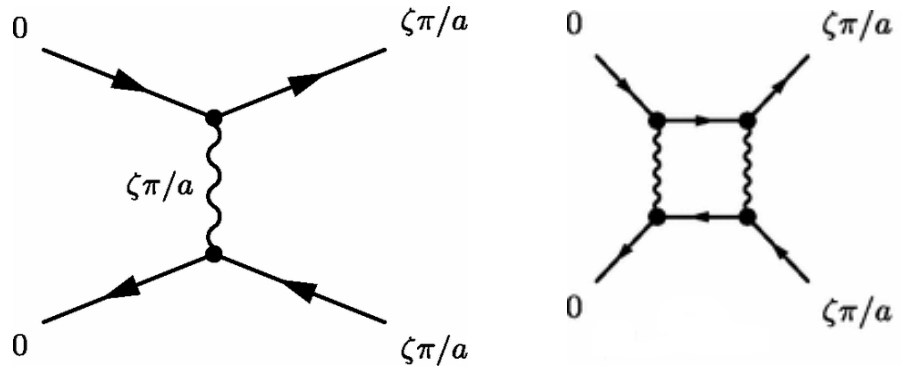

Figure 1.2: Tree level and 1-loop taste-exchange Feynman diagrams.

can be improved by adding a ('Naik') term to the usual expression

$$\Delta_\mu \to \Delta_\mu - \frac{a^2}{6}\Delta_\mu^3 \,. \tag{1.27}$$

The $\mathcal{O}(a^2)$ discretisation errors coming from taste-exchange interactions, see figure 1.2, were not fully appreciated until the late 90s when it was realised that smearing the gauge links could suppress these diagrams. Because of the doubled nature of the staggered action two low momentum quarks can exchange a highly virtual gluon ($p \sim \pi/a$) with the result still being two low momentum quarks but now with different tastes. An improvement program could proceed by adding four quark operators to the action to cancel these diagrams.

HPQCD took a simpler approach, effectively introducing into the gluon-quark vertex a form factor that vanishes for gluons with momenta in the corners of the Brillouin zone. Such a form factor can be introduced by smearing the gauge fields in the action with

$$\mathcal{F}_\mu \equiv \prod_{\rho\neq\mu}\left(1+\frac{a^2\delta_\rho^{(2)}}{4}\right)\Bigg|_{\text{symm.}} \tag{1.28}$$

where $\delta_\rho^{(k)}$ approximates the covariant kth derivative. $\delta_\rho^{(2)}$ and $\delta_\rho^{(1)}$ are

given by

$$\begin{aligned}
\delta^{(1)}_{\rho} U_{\mu}(x) \equiv \frac{1}{a}\Big(& U_{\rho}(x)\, U_{\mu}(x + a\hat{\rho})\, U^{\dagger}_{\rho}(x + a\hat{\mu}) \\
& - U^{\dagger}_{\rho}(x - a\hat{\rho})\, U_{\mu}(x - a\hat{\rho})\, U_{\rho}(x - a\hat{\rho} + a\hat{\mu})\Big) \\
\delta^{(2)}_{\rho} U_{\mu}(x) \equiv \frac{1}{a^2}\Big(& U_{\rho}(x)\, U_{\mu}(x + a\hat{\rho})\, U^{\dagger}_{\rho}(x + a\hat{\mu}) \\
& - 2U_{\mu}(x) \\
& + U^{\dagger}_{\rho}(x - a\hat{\rho})\, U_{\mu}(x - a\hat{\rho})\, U_{\rho}(x - a\hat{\rho} + a\hat{\mu})\Big),
\end{aligned} \tag{1.29}$$

(*cf.* equation 1.26). Smearing with $\mathcal{F}_{\mu}$ removes the tree level taste-exchange interaction but introduces new $\mathcal{O}(a^2)$ errors. These can be removed by modifying the smearing like so,

$$\mathcal{F}^{\mathrm{ASQTAD}}_{\mu} \equiv \mathcal{F}_{\mu} - \sum_{\rho \neq \mu} \frac{a^2 (\delta_{\rho})^2}{4}. \tag{1.30}$$

$\mathcal{F}^{\mathrm{ASQTAD}}_{\mu}$ smears links in the μ direction while generating unsmeared links in the orthogonal directions (to preserve gauge invariance). Modifying the derivative with the Naik term and smearing the link fields with $F^{\mathrm{ASQTAD}}_{\mu}$ results in the 'ASQTAD' action.

It was observed that repeated smearing of the gauge fields further reduced the pion taste mass splitting and therefore suppressed one-loop taste-changing errors. Smearing the links multiple times ensures links in all directions are smeared and so suppresses highly virtual taste-changing gluons. Such a smearing operator, $\mathcal{F}^{\mathrm{HISQ}}_{\mu}$, is defined as

$$\mathcal{F}^{\mathrm{HISQ}}_{\mu} \equiv \mathcal{F}^{\mathrm{ASQTAD}}_{\mu} \mathcal{U} \mathcal{F}_{\mu}, \tag{1.31}$$

where $\mathcal{U}$ unitarises whatever it acts on and then projects onto SU(3). These SU(3) fields are stored as 3x3 complex matrices and can be paramaterised by eight real numbers. A smeared link that has been unitarised is bounded by unity. This combination of reunitarisation and projection stops the growth of two gluon vertices induced by the large number of products of links in the smearing.

Tree-level discretisation errors in the ASQTAD action are negligible for light quarks but not for charm and bottom, being $\mathcal{O}((am)^4)$. Retuning the coefficient of the Naik term, ϵ, by matching to the tree-level quark dispersion relation removes these errors,

$$D_\mu \to \Delta_\mu - \frac{a^2}{6}\,(1\,+\,\epsilon)\Delta_\mu^3. \tag{1.32}$$

The retuning of the Naik coefficient and the double smearing of the gauge fields transforms the ASQTAD action into the HISQ action. The HISQ action,

$$\sum_{n,\mu}\ \overline{\chi}_n\ \left(\theta_\mu D_\mu^{\rm HISQ} + m\right)\ \chi_n, \tag{1.33}$$

has no tree level $\mathcal{O}(a^2, (am)^4)$ errors. The covariant derivative is

$$\begin{aligned} D_\mu^{\rm HISQ} &\equiv \Delta_\mu(W) - \tfrac{a^2}{6}(1+\epsilon)\Delta_\mu^3(X) \\ W_\mu(x) &\equiv \mathcal{F}_\mu^{\rm HISQ}\, U_\mu(x), X_\mu \equiv \mathcal{U}\mathcal{F}_\mu U_\mu(x). \end{aligned} \tag{1.34}$$

The HISQ action suppresses unphysical taste-changing interactions by 3-4 times over the ASQTAD action and, as remarked earlier, is very accurate when simulating heavy quark physics, a feature we utilise in

our study of hybrid charmonium mesons, and light quark physics, this property being inherited from its parent ASQTAD action.

1.2.3 The fourth root approximation

We still have the problem of the four degenerate tastes per quark flavour in the continuum. To see how this unwanted degree of freedom has been dealt with recall the general form of the expectation value of an observable,

$$\langle \mathcal{O} \rangle = \frac{1}{Z} \int [dU] \mathcal{O}(M_{ij}^{-1}) \det M e^{-S_G}. \tag{1.35}$$

This equation is the same as equation 1.5 with the dependence of the observable $\mathcal{O}$ on the propagators made explicit. Staggered fermions appear in two places, sea quarks in $\det M$, and valence quarks in $\mathcal{O}(M_{ij}^{-1})$. To collapse the multiplicity of the sea quarks the fourth root of the fermionic determinant is taken. This rooting procedure was (and to a small extent is) controversial [18, 40], and there is no rigorous theoretical proof that the continuum limit is smooth. However the weight of practical evidence in its favour over the last 15 years, and the broad agreement between independent calculations using staggered fermions and other fermion formulations, gives us confidence that the rooting procedure is not fatal to the reliability of our results. The theoretical arguments for and against the rooting procedure are discussed in [41, 42, 43, 44].

1.3 Renormalisation

It was realised early on in the development of the subject that QFTs are riddled with divergences that need to be cured. In Perturbation Theory (PT) these divergences can be dealt with by imposing a cutoff, Λ, on the momenta being summed over in the path integrals associated with an observable. The integrals can then be split into a finite cutoff-independent part, and a finite cutoff-dependent part from which the divergence arises. The divergence may then be absorbed into a parameter of the theory by renormalising that parameter with reference to some physical quantity, usually the masses and couplings of the theory. The parameters appearing in the Lagrangian are called bare parameters, in contrast to the renormalised parameters they are related to through the renormalisation procedure. Renormalisable theories are ones in which the divergences at all orders can be absorbed by a finite number of parameters. The SM only contains renormalisable QFTs.

The cutoff is called a regulator and its imposition is referred to as 'regulating the theory'. There are other ways to regulate QFTs, such as dimensional regularisation and Pauli-Villars regularisation, and which regulator is most appropriate in a specific situation is a choice for the theorist [45, 46]. The imposition of a regulator introduces a renormalisation scale μ. Scheme-dependent quantities, for instance the quark masses of table 1.1, vary with μ while scheme-independent quantities do not.

Ultimately we want to remove the regulator and re-include the missing high modes of the theory. In the perturbative case this sim-

ply corresponds to sending $\Lambda \to \infty$. After their removal calculated observables should be independent of the choice of regulator.

The finite spacing of the lattice acts as a UV regulator, cutting out modes with momenta greater than $\frac{\pi}{a}$ (in addition the lattice's finite extent acts as an IR regulator, cutting out momenta below $\frac{1}{L}$). Quantities computed on the lattice must then be identified with physical observables through a renormalisation procedure. Different lattice actions will have different renormalisation properties. For example, the remnant chiral symmetry of the staggered fermion formulation means quark masses undergo multiplicative renormalisation, where the bare and renormalised masses are related by $m_0 = Z_m m$, whereas the non-chiral Wilson quarks renormalise additively, $m_0 = (1 + \delta_m)m$.

It is the adopted practice of theorists and experimenters to express the values of scheme-dependent quantities in the modified minimal subtraction scheme, $\overline{\text{MS}}$, at an appropriate scale. Therefore it is desirable to adopt a regularisation scheme that can be implemented in continuum PT and in lattice simulations. One could convert results from the lattice scheme directly to the $\overline{\text{MS}}$ scheme using lattice perturbation theory. However Feynman rules for lattice actions can be very complicated with poor convergence, and this has prompted the creation of the Regularisation-Independent (RI) nonperturbative matching procedure [47].

In the RI scheme renormalisation factors are defined as ratios of expectation values of quark bilinear operators between off-shell single

particle momentum eigenstates in the full and free theories,

$$\langle p|\mathcal{O}_\Gamma|p\rangle_0 = Z_\Gamma^{\mathrm{RI}}(\mu^2)\langle p|\mathcal{O}_\Gamma|p\rangle_{p^2=\mu^2}. \tag{1.36}$$

Since equation 1.36 is gauge variant these expectation values are formed from quark and gluon Green's functions computed in a smooth fixed gauge. If the same RI scheme is implemented both in lattice QCD and in continuum QCD then the continuum limit of the lattice results will be in the continuum RI scheme. These RI results can then be converted to the $\overline{\mathrm{MS}}$ scheme using PT. The matching factors needed,

$$R(\mu, a) = \frac{Z_\Gamma^{\overline{\mathrm{MS}}}(\mu)}{Z_\Gamma^{\mathrm{RI}}(\mu, a)}, \tag{1.37}$$

have been calculated to 3 loops in PT for several RI schemes [48, 49]. Converting results into the $\overline{\mathrm{MS}}$ scheme occurs in two steps, lattice $\longrightarrow$ RI $\longrightarrow$ $\overline{\mathrm{MS}}$.

We now briefly describe a specific RI scheme, the RI-SMOM scheme, developed by HPQCD [50], which has been used to calculate renormalisation factors for the local vector current that is used later on in this work. This scheme is one of a class of so-called 'momentum-subtraction' schemes.

1.3.1 Nonperturbative renormalisation of the vector current in the RI-SMOM scheme

The RI-SMOM scheme defines a vector renormalisation factor, Z_V^{SMOM}, from the ratio of matrix elements calculated between external quark

states of large virtuality in a fixed gauge,

$$Z_V^{\mathrm{SMOM}} \langle p_1 | J_i | p_2 \rangle = \langle p_1 | J_i | p_2 \rangle_{\mathrm{tree}}. \tag{1.38}$$

In the RI-SMOM scheme the momenta are chosen in a symmetric configuration where $p_1^2 = p_2^2 = q^2 \equiv \mu^2$ and $q = p_1 - p_2 \neq 0$. There is only a single (renormalisation) scale μ.

The RI-SMOM scheme was defined with the vector Ward-Takahashi identity (WTI) in mind [51]. In the continuum the vector current satisfies the WTI and on the lattice it can be shown that the conserved vector current satisfies the lattice WTI,

$$\frac{-2i}{a} \sin\Big(\frac{aq_\mu}{2}\Big) \Lambda_V^{\mu,+}(p_1, p_2) = -S^{-1}(p_1) + S^{-1}(p_2), \tag{1.39}$$

where S is the quark propagator and $\Lambda_V^{\mu,+}$ is the amputated vertex function for the conserved vector current, formed by dividing the vertex function on either side by quark propagators, $\Lambda_V = S^{-1}(p_2) G_V S^{-1}(p_1)$,

$$G_V = \langle \psi(p_1) \left(\sum_x \overline{\psi}(x) \gamma_\mu \psi(x) e^{i(p_1 - p_2)x} \right) \overline{\psi}(p_2) \rangle. \tag{1.40}$$

The conserved vector current on the lattice is action dependent however and involves 1-link and 3-link pieces in the HISQ formalism. Oftentimes, as in this work, the local or 1-link point-split vector currents are used instead. These vector currents don't satisfy the lattice WTI. Renormalisation factors for these nonconserved vector currents are defined so that the renormalised currents satisfy the same WTI as the conserved current, only differing by discretisation effects. Further-

more, since the WTI is also satisfied by the conserved vector current in the continuum $\overline{\text{MS}}$ scheme, matrix elements in this scheme will agree with matrix elements of the conserved vector current on the lattice in the continuum limit. In the continuum the wave-function renormalisation is defined as

$$Z_q = -\frac{i}{12p^2}\text{Tr}(\not{p}S^{-1}(p)), \tag{1.41}$$

and the vector current renormalisation is defined as

$$\frac{Z_V}{Z_q}\frac{1}{12q^2}\text{Tr}(q_\mu \Lambda_V^\mu(p_1,p_2)\not{q}) = 1, \tag{1.42}$$

where the trace over colour and spin acts on $\not{q}q_\mu\Lambda_V^\mu$ which becomes $\sum_{\mu,\nu}\hat{q}_\nu(\gamma_\nu\otimes\gamma_\mu)\hat{q}_\mu\Lambda_{V,\text{loc}}^\mu$ in the HISQ formalism. The normalisations in these definitions are set so that $Z_q = Z_V = 1$ at tree level (see equation 1.38). By computing propagators and vertex functions at different values of μ, and averaging over gluon fields fixed to Landau gauge, equations 1.41 and 1.42 are used to compute $Z_V^{\text{SMOM}}(\mu)$.

The authors of [50] found they only needed around 20 configurations for small statistical uncertainties. The RI-SMOM scheme is defined at zero valence quark mass, so for each μ the calculation is done at multiple light quark masses before being extrapolated to zero.

1.4 QED on the lattice

QED is a quantum field theory that describes the electromagnetic interactions of light and matter. QED's origins lie in Dirac's work on

a quantum theory of the electron [52]. It was then developed over a series of years into a fully fledged calculational tool by Feynman, Schwinger, Tomonaga, and Dyson [53, 54, 55, 56, 57]. When considering hadronic observables QED effects can often be ignored because the electromagnetic coupling $\alpha \sim \frac{1}{137}$, whilst the strong coupling $\alpha_s \sim 1$, so that QED effects contribute around 1% to hadronic observables. Until recently the total uncertainty on many lattice observables was greater than 1% so QED could be ignored or a rough estimate of its effect could be included as a systematic uncertainty. But with measurements on the lattice continually improving in precision, through improved statistics and systematics, many groups are now finding they need to include QED in their simulations if they wish to continue reducing their uncertainties and improving their accuracy.

Putting QED on the lattice is non-trivial. The zero modes of the photon propagator produce infrared divergences and cause difficulty when trying to study charged particles. To see this consider Gauss' law, which predicts a net flux through a surface enclosing a charged particle. This is clearly incompatible with the periodic boundary conditions we impose on the lattice. In spite of this there are many ways to usefully define QED in a finite volume.

The QED_{TL} approach removes the global zero modes by hand [58]. The massive photon approach simulates with a massive photon before removing its unphysical effects with an effective field theory [59]. A local solution involves the imposition of so-called C^* boundary conditions, where the gauge fields are periodic up to charge conjugation, $A_\mu \xrightarrow{+L} -A_\mu$ [60, 61]. These anti-periodic boundary conditions auto-

matically remove the zero modes, while breaking flavour and charge conservation at the boundaries.

In the work presented in this thesis, QED effects have been included using the $\mathrm{QED_L}$ formalism. $\mathrm{QED_L}$ is popular in the literature and its theoretical properties, such as finite volume effects, are well studied. Finite volume effects are generally larger in QED, obeying power laws $\mathcal{O}(1/L^n)$, than QCD, $\mathcal{O}(e^{-m_\pi L})$.

1.4.1 $\mathrm{QED_L}$

In the $\mathrm{QED_L}$ approach the problematic zero modes are removed by hand, $A_\mu(\hat{k}_0, |\hat{k}| = 0) = 0$, where A_μ is the vector potential [62]. The photon propagator in Coulomb gauge in $\mathrm{QED_L}$ is then

$$\begin{aligned} \mathcal{D}_{ij}(k) = \langle A_i(k) A_j(-k) \rangle &= \begin{cases} \frac{1}{k^2}\left(\delta_{ij} - \frac{k_i k_j}{\mathbf{k}^2}\right), & \mathbf{k} \neq 0 \\ 0, & \mathbf{k} = 0 \end{cases} \\ \mathcal{D}_{00}(k) = \langle A_0(k) A_0(-k) \rangle &= \begin{cases} \frac{1}{k^2}, & \mathbf{k} \neq 0 \\ 0, & \mathbf{k} = 0 \end{cases} \end{aligned} \tag{1.43}$$

This quenching of the spatial zero modes of the gauge field at any time is non-local but unlike $\mathrm{QED_{TL}}$ the transfer matrix is well-defined. The HPQCD collaboration have performed several QCD+q$\mathrm{QED_L}$ calculations on HISQ ensembles [50, 63, 64, 65, 66].

Chapter 2

Measuring Observables on the Lattice

In this chapter we outline the typical progression of a lattice calculation and discuss some practical considerations the lattice theorist must make. We begin by discussing the generation of gauge fields, including the quenched U(1) fields used in our analysis in chapter 4. Then we describe the conjugate gradient algorithm as it is used for computing quark propagators. Statistical methods for the analysis of correlator data are discussed, including the Bayesian extension of least-squares fitting. We end with a short discussion on how to connect results on the lattice to the real world.

Lots of lattice codes are available, written in different languages and optimised for particular computer architectures. The lattice code primarily used in this work is the open source MILC code, written in C and available at https://github.com/milc-qcd/milc_qcd.

2.1 Generating gauge fields

In the previous chapter we noted that the path integral formulation of a QFT, equation 1.5, lets us write expectation values as an integral over the gauge fields of products of quark and gluon fields weighted by a Boltzmann factor, e^{-S}. On a typical lattice there are, conservatively, $\sim 10^4$ lattice points with each SU(3) link field described by 8 continuous parameters. There are therefore $\sim 10^5$ integration variables in a typical path integral. Such a high-dimensional integral is not tractable by high-dimensional analogues of the trapezium rule. Instead the gauge fields, U_i, are sampled from a distribution,

$$dP = \frac{e^{-S[U]}\mathcal{D}[U]}{\int \mathcal{D}[U] e^{-S[U]}}. \tag{2.1}$$

This is called importance sampling as dP is peaked around field configurations that minimise the action and contribute more to the path integral. Expectation values then become sums over importance sampled configurations,

$$\langle \mathcal{O} \rangle = \lim_{N \to \infty} \frac{1}{N} \sum_{i=1}^{N} \mathcal{O}[U_i]. \tag{2.2}$$

Finding U_i that vary according to dP is non-trivial and is not the focus of this work. One algorithm, the Metropolis algorithm, generates a Markov chain of configurations by starting from a random configuration and then updating the link fields [67, 68, 69]. Successive U_i in the chain are rejected and thrown out if S increases or does not decrease sufficiently.

2.1.1 Autocorrelations

The ensemble of field configurations on which an observable is measured should comprise a statistically independent sample. To this end when these fields are generated, as part of a Markov chain, every nth field configuration is sampled with the other fields being discarded. However even after this process it is normally found that consecutive configurations retain a residual correlation. These correlations in simulation time are referred to as autocorrelations. They are important to consider as they can lead to the underestimation of uncertainties of lattice observables.

The autocorrelation coefficient $C(\tau)$ of an observable A at simulation time lag $\tau = \Delta\tau(i-j)$ is defined as

$$C(\tau) = \langle x_i x_j \rangle, \quad x_i = \frac{A_i - \langle A \rangle}{\sigma_0} \tag{2.3}$$

where the fluctuations x_i are scaled by σ_0, the naive sample variance.

By considering the variance of the mean fluctuation, $\sum_i x_i/N$, and the definition 2.3 above, one can show that the true and naive variances of A are related by,

$$\sigma^2 = \sigma^2_{\text{naive}} \left(1 + 2C(\Delta\tau) + 2C(2\Delta\tau) + \dots\right), \tag{2.4}$$

where it can be shown that $\sigma^2 \geq \sigma^2_{\text{naive}}$. If the A_i are uncorrelated then $C(\tau) = 0$ for $\tau \neq 0$ and the variance does not change. If autocorrelations are present then $C(\tau)$ is a sum of decaying exponentials. The time constant of the slowest exponential can then be defined as

the autocorrelation time of the system.

The usual way to deal with autocorrelations, and the method favoured in this work, is through binning. Binning involves partitioning the data into blocks of N_b measurements of adjacent configurations and averaging the data within a block. This leaves a reduced dataset of N/N_b correlators with reduced autocorrelations. The stability of fitted parameters against a varying bin size is an important measure of the robustness of a fit.

Although we mainly used binning to deal with autocorrelations we also investigated using the `unew` python package to measure the extent of any autocorrelations in our data [70, 71]. Where carried out these investigations affirmed the conclusions reached via binning studies on the extent of autocorrelations in our data. See figure 4.13 for an example of a binning study we carried out in the course of our research.

2.1.2 U(1) field generation

To measure QED effects on hadronic observables we need to generate U(1) fields [72]. Gauge field generation is done with respect to the compact U(1) action,

$$S = \frac{1}{4} \sum_{x,\mu,\nu} F_{\mu\nu}^2, \tag{2.5}$$

with the U(1) lattice field strength tensor defined as

$$F_{\mu\nu} = A_\mu(x) + A_\nu(x+\hat{\mu}) - A_\mu(x+\hat{\nu}) - A_\nu(x). \tag{2.6}$$

Taking the Fourier transform of the vector potential and field strength, and defining

$$\begin{aligned} \tilde{A}_\mu(k) &= e^{-ik_\mu/2} A_\mu(k) \\ \tilde{F}_{\mu\nu}(k) &= e^{-ik_\mu/2 - ik_\nu/2} F_{\mu\nu}(k) \\ \hat{k}_\mu &= 2 \sin k_\mu/2, \end{aligned} \tag{2.7}$$

we arrive at the action in momentum space,

$$S = \frac{1}{4} \sum_{\mu\nu} |\tilde{F}_{\mu\nu}(k)|^2 = \frac{1}{2} \sum_{\mu\nu} \tilde{A}_\mu(k) [\hat{k}^2 \delta_{\mu\nu} - \hat{k}_\mu \hat{k}_\nu] \tilde{A}^*_\nu(k). \tag{2.8}$$

To generate an ensemble of fields with probability $dP = \exp^{-S(A)}[dA]$ we generate gaussian random complex vector fields, $\eta_\mu(k)$, with stochastic average,

$$\langle \eta_\mu(k)\, \eta^*_\nu(k') \rangle = \delta_{\mu\nu}\, \delta_{kk'}. \tag{2.9}$$

Then we define the Feynman gauge field as,

$$\tilde{A}^{(F)}_\mu(k) = \sqrt{\frac{2}{h_p \hat{k}^2}}\, \eta_\mu(k) \tag{2.10}$$

with $h_p = 1$ if $\tilde{A}^{(F)}_\mu$ is real and $h_p = 2$ otherwise. Transforming to Landau gauge can be done by projecting out the photon field along $\hat{k}$, and the transformation to Coulomb gauge is also straightforward [72]. Exponentiation then yields the desired U(1) fields as $\exp ieQA_\mu$, where Q is the electric charge. $\mathrm{QED_L}$ field generation routines for all these have been implemented in the MILC code. Including QED effects in our analysis is then as simple as multiplying the U(1) fields

into the SU(3) links before computing the quark propagators. The calculation then proceeds in the same way as a pure QCD calculation.

Since these U(1) fields have been generated independently of the SU(3) fields they cannot have influenced the sea quark interactions. For this reason these U(1) fields are referred to as electro-quenched. A big advantage of this approach is that these fields can be used with already existing pure QCD ensembles, whereas including QED dynamics in the sea requires the costly generation of new ensembles.

2.2 Scale Setting

On the lattice one determines dimensionless quantities, like amplitudes and masses, as a function of the bare coupling. The theory predicts dimensionless ratios of dimensionful scales, like $\mathcal{R}_i = m_i/m_{\text{ref}}$, but not the scale itself. One could stop here and list one's results as dimensionless ratios against some reference scale, but this would be of limited use. The absolute scale must be determined by associating a quantity on the lattice with a physical quantity derived from experimental observations. A natural scale we could use for QCD is the proton mass, m_p, or the pion decay constant, f_π. Once the scale has been set every other output of the calculation may be converted into physical units.

In lattice calculations scale setting is equivalent to fixing the lattice spacing a at a particular bare coupling g_0. For example, given dimensionless masses M measured on the lattice, if we wished to set the scale with m_p we would carry out the following steps to find the

mass, m, of a hadron of interest in physical units,

$$\begin{aligned} M_p = a m_p \implies a(g_0) &= \frac{M_p(g_0)}{m_p} \\ \therefore \quad m(g_0) &= \frac{M(g_0)}{a(g_0)}. \end{aligned} \tag{2.11}$$

When planning simulations we also need the scale since the quark masses are usually tuned by adjusting pseudoscalar meson masses measured on the lattice to their physical values. Any dimensionful quantity can be used to set the relative scale between ensembles of differing lattice spacing, and care should be taken in its choice. The chosen scale should be derived from a quantity that is precisely computable with low numerical effort, has small controlled systematic uncertainties, and has a weak quark mass dependence. Sommer classifies scales as either 'phenomenological' or 'theory' scales [73]. Phenomenological scales are those which require a minimal amount of theory to connect the lattice to experiment. The pseudoscalar decay constants are an example of such a scale and are used by many groups as pseudoscalar correlators have the best possible signal-to-noise ratio. Theory scales are quantities that are designed to be easy to calculate on the lattice but require more theory to connect to the lattice. Commonly used theory scales are r_0 and r_1, defined from the heavy quark potential, and t_0 and w_0, defined from the gradient flow. Theory scales can more precisely set the relative scale, but a phenomenological scale is still ultimately needed to set the absolute scale, by extrapolating $w_0 M_\Omega$ for instance.

2.2.1 The gradient flow

The gradient flow equations are a set of diffusion equations that describe how a gauge field, B_μ, evolves in a fictitious flow time t [74, 75],

$$\begin{aligned} &\frac{dB_\mu}{dt} = -g_0^2 \frac{\partial S}{\partial B_\mu} = D_\nu G_{\nu\mu}\,, \quad B_\mu(0) = A_\mu\,, \\ &D_\nu X = \partial_\nu X + [B_\nu,\ X]\,, \quad G_{\nu\mu} = \partial_\nu B_\mu - \partial_\mu B_\nu + [B_\nu,\ B_\mu]\,. \end{aligned} \tag{2.12}$$

With increasing t the flow equations 2.12 push the gauge field towards stationary points of the action along the path of steepest descent. In lattice QCD the gauge fields are the SU(3) gluon fields and there is an extra factor of the link fields to preserve gauge invariance,

$$\frac{dV(t)_{i,\mu}}{dt} = -g_0^2 \frac{\partial S(V)}{\partial V_{i,\mu}} V_{i,\mu}\,, \quad V_{i,\mu}(0) = U_{i,\mu}. \tag{2.13}$$

The effect of the evolution in t is a smoothing of the gauge field, pushing the gluon field towards a smooth renormalised field. This flow introduces an independent dimensionful variable, the flow time. Quantities calculated on the lattice from the smoothed gauge links become functions of the flow time, and one can define a scale from this functional dependence. A good quantity on the lattice is the average total energy within a smoothed volume, which is $\propto t^2\langle E(t)\rangle$ where $E(t) = \frac{1}{4}G_{\mu\nu}G^{\mu\nu}$ is the gluon action density. A fiducial point c is chosen which defines the reference time t_0. Empirical evidence suggests the slope of the energy with time has smaller discretisation effects. This lead the BMW collaboration to introduce the parameter

w_0 [76], defined like so,

$$\left[t\frac{d}{dt}t^2\langle E(t)\rangle\right]_{t=w_0^2} = c \ , \tag{2.14}$$

where $c = 0.3$ or $2/3$ depending on whether one wants to minimise discretisation effects, finite volume effects, or the amount of resources one is willing to spend on the calculation.

In their paper introducing w_0 BMW used m_Ω to set the overall scale and found $w_0 = 0.1755(18)$ fm [76]. They also found good agreement for w_0 calculated with the staggered and Wilson actions. As part of their recent HVP calculation they redid the scale setting, now including isospin breaking effects on m_Ω, and produced a more precise determination of $w_0 = 0.17236(70)$ fm [77].

The MILC and HPQCD collaborations have used w_0 to fix the relative lattice spacing on MILC's $N_f = 2+1+1$ HISQ ensembles [78, 79, 80]. Both used the pion decay constant, f_π, to set the overall scale. Both determinations are consistent with each other, with HPQCD finding $w_0 = 0.1715(9)$ fm and MILC finding $w_0 = 0.1714(15)$ fm. As we are using a subset of the HISQ ensembles we use the HPQCD determination of w_0 to fix the overall scale in our analyses in chapters 3 & 4. We expect the effect from QED on the lattice spacing to be negligible and ignore it.

2.3 Measurements on the lattice

In the path integral approach expectation values are given by time-ordered correlation functions. Two-point correlators on the lattice consist of a source operator which creates states that propagate on the lattice before being terminated by a sink operator.

Measuring correlators on the lattice involves inverting the Dirac equation,

$$(\not{D} - m)\psi \equiv M\psi = \psi_0, \tag{2.15}$$

where the ψ are to be solved for after a source, ψ_0, with the appropriate quantum numbers is specified. Solving for ψ on a given background configuration is done by inverting M. On the lattice $(M^{-1})^{y,j,b}_{x,i,a}$ is a finite sparse matrix labelled by site, spin, and colour indices with each of its elements giving the amplitude for the propagation of a quark with site-spin-colour $\{x, i, a\} \longrightarrow \{y, j, b\}$. Inverting M directly is challenging as it has a very large dimension of a few times the lattice volume, and must be done numerically on a computer. Algorithms, such as the conjugate gradient algorithm discussed below, are needed to perform the calculation. Instead, given a point source ψ_0, we try to find $\psi = M^{-1}\psi_0$. This is the quark propagator from the source to all the other sites of the lattice and corresponds to 12 columns (or rows) of M^{-1}, one for each colour and spin degree of freedom. The propagation of the state is then terminated by a sink operator, usually with the same quantum numbers as the source.

A meson is made up of a quark and an antiquark with specific quantum numbers. Therefore on the lattice quark bilinears with the

appropriate γ matrices are used as interpolating operators for mesons. The interpolating operators, ψ and $\overline{\psi}$, create or annihilate the quark fields. In the Wilson formulation the pseudoscalar meson operator is $\overline{\psi}\gamma_5\psi$. The pseudoscalar 2-point correlation function,

$$G(t) = \langle 0| \sum_x \overline{\psi}_i^a(x,t)\gamma_5\psi_i^a(x,t)\overline{\psi}_j^b(0,0)\gamma_5\psi_j^b(0,0)|0\rangle, \qquad (2.16)$$

where the spin, (i,j), and colour, (a,b), indices are summed over, creates the desired meson at (0,0) and annihilates it at (x,t). This is the object we need to measure on the lattice to determine the pseudoscalar meson mass and decay constant. The sum over space, $\sum_x$, projects out the zero momentum states. Stochastic wall sources, where random colour vector fields are generated on all the lattice points on a specified timeslice, can be used instead of a point source. Then an additional stochastic volume average over the wall points has to be performed.

The state generated by the $\mathcal{O}_i = \overline{\psi}\gamma_5\psi$ operator acting on the vacuum is a linear combination of all the possible eigenstates of the Hamiltonian that have the same quantum numbers as the pion. From quantum mechanics we also know that an eigenstate of energy E picks up a factor of e^{-Et} after propagating for Euclidean time t. By inserting the identity, $1 = \sum_n |n\rangle\langle n|$ where n labels the (infinite) eigenstates, into equation 2.16, one can show that the 2-point correlation function

is a sum of exponentials,

$$\begin{aligned} G(t) &= \langle 0| \sum_x \mathcal{O}_f(x,t)\mathcal{O}_i(0)|0\rangle \\ &= \langle 0| \sum_x \mathcal{O}_f(x,t)\Big\{ \sum_n |n\rangle\langle n| \Big\}\mathcal{O}_i(0)|0\rangle \\ &\vdots \\ &= \sum_n \frac{\langle 0|\mathcal{O}_f|n\rangle\langle n|\mathcal{O}_i|0\rangle}{2E_n} e^{-E_n t}, \end{aligned} \tag{2.17}$$

where the exponents are the energies of the eigenstates E_n, and the size of the coefficients are related to the energies and overlap factors, $\langle 0|\mathcal{O}_{i,f}|n\rangle$. See [81] for more details.

In the staggered formalism we have the extra taste quantum number. The local pseudoscalar operator in the staggered spin-taste basis is $\overline{\psi}(\gamma_5 \otimes \gamma_5)\psi$. In the staggered single-component basis this becomes $\sum_\eta (-1)^\eta \overline{\chi}_{2y+\eta}\chi_{2y+\eta}$, where y labels the 2^4 staggered hypercube, and η is the lattice coordinate. The phase factor, here $(-1)^\eta = (-1)^{\eta_0+\eta_1+\eta_2+\eta_3}$, patterns the staggered fields over the lattice to produce the desired quantum numbers.

In practice it is easier to work with the quark propagators obtained by contracting the quark fields using Wick's theorem. The Feynman propagator, S_F, on a single background field is given by

$$S_F(y,j,b;x,i,a) = \langle 0|\psi_j^b(y)\overline{\psi}_i^a(x)|0\rangle = (M^{-1})_{x,i,a}^{y,j,b}. \tag{2.18}$$

Once the required propagators are computed they are tied together

by tracing over their spin and colour indices,

$$G(t) = \langle 0| \sum_x \mathrm{Tr}[S_F(0;x,t)\gamma_5 S_F(x,t;0)\gamma_5]|0\rangle. \tag{2.19}$$

Staggered correlation functions swap out γ matrices for phase factors, $(-1)^{f(\eta_i)}$, and can straddle two timeslices, an issue which we address later on in this chapter. In this way a correlator is calculated on each of the field configurations in an ensemble. In the final step the expectation value is obtained by averaging the correlators over the configurations.

2.3.1 The conjugate gradient algorithm

Equation 2.15 is a matrix equation of the form $Ax = b$, where A is a large sparse matrix, b is a source vector, and we seek the solution x. The conjugate gradient algorithm and its variants are sparse solution methods for this type of equation and have been used very successfully in lattice QCD since the field's inception [82].

Let (x, y) be the scalar product of the vectors x, y. Then the conjugate gradient algorithm generates a series of successively more accurate approximate solutions x_i, with residual vectors, $r_i = b - Ax_i$, shrinking in size as the algorithm advances towards the solution.

Starting from an initial guess x_0, with residual $r_0 = b - Ax_0$, the problem reduces to solving $A(x - x_0) = r_0$. Successive solutions are constructed by adding $\alpha_i p_i$, where the p_i are search vectors and the α_i are coefficients. The search vectors are drawn from an n-dimensional Krylov space, $\mathcal{K}_n$, spanned by the vectors $\{r_0, Ar_0, A^2 r_0, \cdots, A^{n-1} r_0\}$,

that grows in size as the algorithm advances and n increases [83]. The α_i are chosen so that the solutions minimise the norms of the residuals. The CG algorithm specifies that the search vectors must be mutually orthogonal with respect to A, $(p_i, Ap_j) = 0$ for $i \neq j$. This condition can be satisfied by requiring the search vector to be a linear combination of the residual and previous search vector, with coefficients β_i defined below in equation 2.20.

The CG algorithm works as follows: Choose $x_0 \implies r_0 = b - Ax_0$, and choose $p_0 = r_0 \in \mathcal{K}_0$. Then for $n \geq 0$

$$\begin{aligned} \alpha_n &= \frac{(r_n, r_n)}{(p_n, Ap_n)} \\ x_{n+1} &= x_n + \alpha_n p_n \\ r_{n+1} &= r_n - \alpha_n A p_n \in \mathcal{K}_{n+1} \\ \beta_n &= \frac{(r_{n+1}, r_{n+1})}{(r_n, r_n)} \\ p_{n+1} &= r_{n+1} + \beta_n p_n \in \mathcal{K}_{n+1}. \end{aligned} \tag{2.20}$$

The algorithm ends when the cartesian norm of the residual falls below some threshold, $||r_n|| < \epsilon$. ϵ is a parameter, `rel_error_for_propagator`, that can be set in the MILC template file. With exact arithmetic the CG algorithm will terminate at some step, N, with $r_N = 0$. In practice however the algorithm is carried out with machine precision arithmetic, and the resulting accumulation of rounding errors causes two issues. The residuals, $r_n = r_{n-1} - \alpha_{n-1} A p_{n-1}$, become less reliable estimators of the true residual, $b - Ax_n$, and duplicate search vectors are generated later on. Increasing the machine precision can help and so can restarting the algorithm, using the last best solution, x_n, as the

new initial guess. In the MILC code the parameter `max_cg_restarts` sets the maximum number of restarts the CG algorithm may take.

There are many variants of the CG algorithm with performance varying by fermion formulation. For staggered fermions the standard CG algorithm, equation 2.20, has been found to work well. In recent years GPU technology has been taken advantage of to speed up the runtime of the CG algorithm. The correlators analysed in chapter 4 were measured with GPUs.

2.3.2 Truncated Solver Method

To improve the statistics on an ensemble it is often the case that multiple measurements with time shifted sources are taken on each field configuration. So long as the different time sources are not highly correlated this process can increase by an order of magnitude the amount of data from an ensemble. It has been observed that, with stochastic sources, solvers converge in a small number of iterations. This motivated lattice theorists to reduce the residual aimed for by the solver and so speed up their measurements. Since the solver would then stop after fewer iterations this technique is called the truncated solver method (TSM) [84]. To guard against any new systematic bias we measure the correlator on one time source at two levels of precision and compare them. The solution with the smaller residual is called the precise solve and the one with the larger residual is called the sloppy solve. As an example suppose we measure 16 sloppy solves and

1 precise solve. The average over the sources is then

$$G(t) = \frac{1}{15} \sum_{i \neq j} G^i_{\text{sloppy}}(t) + (G^j_{\text{prec}}(t) - G^j_{\text{sloppy}}(t)) \ , \tag{2.21}$$

where the sum is taken over the 15 sloppy-only time sources and j labels the time source on which both sloppy and precise solves were calculated. The TSM works by reducing the precision of the solves of the conjugate gradient algorithm, leading to a reduction in the time elapsed. In order to check this procedure does not introduces biases into our results we can compare the fractional error of different combinations of sloppy and precise solves. Figure 4.11 illustrates how the TSM works in practice by plotting the fractional error of the vector correlator, computed on one of the ensembles used in the HVP analysis, for different combinations of sloppy and precise solves.

2.4 Fitting Correlators

Having measured correlators over a set of importance-sampled gauge configurations we now turn to the question of how to extract information from this statistical dataset. A meson correlator takes the exact form

$$G(t; A_n, E_n) = \sum_{n=1}^{\infty} A_n \, \mathrm{e}^{-E_n t}, \tag{2.22}$$

where the A_n and E_n are the amplitudes and energies of the states coupled to by the operator forming the correlator. By convention the states are arranged in order of ascending energy, $E_{n+1} > E_n$, E_1 being the energy of the ground state. The most common goal of a lattice

analysis is to find the amplitudes and energies by fitting correlator data to a model of this kind.

A slight complication arises when considering correlators formed from staggered fermions. In general the staggered operator with quantum numbers $\Gamma_S \otimes \Gamma_T^*$ is not confined to a single time slice, and so the linear combination

$$\Gamma_S \otimes \Gamma_T^* \pm \Gamma_{S\gamma_0\gamma_5} \otimes \Gamma_{T\gamma_0\gamma_5}^*, \tag{2.23}$$

which is a single-time-slice operator is used [4]. The second term generates states with opposite parity and adds an oscillating term to the correlation function,

$$G(t; A_n, E_n, A_{on}, E_{on}) = \sum_{n=1}^{\infty} A_n \, \mathrm{e}^{-E_n t} + \sum_{n=1}^{\infty} (-1)^t A_{on} \, \mathrm{e}^{-E_{on} t}, \tag{2.24}$$

where the A_{on}, E_{on} are the amplitudes and energies of the oscillating states. The addition of the oscillating terms has benefits and drawbacks. An obvious drawback is that the fits are harder as there are more parameters, and the data is less smooth from timeslice to timeslice. A benefit arises from the fact that since the oscillating states have opposite parity one can gain extra information by fitting the A_{on}, E_{on}. As we will see in the next chapter this is useful if the parity partner is expected to be a conventional meson and the non-oscillating state is exotic.

Since we cannot constrain an infinite number of parameters with a finite number of data points, $G(t), t = 0 \ldots N{-}1$, we truncate equation 2.22 to a finite number of exponentials and use this as our fit model.

At sufficiently large t all the exponentials will have died off except for the lowest energy one. Then the correlator $\sim e^{-E_1 t}$ and can be fit by a simple one exponential model, provided the increase in noise brought about by the larger t does not drown the signal. In most cases we will use a fit model with more than one exponential so that we can glean information about the excited states.

With the exception of the pion we expect the correlator's statistical error to grow with time. The reason for this is illustrated by the following argument due to Lepage [85]: The error of a mesonic correlator grows as the correlator squared, which has 4 valence quark lines. The lowest energy state made from 4 quark lines contains two pions and is the dominant contribution to the noise. The noise falls as $\exp(-M_\pi t)$ while the signal, the lowest energy state of the correlator, in general falls much faster as $\exp(-Mt)$. When $M = M_\pi$, the smallest value M can take, the signal and noise fall at the same rate so that the signal to noise ratio is constant. This is why pseudoscalar correlators have the best signal to noise with long plateaus and more precise results.

Traditional fits vary the fit parameters in order to minimise the goodness-of-fit parameter χ^2 defined like so,

$$\chi^2(A_n, E_n) \equiv \sum_{t,t'} (\langle G(t)\rangle - G_{\text{th}}(t,\, A_n,\, E_n))\ \sigma^{-2}_{t,t'} (\langle G(t')\rangle - G_{\text{th}}(t',\, A_n,\, E_n)), \tag{2.25}$$

where $\langle G(t)\rangle$ is the monte-carlo averaged correlator data, and the correlation matrix, σ^2, is defined as

$$\sigma^2_{t,t'} = \langle G(t)G(t')\rangle - \langle G(t)\rangle\langle G(t')\rangle. \tag{2.26}$$

As remarked earlier fitting an infinite number of parameters to a finite dataset leads to parameters with infinite uncertainties. Constraints on the typical values parameters can take are needed for a stable fit. Normally the amplitudes are assumed to be well-behaved, $|A_{n+1}| \lesssim |A_n|$, so that higher energy states are suppressed at large $t > t_{\text{min}}$. Choosing t_{min} involves a trade off between statistical and systematic errors. A larger t_{min} leads to greater statistical errors as the correlator noise grows while a smaller t_{min} has greater systematic errors due to the increased contribution from higher energy states [4]. Adding exponentials to the fit model leads to larger uncertainties as the higher energy states are poorly constrained. In general one would like the statistical error to mask the systematic error but in practice the procedure to choose t_{min} is *ad hoc*.

2.4.1 Constrained Curve Fitting

By restricting the range of values the model parameters can take (consistent with our physical understanding of the system) we can stably fit more of the data with more exponentials. We would like to fit the entire correlator from $t = 0$ to a model with infinitely many exponentials but in practice will have to settle for small t and a large, ~ 10, number of exponentials. By throwing away as little data as possible we retain more information, which will be especially useful when studying excited states.

The authors of [86] augmented the fitting procedure to take ac-

count of the constraints by adding a term to χ^2,

$$\begin{aligned} \chi^2 \quad &\rightarrow \quad \chi^2_{\text{aug}} \equiv \chi^2 + \chi^2_{\text{prior}}, \\ \chi^2_{\text{prior}} &\equiv \sum_n \frac{(A_n - \tilde{A}_n)^2}{\tilde{\sigma}^2_{A_n}} + \sum_n \frac{\left(E_n - \tilde{E}_n\right)^2}{\tilde{\sigma}^2_{E_n}}. \end{aligned} \tag{2.27}$$

Now χ^2_{aug} is to be minimised. This procedure is called constrained curve fitting as the χ^2_{prior} term punishes fits with amplitudes and energies that deviate from $\tilde{A}_n$ and $\tilde{E}_n$ by large amounts. The $\tilde{A}_n, \tilde{E}_n$ and $\tilde{\sigma}_{A_n}, \tilde{\sigma}_{E_n}$ are inputs to the fit model referred to as prior values and prior widths respectively.

This method of curve fitting can be understood from a Bayesian point of view. In this way of probabilistic thinking any prior information should be used to update our posterior. Under the assumption that the fluctuations in the averaged correlator data is Gaussian (which we believe to be a good approximation from the Central Limit Theorem) the probability of the data given a set of parameters is

$$P(\langle G \rangle | \{\alpha_i\}) = \exp -\frac{1}{2}\chi^2. \tag{2.28}$$

The likelihood function, however, is the probability of the parameters conditional on the data, and this is given by Bayes' theorem

$$P(\{\alpha_i\} | \langle G \rangle) = \frac{P(\langle G \rangle | \{\alpha_i\}) P(\{\alpha_i\})}{P(\langle G \rangle)}. \tag{2.29}$$

By choosing to write the prior probability as a Gaussian we recover equation 2.27 and the principle that χ^2_{aug} be minimised in order to

maximise the likelihood function.

In order to carry out a fit we choose a set of priors, $\{\tilde{E}_n, \tilde{A}_n, \tilde{\sigma}_{E_n}, \tilde{\sigma}_{A_n}\}$, and then find the parameters $\{E_n, A_n\}$ that minimise χ^2_{aug}. Adding an exponential to the fit model requires adding priors in beforehand for that term. The imposition of priors is a way of utilising our physical intuition about a system, directing the fit model away from unphysical parameters. In general fitted parameter values stabilise with the addition of exponentials to the fit model. A robust fit should be insensitive to variations in the priors and tested against prior noise. Given a prior distribution P with mean $\overline{P}$ and width δP, we make the replacement,

$$P = \overline{P} + \delta P \longrightarrow \overline{P} + \text{sample}(\delta P) + \delta P, \tag{2.30}$$

before refitting. Parameters that are sensitive to such variations are not determined by the data.

So far we have only been describing single channel fits. With multiple sources and sinks we can form a matrix of correlators by forming different source/sink combinations. We now discuss matrix fits within the framework of the Generalised Eigenvalue Problem (GEVP) [87].

2.4.2 Generalised EigenValue Problem

Finding the energies of the states in a correlator matrix involves solving a GEVP. Starting from the elements of a matrix of Euclidean space

correlation functions,

$$G_{ij}(t) = \langle \mathcal{O}_i(t)\mathcal{O}_j^*(0)\rangle = \sum_{n=1}^{\infty} e^{-E_n t}\psi_{ni}\psi_{nj}^* \quad i,j = 1\ldots N$$
$$\psi_{ni} \equiv (\psi_n)_i = \langle 0|\hat{\mathcal{O}}_i|n\rangle \qquad\qquad E_n < E_{n+1}, \tag{2.31}$$

the GEVP approach amounts to solving the eigenvalue equation

$$G(t)v_n(t,t_0) = \lambda_n(t,t_0)G(t_0)v_n(t,t_0), \quad n = 1,...,N, \;\; t > t_0. \tag{2.32}$$

for the eigenvalues $\lambda_n(t,t_0)$, and eigenvectors $v_n(t,t_0)$. Lüscher and Wolff showed how to determine the ground and excited state energies from the eigenvalues,

$$E_n = \lim_{t\to\infty} E_n^{\text{eff}}(t,t_0),$$
$$E_n^{\text{eff}}(t,t_0) = -\partial_t \log\lambda_n(t,t_0) \equiv -\frac{1}{a}[\log\lambda_n(t+a,t_0) - \log\lambda_n(t,t_0)]. \tag{2.33}$$

Introducing dual vectors u_n,

$$(u_n,\psi_m) \equiv \sum_{i=1}^{N} u_{ni}^*\psi_{mi}, \tag{2.34}$$

$$(u_n,\psi_m) = \delta_{mn} \qquad m,n \le N \;, \tag{2.35}$$

one can show that the GEVP is solved by,

$$\lambda_n^{(0)}(t,t_0) = e^{-E_n(t-t_0)}, \quad v_n(t,t_0) \propto u_n. \tag{2.36}$$

The orthogonality relations,

$$(u_m, G^{(0)}(t)u_n) = \delta_{mn}\rho_n(t), \quad \rho_n(t) = e^{-E_n t}, \tag{2.37}$$

hold for all t. With staggered quarks there are also oscillating eigenvalues,

$$\lambda_n^{(0)}(t, t_0) = s_n(t - t_0)e^{-E_n(t-t_0)}, \tag{2.38}$$

where $s_n(t) = 1$ for non-oscillating states, and $s_n(t) = (-1)^t$ for oscillating states.

2.4.3 SVD cuts

When the number of correlators, N_G, is insufficiently large relative to the number of data points, N_T, the quality of the fit will suffer due to the observed underestimation of the smaller eigenvalues of the correlation matrix. We can see this by rewriting the formula for χ^2 in terms of the eigenvalues and eigenvectors of the correlation matrix, $M_{\text{corr}}v_n = \lambda_n v_n$,

$$\chi^2(\mathbf{p}) = \sum_{n=1}^{N_G} \frac{\left(\left(\overline{\mathbf{G}} - \mathbf{G}(\mathbf{p})\right)^T \mathbf{D}^{-1}\mathbf{v}_n\right)^2}{\lambda_n} + \chi^2_{\text{prior}}, \tag{2.39}$$

where $\mathbf{D}$ is defined from $M_{\text{cov}} = \mathbf{D}M_{\text{corr}}\mathbf{D}$. The underestimation of the smaller λ_n leads to oversized contributions to χ^2 and a poorer fit. This effect is remarked upon and a remedy offered in appendix D of [88] which we outline here.

The basic idea is to compare the eigenvalues of the original correla-

tion matrix and bootstrapped copies of it. The bootstrap is a common resampling method used to generate statistics about a dataset. Given N data points, $N_{\rm boot}$ datasets are generated, each with N data points selected randomly *with replacement* from the original dataset. By considering a statistic over the bootstrapped copies of the data one can construct a bootstrap average, say, of that statistic.

In this case each bootstrap dataset has a set of eigenvalues, λ_n^i with $i = 1 \ldots N_{\rm boot}$. Averaging over the bootstrapped eigenvalues yields the quantities, $\lambda_n^{\rm boot}$, along with their uncertainties. Where the bootstrap-averaged eigenvalues fall below a certain threshold,

$$\lambda_n^{\rm boot} < (1 - \sqrt{2/N_G})\lambda_n^{\rm exact} \equiv \kappa \lambda_n^{\rm exact}, \tag{2.40}$$

the replacement, $\lambda_n \to \max(\lambda_n, \kappa\lambda_{\rm max})$, is made. This is the so-called SVD cut. It is a conservative replacement that improves the fit and increases the uncertainty of the best fit parameters. This can be seen explicitly by considering

$$G = \overline{G} + \delta{\rm G} \longrightarrow \overline{G} + \delta{\rm G} + \delta{\rm G}_{\rm SVD} \tag{2.41}$$

where $\delta{\rm G}_{\rm SVD}$ is the extra uncertainty induced by the SVD cut,

$$\begin{aligned} \delta{\rm G} &\equiv \sum_{n=1}^{N_G} z_n \sqrt{\lambda_n} {\rm D}\mathbf{v}_n, \\ \delta{\rm G}_{\rm SVD} &\equiv \sum_{\lambda_n < \kappa\lambda_{\rm max}} \tilde{z}_n \sqrt{\kappa\lambda_{\rm max} - \lambda_n} {\rm D}{\rm v}_n, \end{aligned} \tag{2.42}$$

Then the SVD-modified covariance data is

$$\begin{aligned}\langle(\delta G + \delta \mathrm{G_{SVD}})(\delta G + \delta \mathrm{G_{SVD}})^T\rangle & \\ &= \langle \delta G \delta G^T\rangle + \langle \delta G_{\mathrm{SVD}} \delta G_{\mathrm{SVD}}^T\rangle \\ &= \sum_n \max(\lambda_n, \kappa\lambda_{\max}) \mathbf{D}\mathbf{v}_n\mathbf{v}_n^T\mathbf{D},\end{aligned} \tag{2.43}$$

which clearly increases the uncertainty relative to $\langle(\delta G)(\delta G)^T\rangle$.

A robust fit should be insensitive to SVD noise, which can be added by sampling from $\delta \mathrm{G_{SVD}}$ and replacing

$$\delta \mathrm{G_{SVD}} \longrightarrow \delta \mathrm{G_{SVD}} + \mathrm{sample}(\delta \mathrm{G_{SVD}}) \tag{2.44}$$

before refitting. Fitted parameters before and after adding SVD noise should agree.

2.4.4 Criteria for a good fit

When evaluating a fit to the correlator data we rely on a set of goodness-of-fit parameters, $\{\chi^2_\nu, Q, \mathrm{logGBF}\}$.

The reduced chi-squared, χ^2_ν or $\overline{\chi}^2$, is the chi-squared per degree of freedom, $\chi^2_\nu \equiv \chi^2/\nu$. A fit is not considered good if it does not satisfy $\chi^2_\nu \lesssim 1$.

The Q value, also known as the p factor, is the probability that the χ^2 from our fit *could have been larger by chance*, assuming all the data are gaussian and consistent with each other. Good fits usually have $Q > 0.1$.

logGBF, the logarithm of the Gaussian Bayes Factor, is the loga-

rithm of the probability of obtaining the fit data by randomly sampling the fitted model, $\log P(\text{data}|\text{model})$. This quantity is useful for comparing fits of the same data to different models with different priors and fit functions. Taking the difference in this metric between two models and exponentiating produces the ratio of the probabilities that each model, randomly sampled, produced the data,

$$\exp\{(\text{fit.logGBF})_\text{A} - (\text{fit.logGBF})_\text{B}\} = \frac{P(\text{data}|\text{model A})}{P(\text{data}|\text{model B})}, \quad (2.45)$$

for two models labelled A and B. This ratio is known as the Bayes factor. Clearly if the Bayes factor is greater than 1 then model A is preferred to model B. Generally a sliding scale is employed when using Bayes factors to evaluate the relative strength of models. There is clearly a not insignificant element of subjectivity in the choice of thresholds. A not unreasonable heuristic has a Bayes factor greater than 100 being 'decisive', a factor of 20 being 'strong', and a factor of 3 being 'Barely worth mentioning'.

A seemingly good fit might still have to be discarded if it is not robust to changes in the fit parameters, such as the fitting range, SVD cut, or priors.

Much of the data analysis in this thesis was done using Peter Lepage's `corrfitter` library, which implements the statistical methods described in the previous section and many others [89]. All the python scripts used to perform the statistical analysis and generate the results in this thesis are available at https://github.com/gray95/lattice-analysis.

2.5 Extrapolating to the Real World

There are many ways in which simulations on the lattice are unphysical. Unphysical effects must be removed before a fair comparison can be made to the natural world. Measurements on lattices are done in discretised spacetime and a finite volume, giving rise to UV and IR effects respectively. Lattices often have heavier-than-physical pion masses and are isospin symmetric. To remove these unphysical effects extrapolations, sometimes in more than one parameter, to the physical point must be made. In most case these extrapolations are done simultaneously as in the combined continuum-chiral extrapolation in chapter 4 of this thesis.

The extrapolation to the continuum, $a \to 0$, can be done by measuring an observable on ensembles of varying lattice spacing, fitting the measurements to some $f(a)$, then reading off $f(0)$. The appropriate choice of f depends on the type of action and fermion used, and can vary by observable (through the interpolating operator). The HISQ action, being tree-level $\mathcal{O}(a^2)$ improved, generally has mild a^2 discretisation effects, meaning $f(a^2) = \sum_i c_i a^{2i}$ for small positive i is usually an appropriate fit form. However specific observables may mandate alternative fit forms, and there has been some discussion in the context of staggered fermions about whether discretisation effects at $a > 0.12$ fm are well understood [90].

The infinite volume limit, $L \to \infty$, similarly can be taken by measuring on ensembles of varying size, fitting to some $f(1/L)$ before reading off $f(0)$. An alternative approach is to calculate a finite vol-

ume correction at each a using an effective field theory,

$$\Delta\mathcal{O}_{FV} = \mathcal{O}^{(\mathrm{EFT})}(L=\infty) - \mathcal{O}(L=L). \tag{2.46}$$

This approach is taken with the precision calculations of the anomalous magnetic moment of the muon, where there are multiple alternative EFTs used to determine its FV properties [91, 77].

Simulations can be carried out at heavier-than-physical pion masses, $m_\pi^{\mathrm{phys}} = 140$ MeV, in the sea or valence sectors. In the sea their effect is small but significant and can be captured by a quark mass mistuning term in the continuum extrapolation function, see chapter 3 for more details. In the valence sector, provided the quarks are light enough, chiral PT can be used to fix the form of the extrapolation in m_q, see chapter 4 for more details.

Chapter 3

Heavy Hybrid Meson Spectroscopy

In this chapter we present results for the masses of the 1^{-+} and 1^{--} hybrid mesons in the charmonium sector based on lattice QCD calculations with staggered quarks. We preface our calculation with a short review of hybrid mesons. This review covers the definition of hybrid mesons, the models that have been used to try and understand them, previous lattice calculations, and the experimental evidence for their existence. The details of the simulation are described and the form of the hybrid operators used is discussed. The methods used to fit the correlators are outlined, in particular the GEVP method, and best fit parameters are listed. We conclude by presenting the results and then discussing them.

3.1 Introduction

Independently in the 60's, Gell-Mann and Zweig proposed the Quark Model [11, 12]. This model classifies the hadrons by their valence quark content and has proven successful at explaining experimental particle data. It splits the hadrons into two groups, mesons and baryons. Baryons are made up of three quarks, and mesons are made up of a quark-antiquark pair. Gell-Mann's use of the Quark Model to successfully predict the omega baryon in 1964 demonstrated to many its correctness.

In the Quark Model states are labelled by their J^{PC} quantum numbers. For $q\bar{q}$ mesons we have parity $P = (-)^{L+1}$, charge conjugation $C = (-)^{L+S}$ where L is orbital angular momentum, S is spin, and the usual rules apply for addition of angular momentum, $\vec{J} = \vec{L} + \vec{S}$. This leaves the disallowed combinations, $0^{--}, (odd)^{-+}, (even)^{+-}$, as the exotic quantum number states.

However, beginning in 2003 with the detection of the $\chi_{c1}(3872)$ ($J^{PC} = 1^{++}$), a series of resonances have been observed in the charmonium and bottomonium sectors that do not correspond neatly with Quark model states [92, 93]. Many competing non-Quark model explanations for these so-called XYZ states have been proposed, including (but not limited to) gluonic hadrons, bound states of more than 3 quarks, and hadronic molecules [94, 95, 96]. These XYZ states have many different J^{PC}, both exotic and non-exotic.

Well before the experimental discovery of these resonances some theorists had started exploring the possibility of particles with va-

lence gluons. These are the glueballs and the hybrids. Glueballs are composed of only gluons, and hybrids are states made of quarks and gluons. A hybrid meson is a meson *with an excited gluonic component*. Although hybrid mesons (and the other states noted) are exotic in the sense that they fall outside the well-tested Quark model, nothing in principle prevents $\bar{q}qg$ states in QCD. Hybrid mesons have been studied on the lattice for many decades [97, 98, 99, 100, 101, 102].

In the early 80's the first attempts at computing the properties of hybrids were carried out [103][1]. As the gluons can contribute to the quantum numbers of the hybrid mesons these states can have quantum numbers which are inaccessible to conventional $q\bar{q}$ states under the Quark Model. In particular the 1^{-+} quantum numbers are not accessible by conventional mesons. Finding such exotic states would show that the Quark Model is an incomplete description of the bound states allowed under QCD.

It is important to note that all states with the same quantum numbers can, in principle, mix with each other. So even though an exotic hybrid meson will not mix with a conventional meson it will mix with, say, a tetraquark state possessing the same J^{PC}. Baryons can have any quantum numbers, meaning they all could mix strongly with hybrid baryons of the same quantum numbers. However when the HadSpec collaboration examined hybrid and non-hybrid baryons they found only modest mixing, and were able to easily pick hybrid states out of a dense spectrum [104].

[1]Initially hybrids were called hermaphrodites or meiktons depending on the author, until an editor intervened and gave us the name we use today

3.2 Hybrid Mesons

3.2.1 On the Lattice

Following on from the very first calculation by Creutz [105], lattice methods matured, available computer power grew, and groups started performing more sophisticated calculations on increasingly large lattices.

Griffiths *et al.* investigated mesons with excited glue by computing adiabatic gluonic surfaces in SU(2), and found excited states, including exotics, about 800-900 MeV above the ground state [106].

Perantonis and Michael studied the potential between heavy quarks in the presence of an excited gluon field and used the Born-Oppenhimer approximation to extract hybrid charmonium (lightest, 4.19 GeV) and bottomonium (lightest, 10.81 GeV) masses[107].

The UKQCD Collaboration did a quenched calculation of the light hybrid mesons with $J^{PC} = 1^{-+}, 0^{+-}, 2^{+-}$, finding the 1^{-+} state the lightest at 2.0(2) GeV[98]. The MILC collaboration also performed a similar calculation near the charm quark mass finding a 1^{-+} charmonium state with a mass around 4.4 GeV[101]. They compared their lattice result with various models and found broad agreement. They also noted that mixing with tetraquarks should be partially suppressed by the quenched approximation.

Juge, Kuti and Morningstar performed a quenched calculation of a bottomonium hybrid and compared their result to that obtained using the Born-Oppenheimer expansion. They found the two approaches to be consistent and therefore evidence for a particular model interpre-

tation of hybrid bottomonium[108].

Liao And Manke went a step further and calculated the entire excited charmonium spectrum in the quenched approximation, including exotic states (via hybrid operators) and orbitally excited mesons up to $L = 3$ [109]. They found the 1^{-+} lying at 4.428(41) GeV, the 0^{+-} at 4.70(17) GeV, and the 2^{+-} at 4.895(88) GeV, with purely statistical errors.

The Hadron Spectrum Collaboration has performed many lattice calculations concerning the properties of mesons. Over many papers they have developed a series of techniques to more reliably extract excited state energies and to overcome the reduced symmetry of the lattice and assign continuum spin numbers. They have developed a quark field smearing algorithm (distillation) to optimise hadron creation operators [110]. They use a large basis of covariant derivative-based meson interpolating fields and a variational method. Throughout their studies they have been interested in the properties of exotic states in the charmonium sector. Initially they studied this sector with anisotropic lattices in the quenched approximation[111], then using 2+1 dynamical quarks[112], and finally with a less unphysical pion mass ($M_\pi = 240$ MeV)[102]. Their full charmonium spectrum is reproduced in figure 3.1, with possible hybrid states highlighted in red. They predict the lightest hybrid multiplet as consisting of the $(0, 1, 2)^{-+}$ and 1^{--} states.

The lattice has cubic symmetry with five irreps, A_1, A_2, E, T_1, T_2. The continuum however has infinitely many irreps labelled by j with dimension $2j+1$. States on the lattice can therefore be easily classified

under the irreps of the cubic group but not the J^{PC}. The mapping from the continuous to cubic symmetries is listed in table 3.1 up to $J = 4$. The Hadron Spectrum Collaboration navigate this problem by considering the values of vacuum-to-state matrix elements, known as overlaps or Z values, $\langle n|\mathcal{O}|0\rangle$. The operators HadSpec use have a 'memory' of the continuum spin from which they were subduced. Operators subduced from spin J are expected to overlap strongly *only* onto states of continuum spin J.

J	irreps
0	$A_1(1)$
1	$T_1(3)$
2	$T_2(3) \oplus E(2)$
3	$T_1(3) \oplus T_2(3) \oplus A_2(1)$
4	$A_1(1) \oplus T_1(3) \oplus T_2(3) \oplus E(2)$

Table 3.1: How the continuum spins, J, map onto the lattice irreps $\lambda(dim)$.

More recent calculations of hybrid static potentials have been carried out with lattice spacings as small as 0.040 fm, and interquark separations as small as 0.080 fm [113]. These lattice results combined with improved EFT methods promise improved spectra and mixing information.

3.2.2 Models

One might wonder why, if we can compute all the observables of interest on the lattice, do we bother creating and refining models of hybrid meson structure and dynamics? The answer is twofold, firstly it is resource intensive and therefore expensive to calculate large numbers of the needed quantities on the lattice. Secondly, and more importantly,

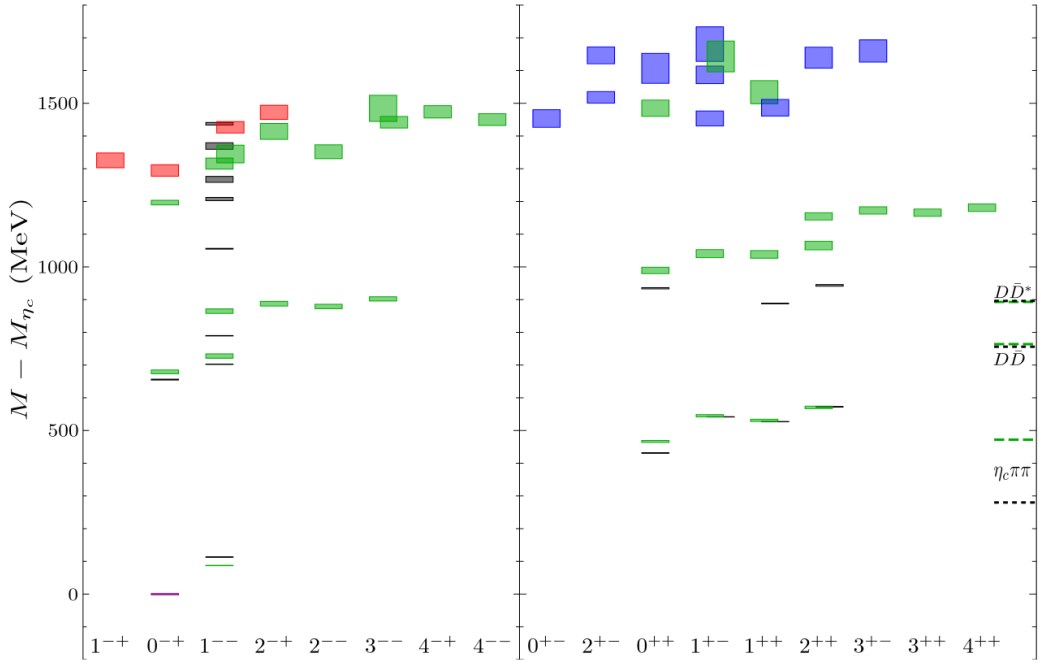

Figure 3.1: The charmonium spectrum computed by the Hadron Spectrum Collaboration[102]. The spectrum in individual channels is given, including exotic channels, with many excited states. The coloured boxes are the computed masses, the black lines the experimental values from the PDG summary tables. The size of the boxes corresponds to the uncertainty in their value. The red boxes correspond to the lightest hybrid multiplet. Note that the masses are given as differences to the pseudoscalar η_c mass.

some complicated quantities relevant to hybrid physics are beyond the reach of current lattice theory, like hybrid scattering amplitudes. A good model should inform and aid in the interpretation of experimental results. Lattice results can help us choose which models represent a more accurate picture of the hybrid meson. These models may then provide insight into the appropriate degrees of freedom in a QCD calculation. Hybrid models can be split up into two groups depending on how they treat the gluonic degrees of freedom. One type treats the gluons as quasiparticles, the other as collective and non-local in nature.

Bag Models

Bag models were introduced as a way to explain the properties of hadrons [114, 115]. In Bag models hybrids are thought of as a quark-antiquark pair and a gluon field placed in a spherical vacuum bubble with appropriate boundary conditions, producing either transverse chromoelectric (TE) or transverse chromomagnetic (TM) modes [103]. The TE modes were found to be lighter. It was realised that heavy quarks would not be confined in the right way in a spherical bag and so the bag should be allowed to deform due to the heavy quark-antiquark pair. These models were called the 'Budapest' variant. The derived adiabatic energy surfaces were used in a two body Schrödinger equation to give heavy hybrid meson mass estimates of 3.9 and 10.45 GeV for the lightest charmonium and bottomonium hybrids respectively.

Juge, Kuti and Morningstar used the Budapest variant to compare model adiabatic energy surfaces in the static quark limit to the lattice

results, finding surprisingly good agreement (see Figure 3.2) [116]. Since they worked in the static limit their results are of relevance to heavy hybrids.

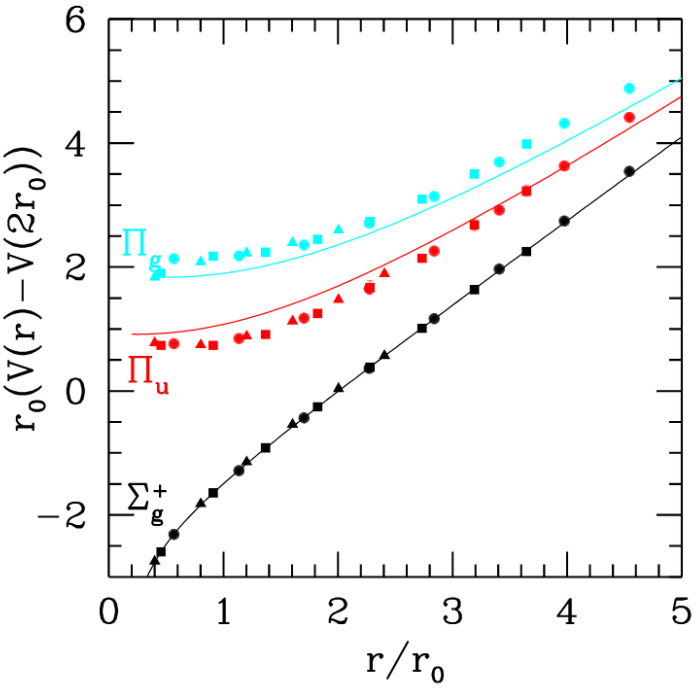

Figure 3.2: From [116]. The bag model predicted potentials are the solid lines and the points are the lattice results. The different lines correspond to the different gluon field configurations and are labelled by their quantum numbers.

Bag models are qualitatively simple and easy to visualise. However they suffer from problems that make their application confused. The centre of mass introduces unphysical degrees of freedom, leading to spurious exited states. Gluon self-energies can be ambiguous. Interactions between the bag boundary and the quarks and gluons and the subsequent change in bag shape are difficult to determine. An issue of interpretation arises from the intrinsic ambiguity between the gluonic degrees of freedom and the bag.

Flux Tube Models

The Flux Tube model was developed by Paton and Isgur in response to bag models [117]. They insisted on using nonperturbative degrees of freedom as opposed to the perturbative gluons of the bag models. They built such a model by taking the lattice QCD Hamiltonian and truncating it with a series of approximations. Thus, in their model the gluons bear similarities to the gluons of the lattice and can be thought of as link variables connecting sites on which quarks live.

They simplified the dynamics by assuming an adiabatic separation of quark and gluon degrees of freedom, ignoring topological mixing such as loop breaking or deformation, and working in the non-relativistic limit.

They modelled the link variables with spinless, colourless particles called 'beads' that undergo small oscillations in a linear potential [117]. Gluons are associated with the phonon modes of this system and so hybrids are constructed by specifying the gluonic states with phonon operators (apparent in the Hamiltonian) and combining these with quark operators.

They then solved a model Hamiltonian of quark motion on a single phonon excited surface and so obtained hybrid meson masses.

$$H = -\frac{1}{2\mu}\frac{\partial^2}{\partial R^2} + \frac{L(L+1) - \lambda^2}{2\mu R^2} - \frac{4\alpha_s}{3R} + \frac{\pi}{R}(1 - e^{-f\sqrt{b}R}) \qquad (3.1)$$

After estimating the effects of adiabatic surface mixing this gave a final value of 4.3 GeV for $c\bar{c}g$ and 10.8 GeV for $b\bar{b}g$.

The lightest flux tube multiplet is larger than the lattice prediction, predicting the usual $(0,1,2)^{-+}, 1^{--}$ *and* $(0,1,2)^{+-}, 1^{++}$ hybrid states. The lowest energy TE mode bag models yield a multiplet in agreement with the lattice. The bag model, being perturbative, does well at small quark separation but poorly at large separation, while the flux tube model works over a wider range of distances.

Many models are ruled out early on because they can't produce the required quantum numbers for the adiabatic potentials. Spinless gluons are ruled out because they don't contain sufficient degrees of freedom to reproduce the spectrum. Alternatively a $J^P = 1^-$ gluon can explain the lightest multiplet if it's in relative P wave with an S wave $q\bar{q}$. The heavier multiplet then corresponds to the the gluon in relative P wave with a P wave $q\bar{q}$.

Born-Oppenheimer Approximation

In the case of heavy quarkonium there is a natural separation of energy scales between the quark and gluon degrees of freedom. The nonperturbative gluon dynamics happens at Λ_{QCD}, while the heavy quark-antiquark pair's energy scale is at $mv^2 \ll \Lambda_{\mathrm{QCD}}$. This separation of scales is analogous to that between the electrons and nucleus of an atom, and has led to the application of the Born-Oppenheimer approximation (BO) on heavy quarkonium systems, including hybrids. BOEFT, an EFT formulation of the BO has been used, with lattice data as input, to calculate the quarkonium hybrid spectrum [118, 119, 120]. This approach has also been used to gain information about hybrids beyond the spectrum including mixing with standard

quarkonium, spin-dependent contributions, and semi-inclusive decays.

For completeness the masses of hybrid mesons have also been calculated with a technique called QCD sum rules [121].

3.2.3 Phenomenology

By calculating transition matrix elements for hybrid transitions we can gain a better understanding of these states and the experimental data collected at various colliders. In order to identify an observed exotic state with a lattice state it helps to not only have the masses agree but the widths and decay rates too. Calculating transitions can aid in our experimental search by discerning between different exotics (glueball and hybrid say) that may decay differently. The light hybrid is expected to partake in the three body decay $1^{-+} \to \rho\pi \to \pi\pi\pi$. Three body decays are very hard to simulate.

McNeile et al. did the first study of a hadronic transition on the lattice, constraining themselves to the heavy quark limit (so more relevant to the bottomonium sector) and using two flavours of light dynamical quarks [122]. They focused on the 1^{-+} and argued that the decay of this heavy hybrid meson into a heavy non-exotic state and a light quark meson is particularly important. They deduced this by arguing that the decay into two S wave mesons is forbidden by the symmetries of the system and that decay into a $Q\bar{q}$ S wave and a $q\bar{Q}$ P wave is forbidden by energy considerations, leaving as the only allowed transition the de-excitation of the gluon field with an accompanying emitted light meson. They discovered a small transition amplitude for the emission of a pseudoscalar meson and a much larger amplitude

for the emission of a scalar meson, $b\bar{b}g(1^{-+}) \longrightarrow \eta_b\eta(s\bar{s})(< 1$ MeV), $b\bar{b}g(1^{-+}) \longrightarrow \chi_b\sigma(s\bar{s})(61(14)$ MeV).

HadSpec have also calculated radiative transition rates for heavy hybrids [123]. Specifically they performed the first lattice calculation of the exotic $1^{-+}\eta_{c1}$ radiative decay, $\eta_{c1} \longrightarrow J/\psi\gamma$, finding a large partial width ~ 100 keV. To do this they computed three-point correlators on quenched anisotropic lattices. They found this process dominated by a magnetic dipole transition and noted that the extra gluonic degree of freedom in a hybrid allows such a transition without spin-flip (spin-flip being suppressed by the large charm quark mass).

For completeness, we briefly discuss the possible hadronic decays of hybrid charm mesons. There are possible string breaking-like decays where the hybrid meson can decay into pairs such as $\overline{D}D$, or two P-wave D mesons, or a P-wave D and a S-wave D, as well as similar channels with charm-strange mesons. There is a selection rule in the heavy quark limit [124] (and some quark models [125]) that a hybrid meson can not decay into two S-wave mesons. It is possible for the hybrid meson to decay to a standard charmonium meson with a light meson and there is a lattice QCD calculation in the heavy quark limit [126].

3.2.4 Experimental status

Starting in 2002 a series of charmonium-like resonances were discovered at BaBar, Belle and other experiments. Some of these states didn't fit neatly into the levels predicted by the Quark Model, having either measurably exotic quantum numbers or non-exotic quantum

numbers with other unconventional properties (branching ratios etc).

As an example consider the $\psi(4260)$ (previously called $Y(4260)$), labelled ψ because it shares the same quantum numbers as the conventional vector meson, 1^{--}. Lying between the $2D$ and $4S$ vectors' quark model predicted masses implies this is a non $q\bar{q}$ state. Its decay to e^+e^- is smaller than other vector charmonia whilst its decay to $J/\psi\pi^+\pi^-$ is larger than other vector charmonia. The mass is about ~ 1 GeV higher than the ground state J/ψ, about what you'd expect for a gluonic excitation. The HadSpec group found a vector hybrid at this mass, lending weight to the hypothesis that this is a hybrid. There are competing models that seek to explain this resonance as hadrocharmonium[2] or a diquark-antidiquark state. It could be that this state is a mixture of all these alternatives.

There are many unexplained resonances with $J^{PC} = 1^{--}$, where charmonium hybrid mesons may occur. See the review by Brambilla et al. [96]. For example it has been speculated that the $\psi(4230)$ is a hybrid meson, but confirmation will require accurate lattice QCD calculations.

Relevant experimental searches include the upcoming PANDA experiment at FAIR, which will search for evidence of gluonic excitations in the charmed hadron spectrum, and the GlueX experiment at Jefferson Lab, which has a complementary search in the light sector [127, 128]. Accurate lattice QCD calculations of the properties of the hybrid mesons in charmonium may encourage the LHCb collaboration to search for them.

[2]Hadroquarkonium describes a compact state of quarkonium embedded in an excited light meson by a QCD analog of the Van der Waals force.

3.3 Simulation Details

The advantages of using staggered fermions is that the discretisation errors are small and the meson spectrum has been thoroughly investigated. The HPQCD collaboration has done many comparisons between lattice calculations and experiment in the charmonium system [129, 130]. There are some disadvantages to using staggered fermions over other fermion formulations. For example, because the staggered correlators have a contribution from the parity partner, the hybrid mesons are the first excited state, but in Wilson like formulations the hybrid meson is the ground state. The initial goal of this project was to check whether it was possible to get accurate results for the mass of hybrid mesons made from charm quarks using staggered fermions.

3.3.1 Interpolating operators for hybrids

Since hybrids have an excited gluonic component the operators which we would expect to couple to them include the field strength tensor, F_{ij}^{ab}, whose components are the chromoelectric and chromomagnetic fields ($\frac{1}{2}\epsilon_{ijk}F_{jk} = B_i$). These are contracted, over the colour indices, with the usual fermion bilinears (the quark-antiquark pair is in a colour octet).

Wilson fermion hybrids

According to the Hadron Spectrum Collaboration the lightest hybrid mesons in the charmonium sector are the $\{1^{-+}, 0_H^{-+}, 1_H^{--}, 2_H^{-+}\}$ states

[102]. The last three states have a subscript H identifying them as hybrids because they're not exotic quantum number states like the 1^{-+}. Since hybrids are defined as hadrons with an excited gluonic component, we can write down mesonic operators for these states,

$$\begin{aligned} 1^{-+} &: \epsilon_{ijk}\overline{\psi}\gamma_j B_k \psi \\ 1_H^{--} &: \overline{\psi}\gamma_5 B_i \psi \\ 0_H^{-+} &: \overline{\psi}\gamma_i B_i \psi \\ 2_H^{-+} &: |\epsilon_{ijk}|\overline{\psi}\gamma_5\gamma_j B_k \psi, \end{aligned} \tag{3.2}$$

where ϵ_{ijk} is the antisymmetric levi-civita symbol and colour indices are omitted. Other hybrid-like operators are given in table 3.2, including examples with the chromoelectric field $E_i = F_{0i}$.

J^{PC}	Operator	mnemonic
1^{-+}	$\overline{\psi}\gamma_0 F_{0i}\psi$	$J_B \otimes E$
1^{-+}	$\overline{\psi}\gamma_4\gamma_5\epsilon_{ijk}\gamma_j F_{0k}\psi$	$b_1 \otimes E$
1^{--}	$\overline{\psi}\psi F_{0i}$	$1 \otimes E$
1^{--}	$\lvert\epsilon_{ijk}\rvert\lvert\epsilon_{klm}\rvert\overline{\psi}\gamma_j F_{lm}\psi$	$\rho \otimes D$

Table 3.2: Alternative operators involving the field strength tensor that are expected to couple to the 1^{-+} and 1^{--} hybrid states.

Staggered Transformation

The majority of the results from lattice QCD for the masses of hybrid mesons have used clover or Wilson fermions. There has been one calculation by the MILC collaboration [99] using staggered fermions, which computed the mass of the 1^{-+} hybrid meson with light and strange quarks. The previous MILC calculation used the taste singlet non-local ρ when constructing hybrid operators to minimize taste

breaking [99]. We use the local ρ operator because taste breaking is less of an issue with charm quarks and local operators can be less noisy than non-local operators.

As we are using staggered fermions we replace the γ matrices with phases. These phases, along with the F_{ij}^{ab}, determine the quantum numbers of the operators. In the staggered basis the operators also have a taste assignment. Taste breaking effects should drop out in the continuum limit.

operator	J^{PC}	PP	Phase
$\gamma_5 \otimes \gamma_5$	0^{-+}	0^{+-}	1
$\gamma_0\gamma_5 \otimes \gamma_0\gamma_5$	0^{-+}	0^{++}	$(-1)^{x+y+z+t}$
$\gamma_i \otimes \gamma_i$	1^{--}	1^{+-}	$(-1)^{i}$
$\gamma_0\gamma_i \otimes \gamma_0\gamma_i$	1^{--}	1^{++}	$(-1)^{x+y+z+t+i}$

Table 3.3: Phases associated to local staggered currents of the given quantum numbers.

The effect of the transformation to staggered fermions is to replace Dirac's γ matrices with phases, see table 3.3. Operators are classified by their spin $\otimes$ taste. In the staggered formalism the local hybrid operators of equation 3.2 become

$$\begin{aligned}
1^{-+} &: \epsilon_{ijk}\overline{\psi}\gamma_j B_k\psi \quad \longrightarrow \quad \gamma_i \otimes \gamma_i : \overline{\chi}\epsilon_{ijk}(-1)^{x_j}B_k\chi \\
1_H^{--} &: \overline{\psi}\gamma_5 B_i\psi \quad \longrightarrow \quad \gamma_5 \otimes \gamma_5 : \overline{\chi}B_i\chi \\
0_H^{-+} &: \overline{\psi}\gamma_i B_i\psi \quad \longrightarrow \quad \gamma_i \otimes \gamma_i : \overline{\chi}(-1)^{x_i}B_i\chi \\
2_H^{-+} &: |\epsilon_{ijk}|\overline{\psi}\gamma_j B_k\psi \quad \longrightarrow \quad \gamma_i \otimes \gamma_i : \overline{\chi}|\epsilon_{ijk}|(-1)^{x_j}B_k\chi \quad ,
\end{aligned} \tag{3.3}$$

where we have given the 'spin $\otimes$ taste' assignment for the operators formed from staggered fields χ on the right. All the results in this chapter are produced using these 1^{-+} and 1_H^{--} operators. We have

neglected disentangling states due to the reduced cubic symmetry of the lattice, such as 1^{-+} with 4^{-+} [131].

We do not present any results for non-local hybrid operators. Examples of such operators in the staggered formalism are

$$\begin{aligned} 1^{-+} &: \gamma_i \otimes 1 : \overline{\chi}\epsilon_{ijk}(\eta_j D_j B_k + B_k \eta_j D_j)\chi \\ 0_H^{-+} &: \gamma_i \otimes 1 : \overline{\chi}(\eta_i D_i B_i + B_i \eta_i D_i)\chi \\ 2_H^{-+} &: \gamma_i \otimes 1 : \overline{\chi}|\epsilon_{ijk}|(\eta_j D_j B_k + B_k \eta_j D_j)\chi, \end{aligned} \tag{3.4}$$

see [33] for the taste singlet ρ operator.

We use gauge fields generated with the Highly Improved Staggered Quark (HISQ) action [132] with $N_f = 2+1+1$ sea quarks. The gauge configurations were provided courtesy of the MILC Collaboration [133, 134]. The lattice spacing is set using w_0 with the value calculated by HPQCD [79]. In table 3.4 the ensembles used are listed. We measured 1^{-+} correlators over all the ensembles in table 3.4, and 1^{--} correlators on just the f-5 ensemble. We used the MILC code to do the calculations. We modified the existing hybrid operators in the MILC code and tested the correlators against our own implementation in the Grid library [135]. In this analysis all the operators were used as point sources when constructing the correlators.

The correlators of hybrid meson operators are typically very noisy. We therefore employ a series of well-established techniques to reduce this noise. On each ensemble we average the correlators over 16 evenly spaced (starting at $t = 0$) time sources and 3 polarisations (x, y, z). We apply covariant smearing to the quarks. We apply APE smearing

name	size	a (fm)	$M_\pi L$	M_π (MeV)	am_c^{sea}	cfgs
very coarse (vc)	32^3x48	0.15088(79)	3.30	131.0(1)	0.8447	1505
coarse (c-10)	32^3x64	0.12225(65)	4.29	216.9(2)	0.628	1000
coarse-phys (c)	48^3x64	0.12121(64)	3.88	131.7(1)	0.643	1059
fine (f-5)	32^3x96	0.09023(48)	4.50	312.7(6)	0.440	1008
fine-phys (f)	64^3x96	0.08787(46)	3.66	128.2(1)	0.450	620

Table 3.4: The 5 lattice ensembles used. Both the f-5 and c-10 ensembles are at heavier than physical pion masses, while the others are at the physical point. The lattice spacings are determined from w_0 and w_0/a, measured by HPQCD [79, 91]. The tuned valence charm quark masses are from [63], and M_π is from [134].

on the gauge links in the field strength tensor and in the gaussian smearing on the quarks. We set the smearing parameters to the same values used in the charmonium analysis in [136]. DeTar and Lee report on using variational smearing with staggered fermions [137].

In figures 3.3 and 3.4 we plot fractional errors for the 1^{-+} hybrid correlator, 1^{--} hybrid correlator, and the $\overline{\psi}\gamma_i\psi$ correlator with charm quarks. The hybrid correlators are considerably more noisy than the conventional vector correlator, with the signal becoming very noisy by t=8. In figure 3.4 we also compare the fractional error of the 1^{-+} hybrid correlator with the estimate from Lepage [85], which implies it should be proportional to $\exp\big(-(M_H - M_{\eta_c})t\big)$.

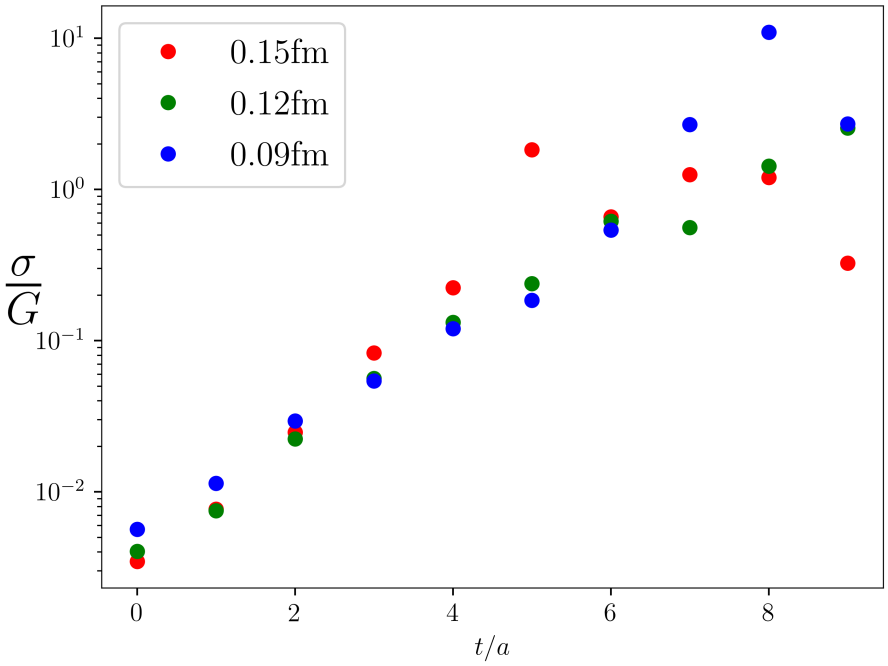

Figure 3.3: The fractional error of the unsmeared 1^{-+} hybrid correlators on each of the physical ensembles.

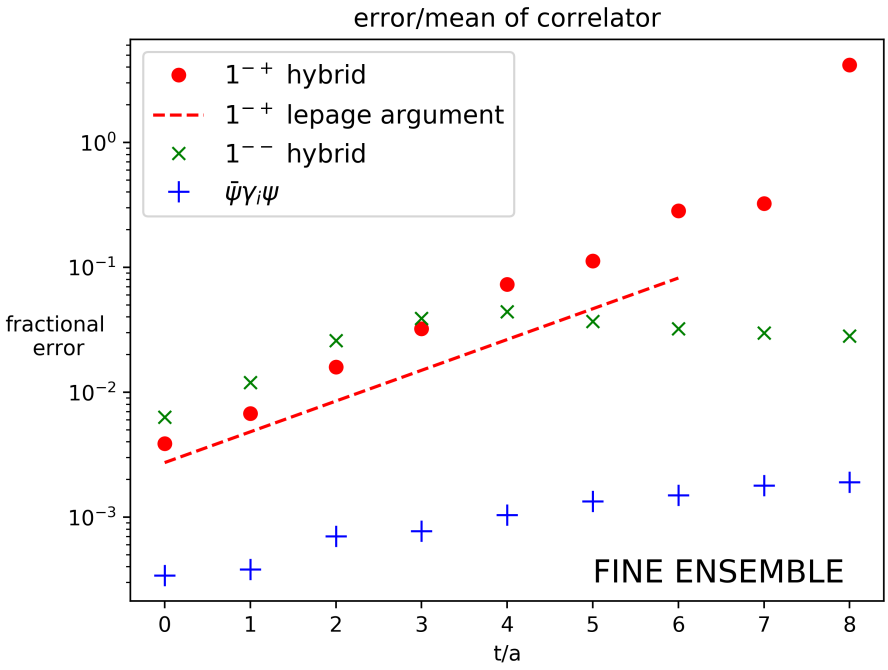

Figure 3.4: The error/mean of correlators against time for 1^{-+}, 1^{--} hybrid and conventional vector operators on the unphysical fine ensemble. We include the predicted fractional error from an argument by Lepage, using the fitted hybrid mass and experimental pseudoscalar mass.

3.4 Fitting Procedure

The measured correlators can be formed into a matrix, turning the problem of fitting them into a GEVP. For the 1^{-+} analysis we use a 2-operator basis, the hybrid operator with and without smearing, to produce a 2×2 matrix of correlators,

$$\begin{pmatrix} \langle HH \rangle & \langle Hh \rangle \\ \langle hH \rangle & \langle hh \rangle \end{pmatrix}, \tag{3.5}$$

where H/h is the unsmeared/smeared 1^{-+} operator. See chapter 2 for details on how the energies and amplitudes are extracted from this matrix of correlators.

The effective masses, M_{eff}, on the physical coarse ensemble are shown in figure 3.5. For the definition of M_{eff} see equation 4.20 in chapter 4. Although it is obscured a little by the noisiness of the correlators it does appear that each correlator has plateaus in M_{eff} that agree with each other within uncertainties. The smeared correlators plateau earlier than the unsmeared correlator and their uncertainties also grow at a slower rate.

Our fitting procedure is as follows: We choose a time, t_0, and use it to generate priors by diagonalising the correlator matrix with the eigenvectors associated to the solution of the GEVP at times t_0 and t_0+2. In this way we generate the priors from the data, we do not put them in by hand. These data driven priors are listed in table 3.5. The same prior is used for the oscillating and non-oscillating ground state masses. Due to the noisiness of the correlators we find $t_0 = 1$ or 3 is

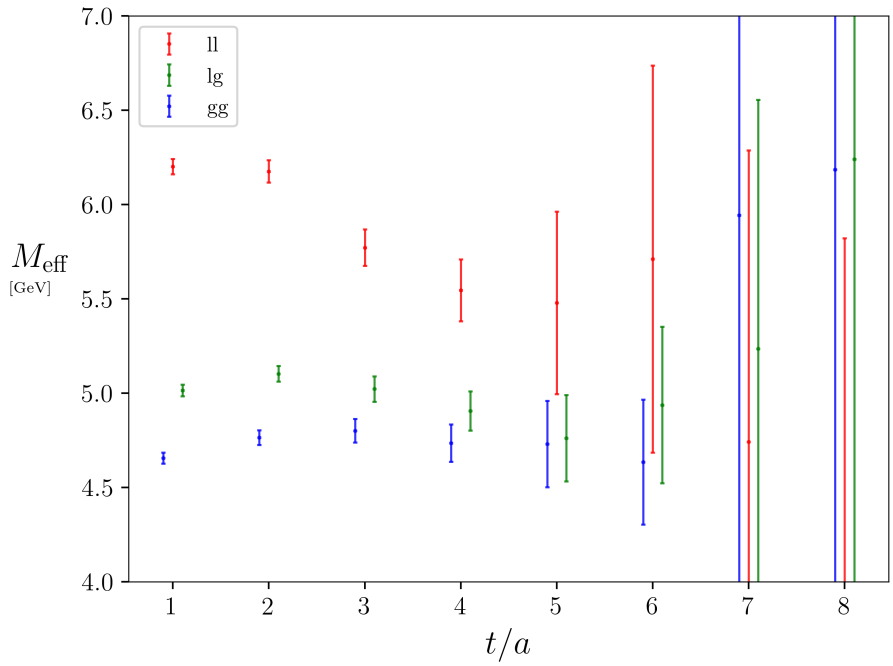

Figure 3.5: The effective masses in physical units of the local-local (ll), local-smeared (lg), and smeared-smeared (gg) 1^{-+} hybrid correlators on the physical coarse (0.12fm) ensemble.

usually a good choice, with results depending only weakly on t_0. The larger value of $t_0 = 3$ on the f-5 ensemble leads to a wider prior, but the effect on the fit compared to using $t_0 = 1$ is small and well below 1σ.

	B	t_0	prior(E_1, E_{o1})	prior (GeV)	fit/prior(E_1)	fit/prior(E_{o1})
vc	3	1	2.68(94)	3.5(1.2)	0.066	0.14
c-10	2	1	2.83(39)	4.57(60)	0.069	0.49
c	3	1	2.81(37)	4.57(63)	0.11	0.54
f-5	2	3	2.1(1.3)	4.7(2.1)	0.018	0.075
f	2	1	2.10(94)	4.6(2.8)	0.014	0.084

Table 3.5: Priors in the 1^{-+} analysis. The second column lists the bin size, B. The fourth column lists the prior for the non-oscillating (E_1) and oscillating (E_{o1}) ground states, generated from the correlator matrix at timeslices t_0, t_0+2. The fifth column lists the priors in physical units. The last two columns list the ratio of the width of the fitted masses to the width of the corresponding prior.

We then apply an SVD cut and fit the data using a model consisting

of 9+9 exponentials over a specified time region,

$$\sum_{i=1}^{9} A_i e^{-E_i t} + A_{io}(-1)^t e^{-E_{io} t}. \tag{3.6}$$

For a discussion on how the SVD cut is chosen see the analysis of the muon anomaly in chapter 4. The staggered formalism requires a parity partner (PP) state, which oscillates in time, to be included in the fit model. For the 1^{-+} channel the quantum numbers of the parity partner are 1^{++}. We vary the fit range until the goodness of fit parameters indicate an acceptable fit. Where there are multiple good choices for the fit parameters we choose the one with the smaller hybrid mass uncertainty. The best-fit parameters are given in table 3.6. On some of the ensembles we use a smaller time range for the off-diagonal correlators because later time slices tend to be more highly correlated and removing these from the simultaneous fit can ease the fitting procedure and result in better χ^2. This was not necessary on the two fine ensembles.

Ensemble	fit range	SVD cut	$\chi^2_\nu/(\chi^2_\nu)^*$	Q/Q^*
vc	[1-8]†:[1-4]	2.3×10^{-7}	0.86/1.3	0.63/0.15
c-10	[1-5]:[1-4]	2.9×10^{-5}	0.75/1.1	0.73/0.32
c	[1-5]:[1-4]	2.5×10^{-5}	0.53/1.5	0.92/0.11
f-5	[2-12]:[2-12]	5.3×10^{-4}	0.76/0.98	0.83/0.49
f	[1-20]:[1-20]	6.6×10^{-4}	0.94/1.1	0.61/0.27

Table 3.6: Summary of 1^{-+} fit parameters. Column 2 lists the range of times included in the fit, the second range is used for the off-diagonal correlators. Column three lists the SVD cuts. Columns four and five list the reduced χ^2 and the Q value of the fit, respectively. Starred (*) quantities are goodness of fit parameters after prior and SVD noise have been added.
† On the vc ensemble the $t = 5$ timeslice was removed.

We use a large number of exponentials in our fit models, $N = 9$. These fits are stable even if the number of data points fitted is $\lesssim 9$ because the fitting procedure is iterative, looping over $1 \ldots N$, and the priors prevent unreasonably large coefficients A_i, A_{io}. Past $N = 3$ the fitted parameters generally reproduce the prior, suggesting 3+3 exponentials is sufficient to describe the data. This is illustrated in figure 3.6, where the masses on the unphysical fine ensemble (f-5) are plotted against the number of exponentials in the fit model. Even though most of the terms in the fit function are not necessary when fitting the data, we leave the fit function unchanged as their inclusion does not hurt the quality of the fit.

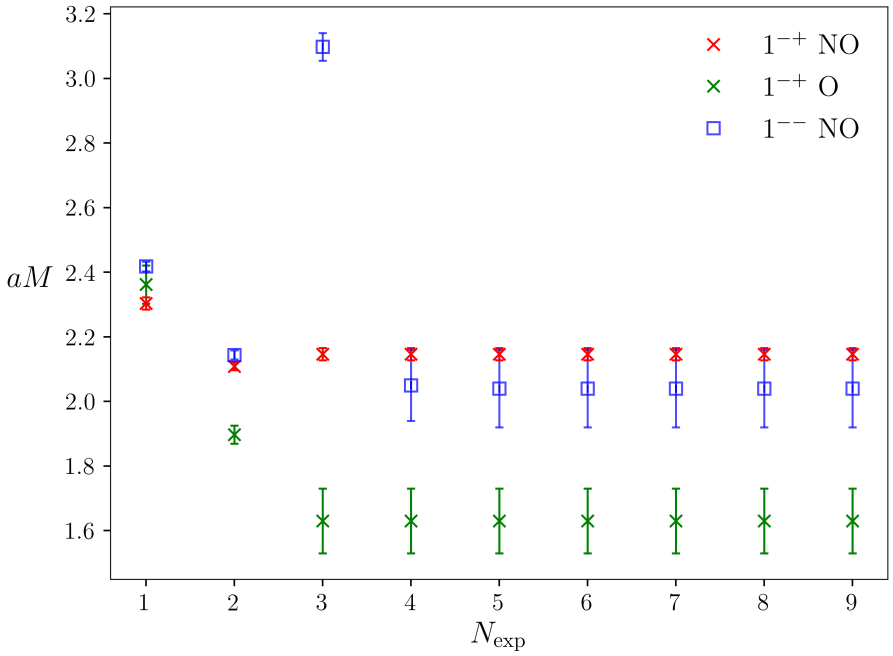

Figure 3.6: Fitted $1^{-+}/1^{--}$ oscillating (O) and non-oscillating (NO) masses against number of exponentials on the f-5 ensemble. The 1^{--} NO mass comes from a 2x2 fit with just the hybrid operators.

We can test whether our fits are robust to changes in the fitting region by varying (only) t_{min}. Figure 3.7 shows that the fitted masses on the f-5 ensemble agree within uncertainties as t_{min} is varied and,

as one expects, the uncertainty in the mass grows as t_{min} is increased and the fit region is shrunk.

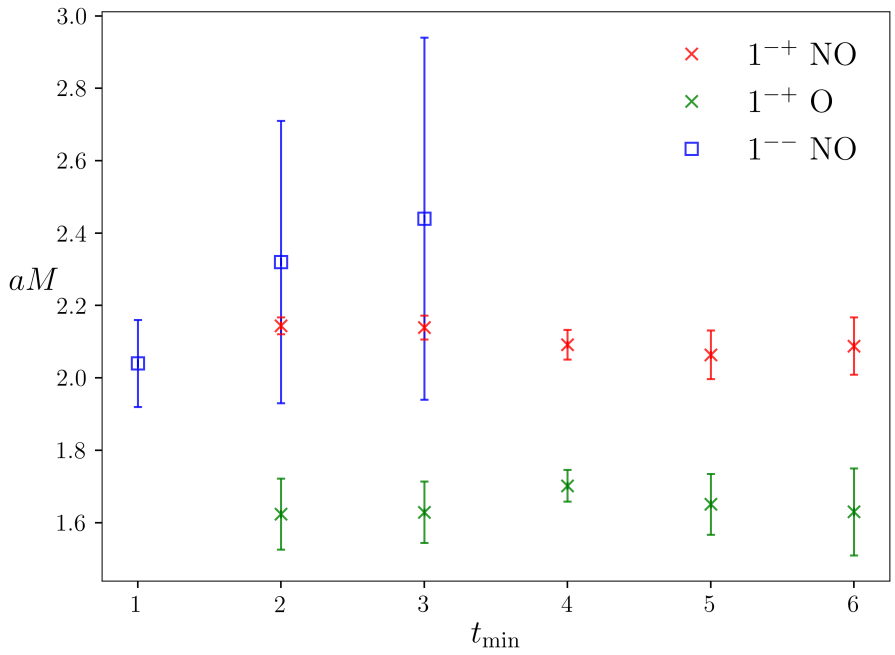

Figure 3.7: Variation of the fitted $1^{-+}/1^{--}$ oscillating (O) and non-oscillating (NO) masses with t_{min} on the f-5 ensemble. Beyond $t_{\text{min}}=3$ we could not extract a mass for the 1^{--} NO hybrid state. The 1^{--} NO mass comes from a 2x2 fit with just the hybrid operators.

We add noise to the SVD cut and the priors before refitting, as discussed in chapter 2, and we redo the fits after binning the correlators [88]. To be considered a robust fit we require $\chi^2_\nu \sim 1$ after adding noise, and the binned results to agree within uncertainties to the unbinned results. Table 3.6 shows that the goodness-of-fit parameters indicate good fits after adding SVD and prior noise. Figure 3.8 shows that the fitted masses are stable on the f-5 ensemble when the svdcut is varied over several orders of magnitude while holding the other fit parameters fixed.

In table 3.5 we list the bin sizes used in the final fits. Given the size of our ensembles we can't go much beyond $B = 3$ before we have

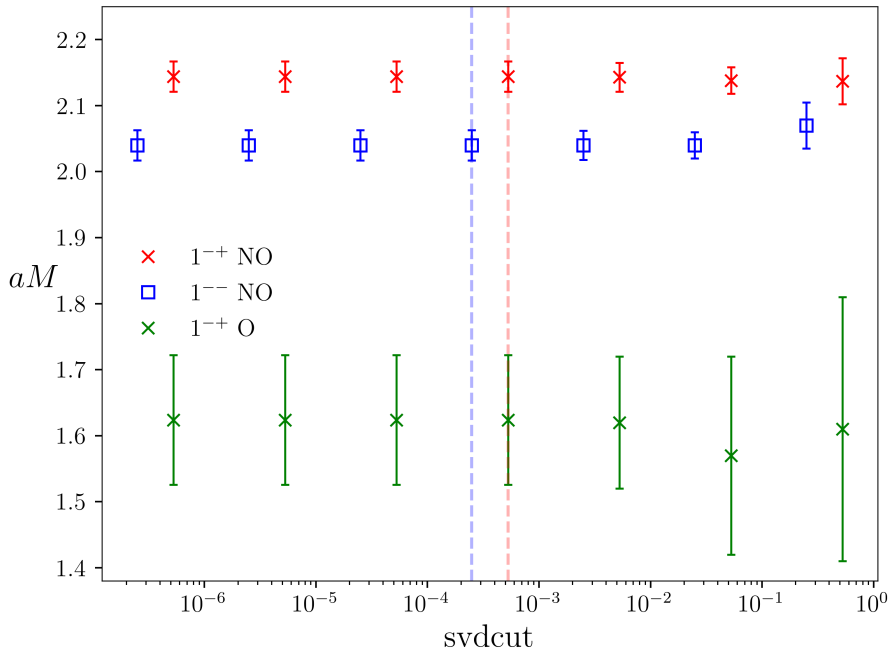

Figure 3.8: Variation of the fitted $1^{-+}/1^{--}$ masses with svdcut on the 'f-5' ensemble. The dashed lines indicate the svdcuts used in the final fit. The 1^{--} NO mass comes from a 2x2 fit with just the hybrid operators.

too few correlators left over. Also in table 3.5 we show the ratio of the widths of the fitted masses to their priors on each ensemble. Across all the ensembles both the NO and O fitted masses are narrower, some much narrower, than their priors. This suggests the results of the fit are driven by the data and not the prior. Figure 3.9 illustrates the quality of our fit on the unphysical fine ensemble, showing that the data and fit agreeing to within 1σ across the fitting range.

To examine the 1^{--} hybrid state we perform a very similar GEVP analysis, with the main difference being an expanded 4-operator basis; the standard vector operator J, the hybrid operator H, and their

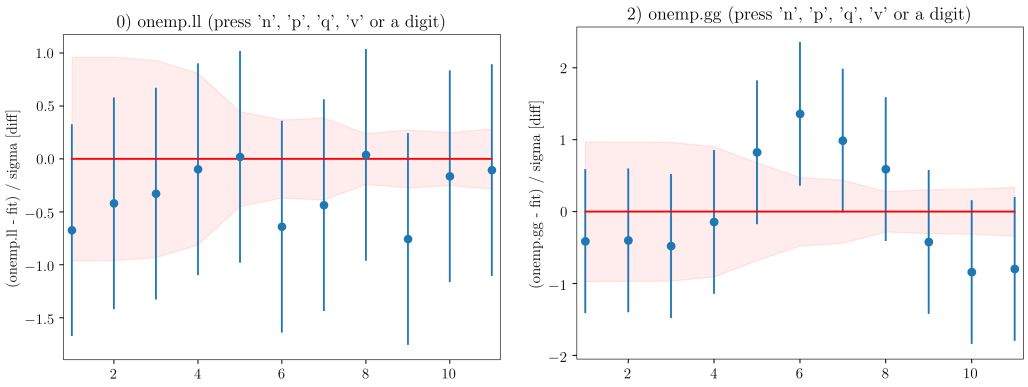

Figure 3.9: Fractional difference between the data and fit against time expressed in standard deviations for the unsmeared HH correlator on the f-5 ensemble. The red shaded region shows the uncertainty of the fit model for the best-fit parameters. The blue points are the correlator data.

smeared (j, h) counterparts. The 4x4 matrix of correlators is then

$$\begin{pmatrix} \langle HH \rangle & \langle HJ \rangle & \langle Hh \rangle & \langle Hj \rangle \\ \langle JH \rangle & \langle JJ \rangle & \langle Jh \rangle & \langle Jj \rangle \\ \langle hH \rangle & \langle hJ \rangle & \langle hh \rangle & \langle hj \rangle \\ \langle jH \rangle & \langle jJ \rangle & \langle jh \rangle & \langle jj \rangle \end{pmatrix}. \tag{3.7}$$

The effective masses, M_{eff}, on the f-5 ensemble are shown in figure 3.10. All the correlators, whether formed from the vector hybrid or conventional vector operators, have an M_{eff} that has a plateau around the mass of the J/ψ at 3.1 GeV. The higher energy states in the hybrid correlators seem to become dominated by this conventional charmonium state around $t=8$. This accords with the fractional error of the correlator shown in figure 3.4.

The rest of the analysis proceeds along similar lines to the 1^{-+} analysis. We can also fit the 2x2 sub-matrices formed by restricting the operator basis to either the standard vector operators (J,j), or

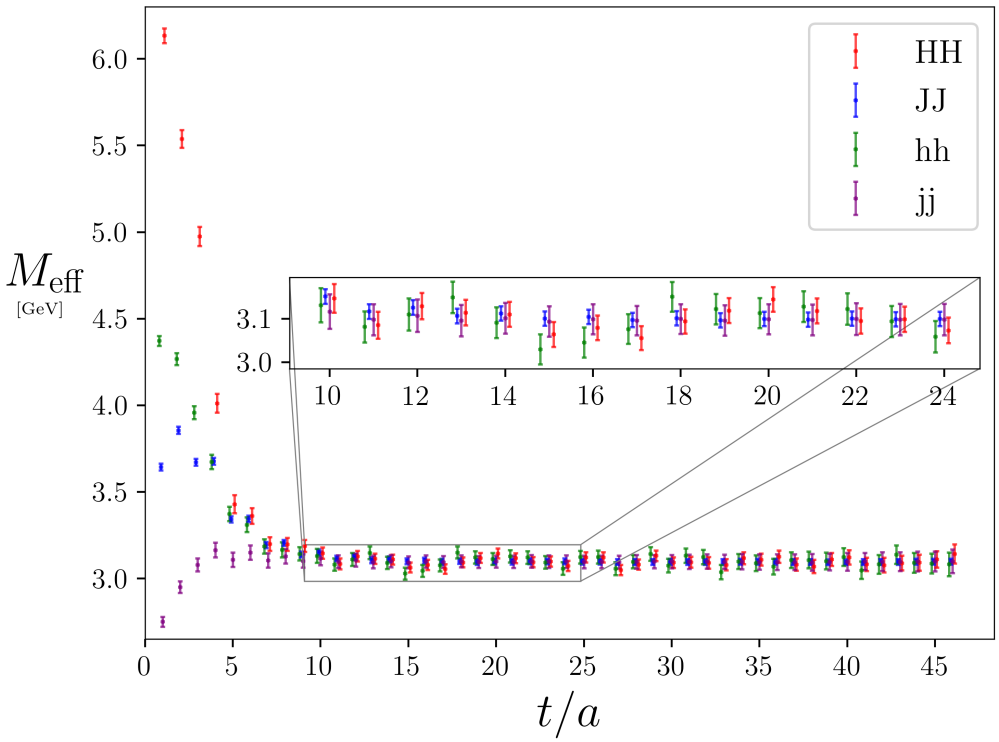

Figure 3.10: The effective mass of the hybrid local-local (HH), vector local-local (JJ), hybrid smeared-smeared (hh), and vector smeared-smeared (jj) 1^{--} correlators on the f-5 ensemble.

the hybrid operators (H,h). Fitting these smaller matrices is easier and can provide guidance on the best fit parameters to use in the 4x4 fit. They are also useful as cross-checks, the 2x2 standard vector fit should reproduce the conventional charmonium spectrum in the 1^{--} channel and its parity partner 1^{+-} channel. Best-fit parameters are given in table 3.7.

Fit	t_0	fit range	SVD cut	χ^2_ν	Q
2x2 fit	7	6-24	1.2×10^{-6}	0.88	0.72
2x2 hybrid fit	1	1-6	2.5×10^{-4}	0.9	0.58
4x4 fit	3	2-6	2.2×10^{-4}	0.81	0.82

Table 3.7: Summary of 1^{--} fit parameters on the f-5 ensemble. There are three fits, the standard vector 2x2 fit, the hybrid 2x2 fit, and the full fit with all 16 correlators.

We use Lepage's python library `corrfitter`, which implements a

suite of functions to fit correlators and matrices of correlators within a Bayesian framework [86, 89].

3.5 Results

In this section we present the results for the masses of the ground oscillating and non-oscillating states, describe our procedure for extrapolating to the continuum, and present results for the masses in the continuum. We don't apply any corrections, such as taste or finite-volume corrections, to our results before extrapolating. Omitting such corrections should not have a significant effect on our results as we expect both effects to be small at the charm quark mass, see for instance the negligible FV effects reported in [138] and the small taste splittings reported in [139]. Taste-splittings are discretisation errors which vanish in the continuum limit, so in any case the continuum extrapolated value with taste corrections should be consistent with the corresponding extrapolated value without taste corrections.

3.5.1 1^{-+} hybrid

Results, in lattice and physical units, for the ground state masses of the 1^{-+} hybrid correlators are collected in table 3.8. The conversion from lattice to physical units is done using values of w_0 and w_0/a determined on the ensembles by HPQCD in previous calculations [79, 91]. The non-oscillating ground state masses vary from 4.1–4.7 GeV across our ensembles with uncertainties between 1 and 2%. The oscillating ground state masses vary from 3.2–3.9 GeV with uncertainties between

Ensemble	aM_{NO}	M_{NO} (GeV)	aM_{O}	M_{O} (GeV)	$M_{\mathrm{NO}}/M_{\mathrm{O}}$
vc	3.144(62)	4.095(84)	2.80(13)	3.65(17)	1.123(60)
c	2.811(41)	4.577(71)	2.37(20)	3.87(32)	1.18(10)
c-10	2.858(27)	4.613(50)	2.44(19)	3.94(31)	1.169(91)
f	2.100(13)	4.716(39)	1.433(79)	3.22(18)	1.466(81)
f-5	2.144(23)	4.688(57)	1.624(98)	3.55(22)	1.320(78)

Table 3.8: Summary of 1^{-+} fit results. The second and fourth columns list the ground non-oscillating (NO) and oscillating (O) energies respectively in lattice units. The third and fifth columns list the corresponding masses in physical units. In the final column we list the ratios of the masses of the NO to O ground states on each ensemble.

5 and 10%. These larger uncertainties are unsurprising as oscillating states are harder to isolate, particularly so given the restricted fitting ranges. Comparing the results on the physical and unphysical ensembles there does not appear to be much variation in the masses by the value of m_l/m_s in the sea. The c/c-10 results are within 0.7σ and the f/f-5 results are within 1.2σ, with the unphysically heavy ensembles yielding slightly larger masses in both instances.

In figure 3.11 we show the overlaps of the hybrid operators with the hybrid states. The overlaps are related simply to the fitted coefficients, $\langle 0|\widehat{\mathcal{O}}|H\rangle = \sqrt{2M_H A_H}$. All the 1^{-+} overlaps agree to within 2σ. It is notable that the overlaps on the fine ensembles are much more precise than the coarse overlaps, which in turn are more precise than the very coarse overlap.

If we look at the ratio of the NO:O masses we see a clear increase, above 1, as the lattice spacing decreases, see figure 3.12. This enhanced separation of the oscillating and non-oscillating masses, and the smaller uncertainties of the overlaps on the fine ensembles in figure 3.11 may suggest that identifying and obtaining information about

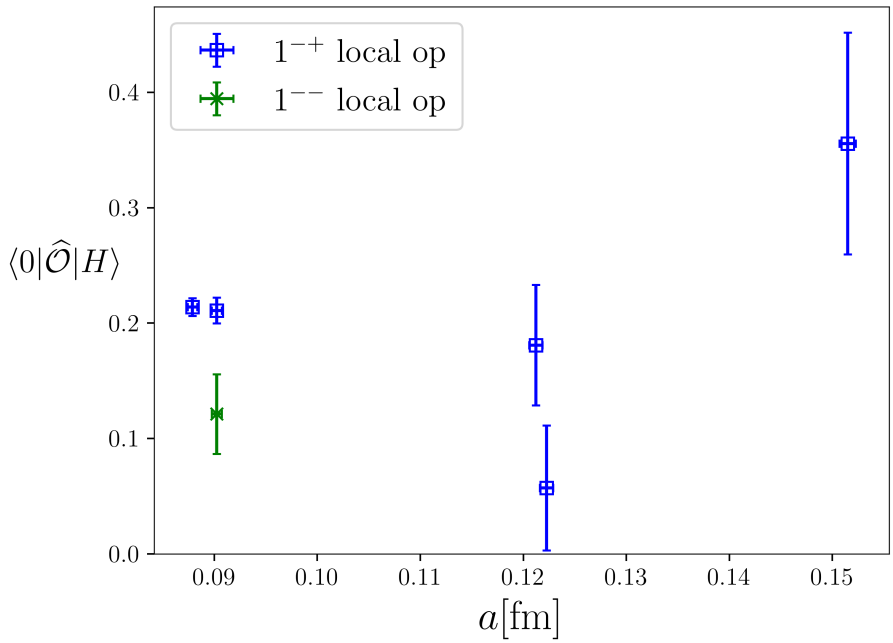

Figure 3.11: Overlap of the 1^{-+} and 1^{--}_H operators with the states identified as hybrids on all the ensembles.

hybrids with staggered fermions is easier at smaller lattice spacings.

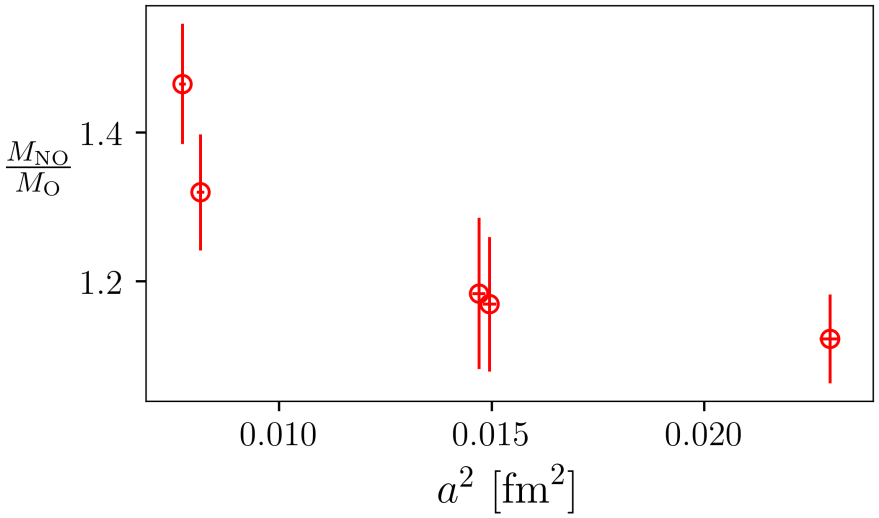

Figure 3.12: Ratio of the non-oscillating to oscillating masses against squared lattice spacing.

To extrapolate our masses to the continuum, $a = 0$, we use the following fit form,

$$M = c_0(1 + c_1(a\Lambda)^2 + c_2(a\Lambda)^4 + c_3\delta x) \tag{3.8}$$

where the c_i are the coefficients to be fitted. Both the NO and O masses are fitted simultaneously with the same priors. This form was chosen as it is the simplest functional form that can fit the data well while including a term to account for the unphysical ensembles. Attempts to fit to a function linear in a^2 (ie. set $c_2 = 0$) resulted in poor χ^2_ν. $\Lambda = 1$ GeV sets the scale of the extrapolation and the size of the priors on c_1, c_2. The $c_3 \delta x$ term is included to handle the presence of the unphysical ensembles, $\delta x \equiv (m_l^{\text{phys}} - m_l^{\text{sea}})/m_s$. We set a wide prior of 4(2) GeV on c_0 and 0(1) on the other coefficients. The goodness-of-fit parameters $\chi^2_\nu = 0.47$ and $Q = 0.91$. The extrapolation is shown in figure 3.13. Priors and best-fit parameters for the c_i are listed in table 3.9.

	prior	NO posterior	O posterior
c_0	4(2)	4.53(15)	3.04(35)
c_1	0(1)	0.39(22)	0.49(61)
c_2	0(1)	-0.93(33)	-0.21(73)
c_3	0(1)	-0.0004(14)	0.011(10)

Table 3.9: Priors and fit results from the continuum extrapolation of the 1^{-+} fitted masses on all the ensembles.

Setting $a = \delta x = 0$ implies that the continuum masses are equal to c_0. Therefore the continuum NO mass is 4.53(15) GeV, and we identify this as the mass of the 1^{-+} hybrid charmonium meson. This value will be compared to other determinations of the hybrid mass in the conclusions below. The continuum limit of the parity partner mass is 3.04(35) GeV, which given its 1^{++} quantum numbers we identify with the $\chi_c(1P)$, which has a mass of 3.51 GeV [16]. This mass is higher than our continuum determination, with a tension of around

1.5σ.

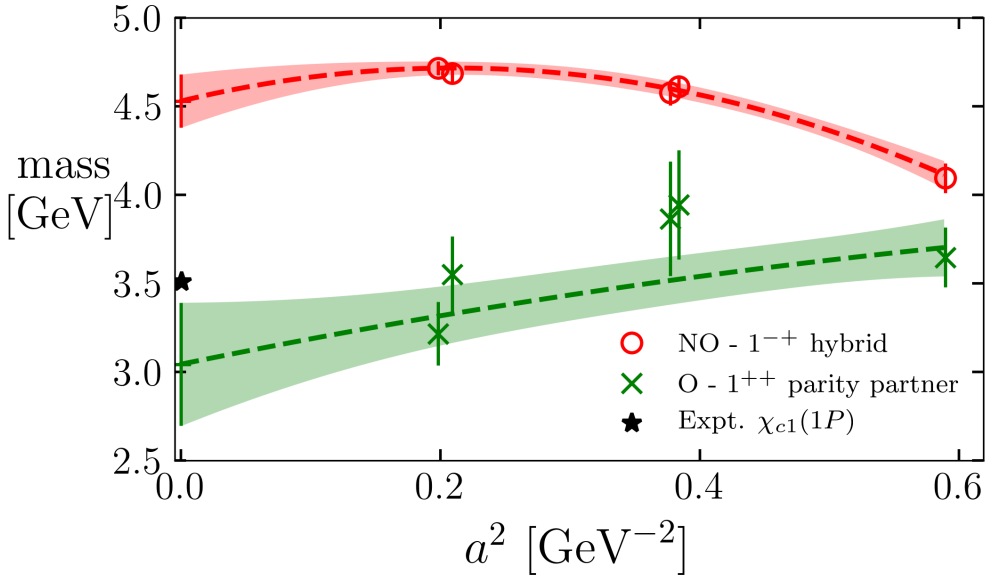

Figure 3.13: Continuum extrapolation of the masses of the 1^{-+} hybrid charmonium meson and its parity partner state.

In table 3.10 we break down the total uncertainty of the extrapolated masses into their component parts coming from different parts of the analysis.

The uncertainty comes mainly from the the fits of the correlator in the case of the hybrid, and equally from the correlator fits and extrapolation for the PP state. The determination of the lattice spacing, through w_0, contributes a small amount to the final error of both masses. Of note is the negligible contribution of the SVD cuts. By manually changing the SVD cuts we see that we need to make the cuts at least two orders of magnitude larger before they make a significant impact on the error. The insensitivity of our fits to SVD noise indicates we have not been unreasonable with our chosen SVD cuts.

	NO					O				
	vc	c	c-10	f	f-5	vc	c	c-10	f	f-5
statistics	1.43	0.82	0.71	0.59	0.93	4.23	2.63	2.18	5.36	5.61
prior	1.36	1.19	0.63	0.23	0.55	1.79	7.35	8.07	1.33	2.26
SVD cut	0.0	0.0	0.0	0.0	0.0	0.0	0.0	0.0	0.0	0.0
fit	3.03					7.67				
a	0.56					0.54				
$a \to 0$	1.25					8.45				
total	3.32					11.43				

Table 3.10: Percentage error budget for the oscillating and non-oscillating ground state masses of the 1^{-+} correlators and their continuum extrapolation. The error of the masses on each ensemble is given in the first three rows, broken down into their statistical, prior, and SVD cut contributions. These feed into the total error from the fit, given in the fourth row. The lattice spacing contribution to the error is given in the fifth row and the error from the extrapolation is given in the sixth row.

3.5.2 1^{--} hybrid

There are many XYZ states in the 1^{--} channel in the charmonium meson sector [16]. There are at least two conventional states, the ground state J/ψ around 3 GeV and the first excited state $\psi(2S)$ around 3.7 GeV. Therefore we expect the hybrid state to be the (at least) second excited state, after the J/ψ and $\psi(2S)$, with a mass around 4 GeV or more. When we examine the overlap of the hybrid operator with the states we find the second excited state has the first non zero overlap. The extraction of the properties of such a state will be more difficult than in the 1^{-+} case above where the hybrid was the ground state. Identification of the states, conventional charmonia or hybrid, is done by examining the overlaps. The amplitude listed is the overlap of the state with the unsmeared operator. The oscillating component of the correlator will contain 1^{+-} parity partner states,

implying the $h_c(1P)$ meson is the parity partner ground state. Our results are shown in table 3.11 where they are broken down into the three different fits described earlier. This is an exploratory calculation, using only correlators measured on the f-5 ensemble, which forecloses the possibility of a continuum extrapolation.

The ground state masses from the 2x2 vector fit agree well with the experimentally measured masses of the J/ψ and $h_c(1P)$ mesons, $M^{\text{exp}}_{J/\psi}$=3.096 GeV and $M^{\text{exp}}_{h_c(1P)}$=3.525, however the $\psi(2S)$ mass is larger than observed by 3.4σ, $M^{\text{exp}}_{\psi(2S)}$=3.686 GeV [16]. The 4x4 and 2x2 J/ψ masses are consistent (we could not identify a $\psi(2S)$ candidate state in the 4x4 fit), though there is a slight tension between their ground state amplitudes. In the full 4x4 fit the first state with significant non zero overlap with the hybrid operators has a mass of 4.38(12) GeV, this agrees with 4.33(16) GeV determined from the 2x2 hybrid fit.

state	M [GeV]	amplitude	f [MeV]	Γ_{ee} [keV]
	2x2 fit $\{J, j\}$			
J/ψ	3.097(17)	0.16441(26)	417.5(2.3)	5.836(36)
$\psi(2S)$	3.781(28)	0.1860(78)	428(18)	5.01(42)
$h_c(1P)$	3.512(29)	0.0578(75)	–	–
	2x2 fit $\{H, h\}$			
Hybrid	4.33(16)	0.086(15)	–	–
	4x4 fit $\{J, H, j, h\}$			
J/ψ	3.110(18)	0.1701(27)	431.1(7.2)	6.20(20)
Hybrid	4.38(12)	0.065(18)	9(167)	0.002(67)

Table 3.11: Summary of 1^{--} results for each fit on the f-5 ensemble, see table 3.7.

The J/ψ decay constant, $f_{J/\psi}$, is defined from

$$\langle 0|\bar{\psi}\gamma_\mu\psi|J/\psi\rangle = f_{J/\psi}M_{J/\psi}\epsilon_\mu, \tag{3.9}$$

and can be calculated from the amplitude, a_0, and mass, M_0, of the ground state,

$$f_{J/\psi} = Z_V a_0 \sqrt{\frac{2}{M_0}}, \tag{3.10}$$

where Z_V is the vector current renormalisation factor. The local vector operator was used so we need to renormalise it, we take the Z_V renormalisation factors from [50]. As a check we computed the decay constants of the J/ψ (see [63] for a systematic study of the leptonic decay constants of the J/ψ) and $\psi(2S)$, finding from the 2x2 fit $f_{J/\psi} = 417.5(2.3)$ MeV, in good agreement with the experimental value, $f^{\text{exp}}_{J/\psi} = 416(6)$ MeV, and $f_{\psi(2S)} = 428(18)$ MeV, significantly larger than the experimental value, $f^{\text{exp}}_{\psi(2S)} = 304(4)$ MeV [140]. We can define a hybrid decay constant, f_H, through the matrix element formed by the overlap of the vector current operator into the vector hybrid state,

$$\langle 0|\hat{\mathcal{V}}_i|H\rangle = f_H M_H \epsilon_i \ , \tag{3.11}$$

where $\hat{\mathcal{V}}$ is the vector current operator. Using f_H we can estimate the leptonic width, $\Gamma(H_{c\bar{c}} \hookrightarrow e^+e^-)$, of the hybrid vector charmonium state with the formula

$$\Gamma(H_{c\bar{c}} \hookrightarrow e^+e^-) = \frac{16\pi}{27}\alpha^2_{\text{QED}}\frac{f_H^2}{M_H} \ , \tag{3.12}$$

where $\alpha_{\text{QED}} = 1/134$ is the electromagnetic coupling at the charm quark mass. The overlap of the vector operator with the hybrid state is very small and consistent with zero, producing an implied upper bound on its leptonic width of just 70 eV. A previous calculation of

this leptonic width in the quenched approximation bounded it from above at 40 eV [141].

3.6 Conclusions

We have presented the first continuum extrapolation of the mass of the 1^{-+} charmonium hybrid meson in unquenched lattice QCD. Our continuum extrapolated hybrid meson mass is 4.53(15) GeV. In figure 3.14 we plot our results on each ensemble along with the continuum extrapolated value. Included in figure 3.14 are results for the mass from other lattice calculations [102, 142, 100]. These earlier calculations, in contrast to our staggered simulation, all used Wilson fermions with the clover action, heavier-than-physical pions, and did not do a continuum extrapolation.

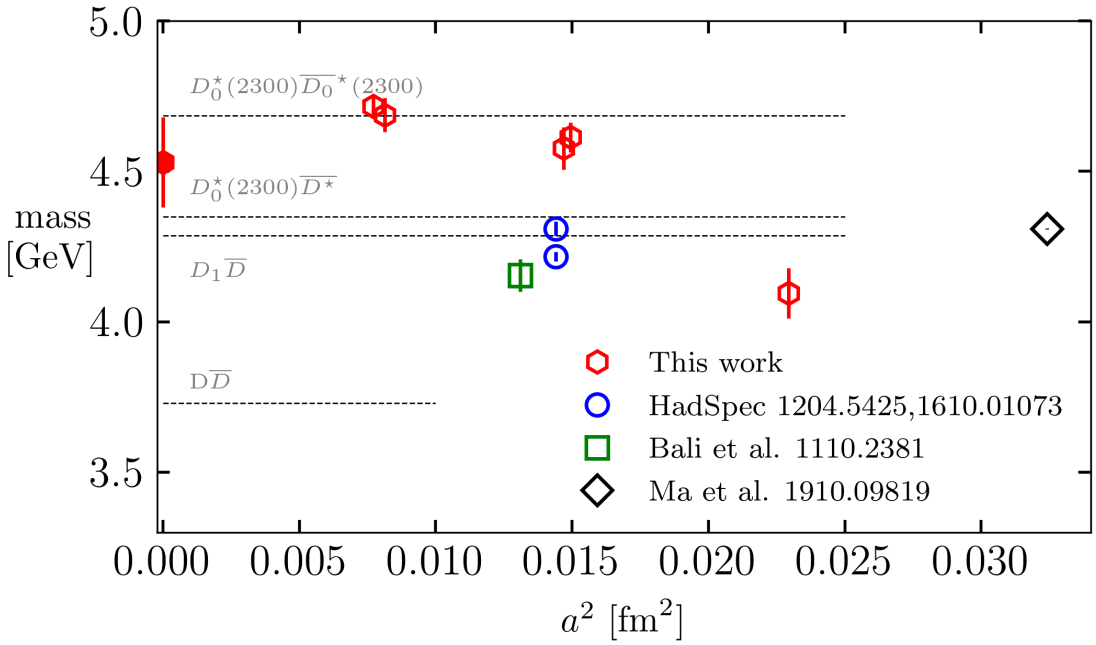

Figure 3.14: Summary plot for the 1^{-+} hybrid meson mass as a function of the lattice spacing, including some of the previous determinations of the mass by other groups [102, 142, 100].

We expect different discretisation effects from the clover action compared to the HISQ action we use, this may explain why our masses are a few hundred MeV higher than the Hadspec and Bali measurements around 0.12 fm. The clover simulations found the 1^{-+} hybrid mass increasing as the pion mass is decreased, from 1000 MeV in [142] to 400 MeV in [112] and 240 Mev in [102]. We do not see such a difference in our results, where the hybrid masses are consistent within errors on the physical and unphysical ensembles. It is interesting to note that our result agrees with the quenched continuum extrapolated results for the 1^{-+} mass in [109] and [143], suggesting the effect of quenching the sea quarks on the mass of the hybrid is not large.

There are several ways in which our analysis could be improved and extended. The non-linear variation of the mass with a^2, see figure 3.13, weighs heavily in favour of taking measurements on finer ensembles, to check the extrapolation and have better control of it. Results at 0.06 fm would improve the quality of the continuum extrapolation without incurring a large computational cost as such HISQ lattices already exist.

Having focused on the charmonium spectrum a natural extension would be to search for hybrids in the bottomonium spectrum where there are also many unidentified XYZ states (though as with charmonium, none have been seen in the 1^{-+} channel). In this case one would have to measure the mass of the 1^{-+} hybrid meson with a series of heavy quarks ($m_c < m_q < m_b$) before extrapolating to the bottom quark mass.

Enlarging the operator basis would improve our ability to isolate

and identify states in the correlator. In this project we focused on single meson operators with a small two operator basis, a more complete analysis would include two-meson operators in the operator basis. One could also include other four-quark operators, and/or the one-link hybrid operators in equation 3.4. This method, choosing a wide variety of shapes of operators in the 1^{-+} channel, is similar to that carried out by the HadSpec collaboration. Along similar lines the mixing of hybrid and tetraquark states on the lattice seems an interesting topic to investigate, particularly given the observed partial suppression of such mixing in the quenched approximation [143].

Throughout this work we have treated hybrid mesons as stable particles that do not decay. In reality they would be resonances that decay into lighter particles. Figure 3.14 includes some of the relevant physical decay thresholds in the charmonium sector, the lowest of which is the $D\overline{D}$ at around 3.8 GeV. Clearly the hybrid charmonium masses are distributed quite close to these thresholds. The $\chi_{c1}(3872)$ has often been identified as a $D\overline{D}^*$ molecular state due to its proximity to that threshold. Ultimately we would like to study the hadronic decays of the hybrid mesons on the lattice using Luscher's finite volume method [144, 145]. Hadspec have found that an operator basis that includes only single meson operators, like that used in this work, are not able to capture the whole finite volume spectrum [146]. They found that augmenting the operator basis with meson-meson like operators, like $[\bar{d}\gamma c][\bar{c}\gamma u]$, improved the spectrum. A calculation with a large basis consisting of meson like, meson-meson like, and tetraquark operators may be a promising avenue to explore. There are only a couple ex-

ploratory calculations of hadronic decays of hybrids using staggered fermions [147, 148], and a more advanced Hadspec calculation with Clover fermions [149].

We also showed results for the mass and leptonic decay constant of the 1^{--} charmonium hybrid meson at a single lattice spacing, 0.09 fm, with 310 MeV pions. The result for the hybrid mass is 4.38(12) GeV and its leptonic width is bounded from above at 70 eV. Brambilla et al. [96] review the importance of the decay constant in probing the properties of 1^{--} hybrid mesons. The mass is shown in figure 3.15 along with a selection of other results for the hybrid meson mass and three of the XYZ states in the 1^{--} channel. With the size of our

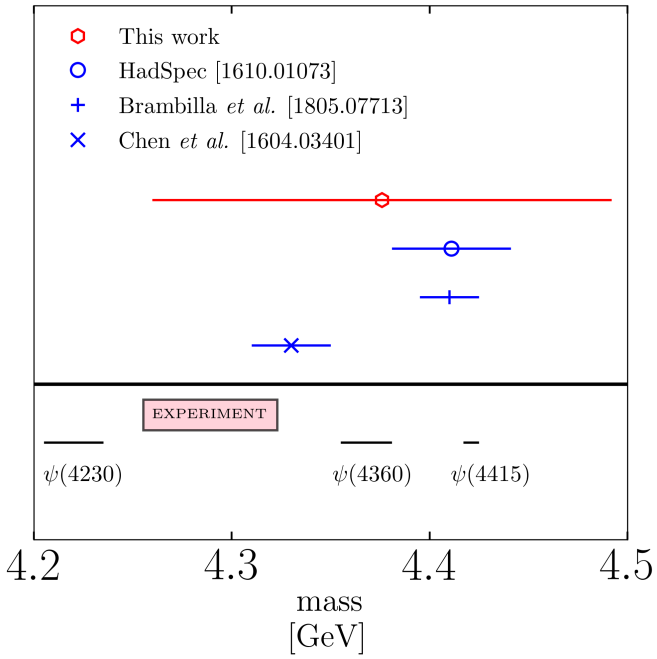

Figure 3.15: Comparison of our determination of the 1^{--} hybrid mass at 0.09 fm from a 4-by-4 fit to the results of three other groups, and three resonances the PDG lists as 'established'[102, 96, 141].

uncertainty and lack of a continuum extrapolation it is not possible to identify the 4.38(12) GeV state with any of the experimental resonances. The 1^{--} channel is so densely populated that a larger operator

basis and far greater statistical precision is essential to separate out the conventional states from the unconventional states.

Our results (see the error budget in table 3.10) make clear how noisy correlators formed from operators including the field strength tensor can be. It is clear that if significant progress is to be made in determining the properties of hybrid mesons, this signal to noise problem must be overcome. This is what motivated us to use smearing and a GEVP approach in the first place. Alternatives to the point source operator like the stochastic wall source should be investigated. Recently the multi-level Monte-Carlo integration approach has been used to reduce the noise in the tail of the vector correlator with impressive results, applying it to hybrid correlators may be worth exploring [150].

Chapter 4

The QED correction to the Hadronic Vacuum Polarisation

4.1 Introduction

The muon is a second generation lepton with the same electric charge and around 200 times the mass of the electron. As it has an intrinsic spin it responds to magnetic fields by aligning its axis along the field lines. The size of the magnetic moment associated to its spin is $\propto e\hbar/2m_\mu$, with constant of proportionality g_μ. Dirac's quantum theory of the electron predicted that this constant of proportionality is equal to 2 [52]. Schwinger realised quantum fluctuations would 'correct' this value and made the first calculation of the $\mathcal{O}(\alpha)$ correction to g_μ[1] using his then new formulation of QED [56]. In particular Schwinger

[1] the $\mathcal{O}(\alpha)$ correction is independent of lepton mass and therefore the same for g_e.

calculated the quantum correction to the magnetic moment from a virtual photon, see figure 4.1.

In fact g_μ gets corrections not only from QED but also the Electroweak and Strong sectors of the SM. An example of a relevant diagram in the Electroweak sector is shown in figure 4.1, where a virtual Z boson is exchanged.

The fractional difference of g_μ from the naive value of 2 is called the 'anomalous magnetic moment of the muon', $a_\mu \equiv (g_\mu - 2)/2$. For more than two decades now there has been a tension in the theory and experimental values for the muon anomaly. Although not significant enough (in the statistical sense) to be classed as a discovery, the longevity of the discrepancy has led some to focus their search for new beyond-the-Standard Model (BSM) physics on this observable.

Quantum corrections to $(g-2)_{\text{lepton}}$ from new heavy particles from BSM are expected to be $\propto (M_{\text{lepton}}/M_{\text{heavy}})^2$, meaning such effects should be easier to discern with g_μ than g_e. Of course the tau lepton is heavier still but it decays weakly before it can hadronise.

This chapter will focus on the theory side of the calculation and, in particular, the QED correction to the hadronic vacuum polarisation contribution to the anomaly.

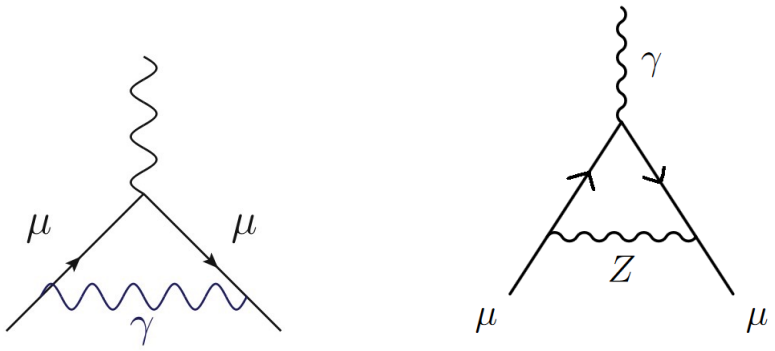

Figure 4.1: (left) The quantum correction to the magnetic moment of the muon coming from a virtual photon. (right) Same but for a Z boson.

The various contributions to a_μ are listed in table 4.1. They are broken down into QED, Electroweak, and Strong contributions, with the Strong contribution further broken down into the hadronic vacuum polarisation (HVP) and hadronic light-by-light (HLbL) contributions. Even though the QED contribution dwarfs the other contributions its very precise determination means it contributes a tiny amount to the theoretical uncertainty of a_μ, just 0.1×10^{-11} compared with the overall uncertainty of 40×10^{-11}. The HVP contribution to a_μ is, albeit several orders of magnitude smaller than the QED contribution, the next largest piece with a much larger contribution to the total uncertainty of 40×10^{-11}. It is necessary to control the HVP contribution to a greater precision to reduce the theoretical uncertainty of a_μ.

Contribution	Value $\times 10^{11}$	Ref
QED	116 584 718.931(104)	[151]
Electroweak	153.6(1.0)	[151]
Strong - HVP (data-driven)	6845(40)	[151]
Strong - HVP (Lattice)	7116(184)	[151]
Strong - HLbL	106.8(14.7)	[152]
SM value	116 591 817(43)	[151]
Exp value	116 592 061(41)	[153]
Exp-Th difference	244(59)	[151]

Table 4.1: The various SM contributions to a_μ . Table adapted from [151], see references therein.

4.1.1 a_μ from experiment

The E821 experiment at the Brookhaven National Laboratory (BNL) in New York made precision measurements of the anomaly, a_μ, by injecting polarised muons into a magnetic storage ring and measuring the difference, ω_a, between its precession and cyclotron frequencies [154, 155]. In a similar manner to a spinning top the magnetic moment of the muon precesses about its axis in the presence of a magnetic field which is perpendicular to the muon spin direction and to the plane of its orbit. The muons decay into positrons whose energy spectra are measured and depend simply on ω_a. Since $\omega_a = a_\mu \frac{eB}{mc}$, this is a way to measure the anomaly, provided the magnetic field can be mapped and measured precisely. This is done by placing hundreds of NMR probes around the vacuum chamber the muons travel through.

While simple in theory several corrections are needed to take into account systematic effects encountered in the real world, here we just mention two of these corrections. A so-called pitch correction is required to account for vertical betatron oscillations that cause the muon spin and magnetic field not to be perpendicular. To keep the muons vertically confined an electric quadrupole is used to generate an electric field. This electric field can also cause the muons to precess, and this effect also has to be corrected for. For more details on the corrections and experimental setup see [154, 155]. The E821 result of

$$a_\mu^{(\mathrm{BNL})} = 116\,592\,089(63) \times 10^{-11} \ , \tag{4.1}$$

was in tension with the SM value at the level of 2.6σ [155]. This tension warranted a follow-up experiment.

The E989 experiment at the Fermilab National Accelerator Laboratory (FNAL) is a direct successor to E821 and uses the same principles to measure a_μ [153]. It uses the same storage ring as the E821 experiment, which had to be transported from New York to Illinois via the Mississippi river as some of its components could not be broken up. By using 20 times as many muons as the E821 experiment they are able to improve the lower bound on the achievable statistical error. The E989 experiment has 2.5 times improved magnetic field uniformity and much improved magnetic field measuring capabilities. Its state-of-the-art tracking and improved calorimetry enable it to measure the beam properties and precession frequency more precisely. Detailed beam storage simulations were used to determine the

uncertainties in the pitch and electric field corrections arising from the particular geometry of the setup.

The overlapping apparatus between the two experiments prompted some to question whether their results are truly independent. The Fermilab group performed a multitude of cross-checks and calibrations to establish this independence [153, 156]. Their analysis was also blinded, meaning they did not know the final result until after they had completed their analysis, at which point they could not make any further changes and unblinded their result. This was done to remove the possible influence of confirmation bias. The E989 result,

$$a_\mu^{(\mathrm{FNAL})} = 116\,592\,040(54) \times 10^{-11} \ , \tag{4.2}$$

has a precision of 0.46 ppm or just under one part in two million [153]. This result is 3.3σ larger than the SM result and agrees very well with the previous measurement by E821. E989 will collect more data over the coming years and is aiming for a final uncertainty of around 0.1 ppm. Combining the two results lowers the uncertainty of a_μ to 0.35 ppm, and increases the experiment-theory deviation to 4.2σ, not far off the 5σ threshold at which a discovery can be claimed. Figure 4.2 summarises this information.

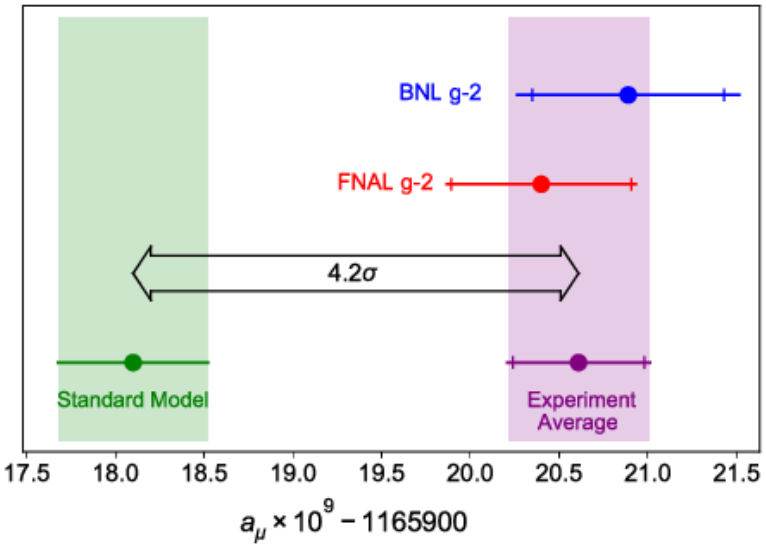

Figure 4.2: Figure taken from [153] showing the difference, 4.2σ, between the average of the Fermilab and Brookhaven measurements, and the SM prediction from the data driven dispersive approach.

The planned experiment at J-PARC by the E34 collaboration will provide another independent measurement of the muon anomaly [157]. By using an ultra-cold muon beam they remove the need for an electric focusing field. After accelerating the muons in a linac to 300 MeV/c they are injected into a storage ring around 20 times smaller than the one used in the BNL and FNAL experiments. They aim for a precision of 0.1 ppm in their measurement of the muon anomaly, similar to the ultimate goal of the E989 experiment.

4.1.2 Hadronic Vacuum Polarisation contribution

There are two complementary methods for determining the HVP contribution to a_μ, the data-driven dispersive approach and the lattice approach. As the data-driven approach currently yields a value with a smaller uncertainty (see table 4.1) it is used in the SM determination of a_μ.

The data-driven determination is obtained by converting loop integrals of the HVP inserted into the photon propagator, see figure 4.3, into dispersion integrals over the cross section of a virtual photon decaying into hadrons [158],

$$a_\mu^{\mathrm{HVP,LO}} = \frac{\alpha^2 m_\mu^2}{9\pi^2} \int_{m_\pi^2}^{\infty} ds \frac{\hat{K}(s)}{s^2} R(s). \tag{4.3}$$

$\hat{K}(s) = \frac{3s}{m_\mu^2} K(s)$, is a known slowly varying monotonic function that depends on the mass of the muon,

$$K(s) = \frac{x^2}{2}(2 - x^2) + \frac{(1+x^2)(1+x)^2}{x^2}\Big(\log(1+x) - x + \frac{x^2}{2}\Big) + \frac{1+x}{1-x}x^2 \log x$$
$$\text{where} \quad x = \frac{1-\beta_\mu}{1+\beta_\mu}, \quad \beta_\mu = \sqrt{1 - 4m_\mu^2/s}. \tag{4.4}$$

The hadronic R-ratio, $R(s)$, given by

$$R(s) = \frac{\sigma^0(e^+e^- \to \mathrm{hadrons}(\gamma))}{4\pi\alpha^2/3s}, \tag{4.5}$$

depends on the bare (excluding VP effects) cross-section for electroproduction. $R(s)$, and therefore $a_\mu^{\mathrm{HVP,LO}}$, is calculated by combining the experimental results for $e^+e^- \to \mathrm{hadrons}(\gamma)$ across a range of energies. The simplest way to do this, called the direct scan method, is by measuring the hadronic cross section while varying the beam energy of a e^+e^- collider. Multiple experiments and an abundance of data mean the hadronic cross section is known precisely across a wide range of energies [151].

The accepted data-driven SM prediction for the HVP contribution was put forward by the g–2 Theory Initiative in a white paper authored

by a large collection of physicists, and represents a best estimate value against which lattice results can be compared [151]. See table 4.1 for the value put forward by the Theory Initiative and figure 4.6 for results from individual groups. The 4.2σ deviation is between experiment and the SM value incorporating the data-driven HVP.

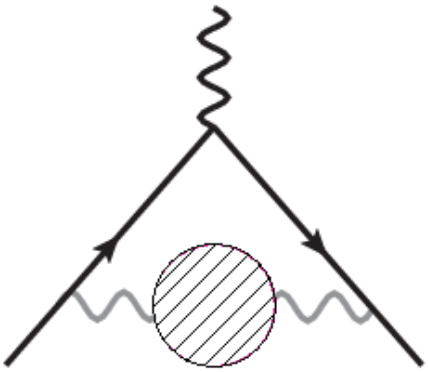

Figure 4.3: The Feynman diagram corresponding to the LO HVP contribution to the anomalous magnetic moment of the muon.

The LO HVP contribution can be calculated on the lattice by measuring vector current-current correlators [159, 160],

$$C(t) = \frac{1}{3}\sum_{i}\sum_{x}\langle j^i(x,t)j^i(0,0)\rangle, \tag{4.6}$$

where $j^i = \overline{\psi}\gamma_i\psi$ is the vector current. The correlators are then Fourier transformed to obtain the quark polarisation function, $\Pi(q^2)$,

$$q^2\Pi(q^2) = a^4\sum_{t} e^{iqt}\sum_{x}\langle j(x,t)j(0,0)\rangle, \tag{4.7}$$

which is integrated with a kinematic function to get a_μ^{HVP}. The contribution to a_μ^{HVP} coming from a quark of flavour f can then be thought of as coming from an insertion of the subtracted quark polarisation,

$\hat{\Pi}(q^2) = \Pi(q^2) - \Pi(0)$, into the photon propagator,

$$a_\mu^{(f)\mathrm{HVP,LO}} = 4\alpha^2 Q_f^2 \int_0^\infty dq^2 \mathcal{F}(q^2)\, \hat{\Pi}_f(q^2), \tag{4.8}$$

where Q_f is the electric charge of the quark of flavour f, and the QED kernel $\mathcal{F}(q^2)$ is a kinematic function [159],

$$\begin{aligned} \mathcal{F}(q^2) &= \frac{m_\mu^2 q^2 Z^3 (1 - q^2 Z)}{1 + m_\mu^2 q^2 Z^2} \\ Z &= -\frac{q^2 - (q^4 + 4m_\mu^2 q^2)^{1/2}}{2m_\mu^2 q^2}. \end{aligned} \tag{4.9}$$

There are different conventions for writing down equation 4.8, this form makes clear the LO HVP is $\mathcal{O}(\alpha^2)$. The $\mathcal{O}(\alpha)$ Schwinger contribution is simply the photon propagator without the insertion of the quark polarisation, $\frac{\alpha}{\pi}\int_0^\infty dq^2\, \mathcal{F}(q^2)$.

$\mathcal{F}(q^2)$ diverges as $q^2 \to 0$, with the integral in equation 4.8 dominated by the low momentum region around $q^2 = m_\mu^2$. This divergence does not cause the integral to blow up as it is cancelled by the vanishing of the subtracted quark polarisation function, see figure 4.4. $\mathcal{F}(q^2)$ tends to 0 as q^2 increases while $\hat{\Pi}(q^2)$ grows larger. The overall effect is that the integrand in equation 4.8 dies off at both large and small q^2, see figure 4.5. The HVP is nonperturbative in the low q^2 region so that the lattice is an appropriate calculational tool. Above $q \sim 1/a$ $\hat{\Pi}(q^2)$ is cutoff on the lattice, the small (on the order of a percent) contribution to the HVP in this region can be calculated with continuum perturbation theory [161].

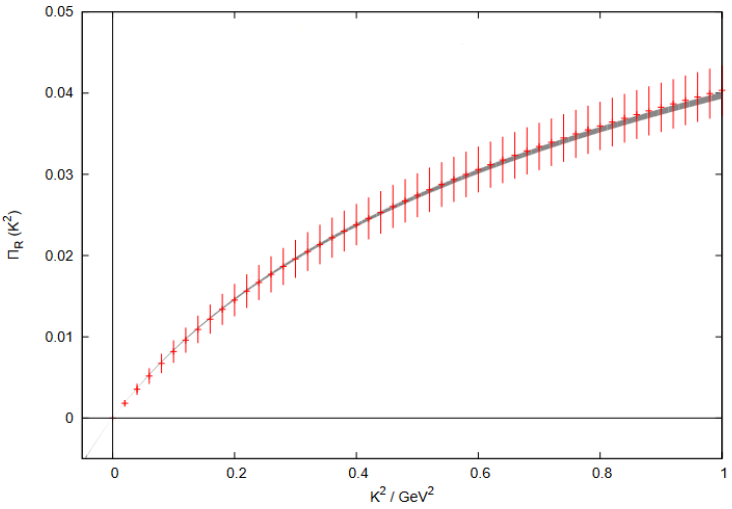

Figure 4.4: The subtracted quark polarisation function, $\Pi_{\mathrm{R}}(K^2)$, from experiment (grey band) and a typical lattice (red lines) [162].

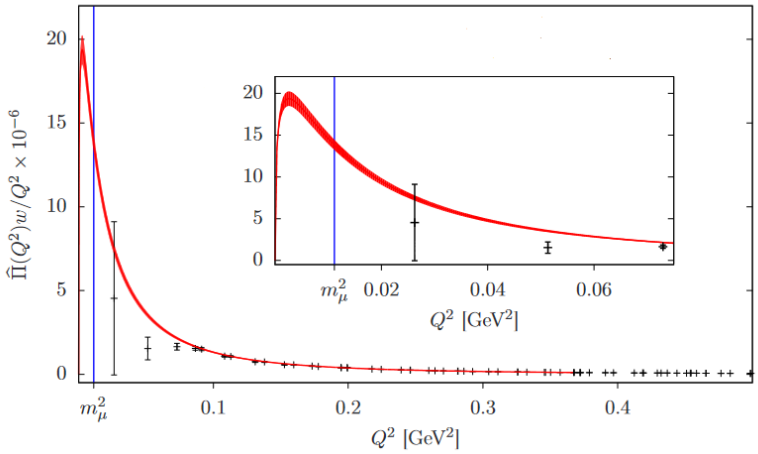

Figure 4.5: The integrand in equation 4.8 with $w/Q^2 \equiv \mathcal{F}(Q^2)$ [163].

In the time-momentum representation [164] the subtracted quark polarisation can be obtained by integrating the correlator over time with a kernel,

$$\hat{\Pi}(\omega^2) \equiv \frac{4\pi^2}{\omega^2} \int_0^\infty dt \left[\omega^2 t^2 - 4\sin^2\left(\frac{\omega t}{2}\right)\right] C(t). \tag{4.10}$$

On a periodic lattice this integral becomes a sum,

$$\hat{\Pi}(q^2) \equiv \Pi(q^2) - \Pi(0) = \sum_t \left(\frac{\cos(qt) - 1}{q^2} + \frac{1}{2}t^2 \right) C(t). \tag{4.11}$$

Then equation 4.8 can be recast as a weighted sum over time of the correlator with weights, w_t, that can be calculated using equation 4.11,

$$\begin{aligned} a_\mu^{\mathrm{HVP,LO}} &= \sum_t w_t C(t) \\ \implies w_t &= 4\alpha^2 \int_0^\infty dq^2 \mathcal{F}(q^2) \left(\frac{\cos(qt) - 1}{q^2} + \frac{1}{2}t^2 \right) . \end{aligned} \tag{4.12}$$

On the lattice the LO HVP contribution has been calculated previously by many groups, for recent examples see [165, 166, 77, 167]. This project is part of the HPQCD, MILC, and Fermilab Lattice collaborations joint effort at calculating the HVP over the last several years [138, 168, 169, 91].

The two methods should agree on the value of the HVP. In figure 4.6 a selection of the dispersive and lattice HVP results are highlighted, showing that the two methods agree with each other, if only because the uncertainty of the lattice results are relatively large. Results on the lattice are expected to continue improving and should match the precision of the dispersive method in the future. The current state-of-the-art lattice result, from the BMW collaboration, is around 2σ larger than the dispersive result, and 2σ lower than the experimental result (assuming no new physics) [77]. The evidence for a discrepancy between the dispersive and lattice HVP has been bolstered recently by a series of papers looking at windowed values of $a_\mu^{\mathrm{HVP,LO}}$ [170, 171, 172].

Windowed quantities are determined by restricting the sum in equation 4.12. By cutting out large times and/or short times from the correlator the windowed lattice HVP has lower statistical and systematic errors, and a more stringent comparison with the (windowed) dispersive HVP can be made.

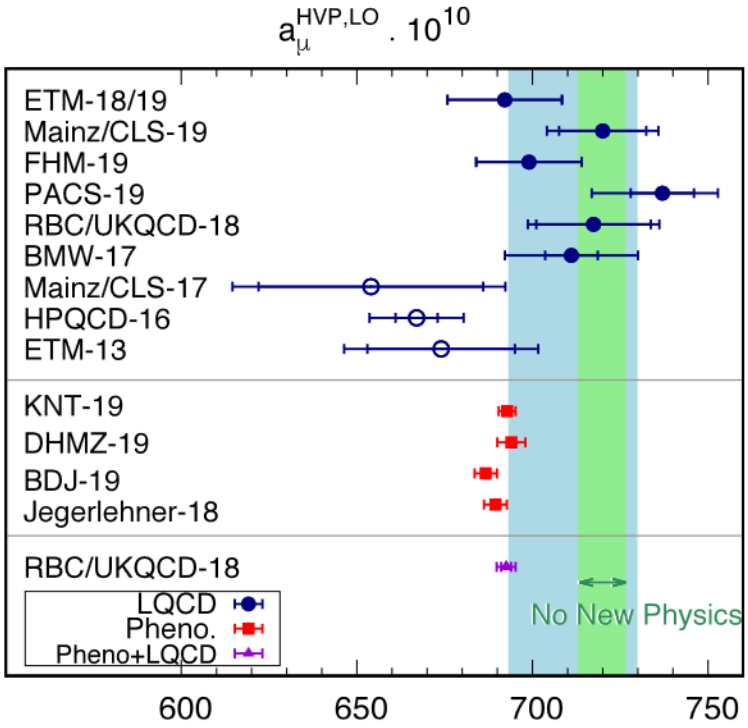

Figure 4.6: Figure taken from [151] showing various lattice and dispersive calculations of the HVP. The expected value of the HVP in the absence of any new physics is shown as a green band.

Next-to-leading (NLO) order HVP effects are further suppressed by a power of α and will not be considered here, the joint Fermilab Lattice, MILC, and HPQCD collaboration found the NLO HVP contribution to be around 1% of the LO effect as expected, similar in size to the HLbL contribution [173].

4.2 QED Correction to the HVP

Reducing the theoretical uncertainty of $a_\mu^{\mathrm{HVP,LO}}$, which we will now refer to as a_μ, below 1% requires the inclusion of isospin breaking effects. These arise from the up and down quarks unequal masses, $m_u \neq m_d$, and their unequal electric charges, $Q_u = 2e/3 \neq Q_d = -e/3$. This project aims to calculate the QED isospin breaking correction to the light connected HVP, see figure 4.7.

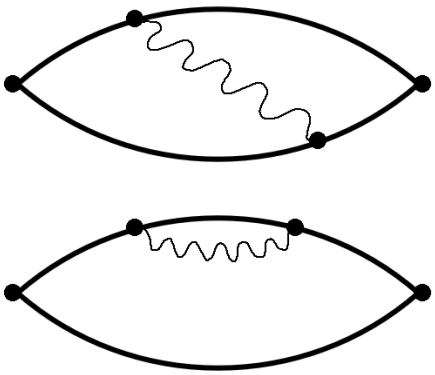

Figure 4.7: QED correction diagrams to the connected HVP at $\mathcal{O}(\alpha)$.

We use the following definition for the QED correction to the HVP, δa_μ^f,

$$\delta a_\mu^f \equiv a_\mu^f(m_q^f, Q_f) - a_\mu^f(m_q^f, 0), \tag{4.13}$$

where the difference is evaluated at equal renormalised quark mass. The QED correction to the connected strange HVP is then simply

$$\delta a_\mu^s = a_\mu^s(m_s, -1/3) - a_\mu^s(m_s, 0), \tag{4.14}$$

with corresponding formulas for the up and down quarks. The QED correction to the light connected HVP is the sum of the corrections

for the up and down quarks,

$$\delta a_\mu^{ll} = \delta a_\mu^u + \delta a_\mu^d. \tag{4.15}$$

Including QED in our simulations leads to two issues, potentially enhanced finite volume effects, and renormalisation effects, which we now discuss. For a short discussion on the formalisms for including QED on the lattice and a description of our process for generating quenched $U(1)$ fields see the relevant sections in chapters 1 and 2.

4.2.1 QED HVP Finite Volume Effects

Finite volume effects (FVE) are an issue for QED corrections to QCD quantities on the lattice. Whereas FVE on pure QCD quantities are exponentially suppressed on the lattice, going like $e^{-m_\pi L}$, in QED calculations FVE scale like $1/L^n$, where n varies depending on the observable being studied. From the physical point of view we can understand these larger power-like FVE as a manifestation of the long ranged nature of the electromagnetic interaction. The massless, electrically neutral photon can connect disparate regions of a box, size L, in a way colour confined gluons cannot.

Given the potentially large systematic errors these power-like corrections may impose on QCD+QED calculations many groups have studied the finite volume properties of many observables on the lattice, and with effective field theories confined to finite volumes. The FVE on the lattice can then be controlled using the parameterisations gained from an EFT. For example, in [174] the authors show the

FV electromagnetic correction to charged pseudoscalar meson masses is $\mathcal{O}(1/L^3)$. In [130] it was shown, with the HISQ action, that the quenched QED correction to both the J/Ψ and η_c masses did not vary with lattice size to within 0.01%. This was not unexpected as these mesons are spatially small, and the FV expansion for electrically neutral mesons begins at $\mathcal{O}(1/L^4)$.

The authors of [175] show, using a scalar QED model, that the $\mathcal{O}(\alpha)$ QED_L FV correction to the two pion contribution to the HVP is $\mathcal{O}(1/L^3)$. From the physical point of view this is due to the electrically neutral nature of the vector correlators, in a similar way to the strength of the electric field of a dipole. More specifically, they found the QED FVE on the quark polarisation function, $\Delta\Pi(q^2) \sim (m_\pi L)^{-3}$. In addition they showed that their result is universal in full QCD+QED. Plugging in $m_\pi L \sim 0.1 \times 3.2$, the values on our smallest lattice (and hence where FVE will be most severe), implies an effect of 3%. This is a much smaller systematic uncertainty than our current and forecast statistical uncertainty. Therefore, given the precision we are aiming for, we can safely neglect QED FVE.[2] These effects on the HVP are small overall and should not make up a significant fraction of the error budget of δa_μ in the short to medium term.

As a check we performed a brief FV study at m_s, where the predicted QED FVE are $\sim 0.02\%$. Within our statistical uncertainties we found no discernible effect. The ensembles we used and the results are described in table 4.4, and figure 4.19.

[2]This is fortunate, carrying out a FV study at lighter valence quark masses would require a large amount of time and resources.

4.2.2 EM Renormalisation and Scheme Dependence

We want to isolate the QED correction to the HVP and, accordingly, all our ensembles have $m_u = m_d = m_l$ (IsoQCD) and no strong isospin breaking contributions to a_μ are calculated. Matching the parameters of full QCD+QED onto the real world to produce physical results proceeds in much the same way as pure QCD, the only difference being an extra parameter to fix, the EM coupling α. An extra complication arises because we wish to separate out the QCD and QED contributions to a_μ. In writing a_μ like so,

$$a_\mu = \overline{a}_\mu + \delta a_\mu \tag{4.16}$$

where $\overline{a}_\mu$ is the QCD part, and δa_μ is the QED correction, we are making an unphysical separation. This leads to an inescapable ambiguity in the definition of δa_μ stemming from our choices in making that separation. Implicit in equation 4.16 is a choice of parameters for which $\delta m = m_u - m_d = 0$. Although in IsoQCD we simulate with $\delta m = 0$ when QED is turned on their masses will not renormalise in the same way because of their differing charges.

The charged and uncharged correlators we have computed are at the same bare quark mass. If we assume the QCD-only bare quark masses are tuned correctly then we only need to determine the bare quark masses m_u, m_d that, upon renormalisation with respect to QED, yield m_l. If the quark mass shift, δm_q, induced by turning on QED is small, the translation from differences at equal bare quark mass, Δa_μ,

to equal renormalised quark mass, δa_μ is straightforward,

$$\begin{aligned} \delta a_\mu &= a_\mu^{\mathrm{QCD+QED}}(m_q - \delta m_q) - a_\mu^{\mathrm{QCD}}(m_q) \\ &= \Delta a_\mu - \delta m_q \frac{\partial a_\mu}{\partial m_q}, \end{aligned} \tag{4.17}$$

where we determine $\frac{\partial a_\mu}{\partial m_q}$ on each ensemble by fitting a smooth spline through a_μ. After taking the chiral and continuum limits of Δa_μ, $\delta m_q = m_q \delta_q$, and $\partial a_\mu / \partial m_q$ we use equation 4.17 to calculate the extrapolated δa_μ. Alternatively we can correct the bare differences at each m_q before extrapolating in δa_μ.

We adopt the nonperturbative EM renormalisation procedure first introduced by BMW in [176], and also used by MILC in [177]. In the QCD+qQED theory we adjust the bare masses m_u, m_d to enforce

$$\begin{aligned} M^2_{uu'} = M^2_{dd'} = M^2_{nn'} \equiv M^2_{\pi^0} \\ (M^2_{uu'})^\gamma = 0 = (M^2_{dd'})^\gamma \end{aligned} \tag{4.18}$$

where $M^2_{xx'}$ is the squared mass of the ground state pseudoscalar meson correlator. 'u' here means up-like with respect to QED, 'd' down-like, and 'n' neutral. In effect we are setting $\delta m = 0$ through a proxy, $\Delta M^2 = M^2_{uu'} - M^2_{dd'}$. We perform our simulations in the Strong isospin-symmetric limit where, in QCD, $m_l = m_d = m_u$. After EM renormalisation we have $m_u = m_l(1 - \delta_u)$ and $m_d = m_l(1 - \delta_d)$ to enforce equation 4.18. δ_u and δ_d are the fractional shifts in the u and d bare masses needed to ensure the renormalised masses are both equal to m_l. All quarks with the same electric charge will renormalise the same with respect to QED, so that $\delta_s = \delta_d$.

It can be show that equation 4.18 can be written in terms of the differences at equal bare quark mass,

$$\begin{aligned} \Delta M^2_{uu'}(m_u) &= 2Bm_l\delta_u \\ \Delta M^2_{dd'}(m_d) &= 2Bm_l\delta_d, \end{aligned} \tag{4.19}$$

where B is a parameter that can be determined from NLO SU(2) χPT and the LEC $l_3 = 3.07(64)$ [178]. After a chiral extrapolation to find the quantities on the LHS of equation 4.19 we can solve for δ_u and δ_d at each lattice spacing. NNLO SrχPT suggests a chiral fit function of the form $Am_q + Bm_q^2$. Figure 4.8 illustrates these chiral fits on the fine and very coarse ensembles. See table 4.5 and the accompanying discussion for more information on the pseudoscalar fits. Note that because we have fewer statistics on the fine ensemble the extrapolated values of δ_d, δ_u are relatively wide and dominate the error in δa_μ.

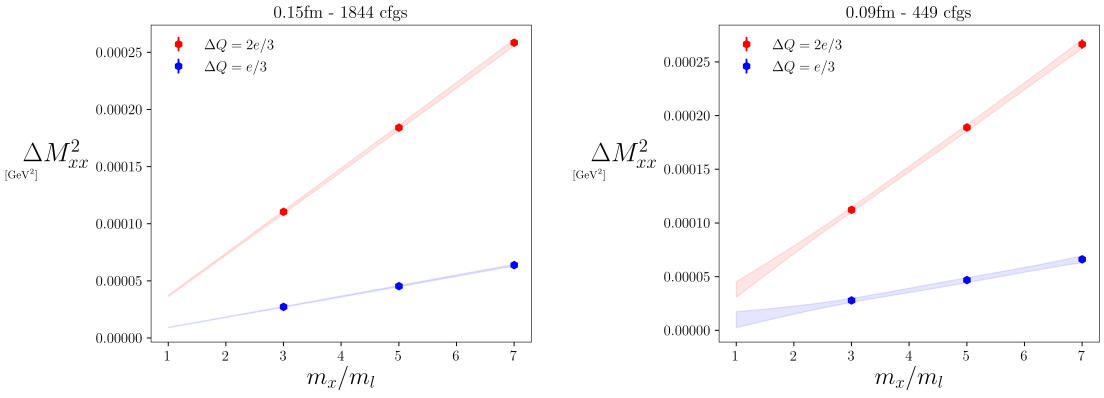

Figure 4.8: Shift in the squared pseudoscalar mass due to QED as a function of quark mass. By extrapolating to $m_q = m_l$ and using equations 4.19 we can calculate the fractional shift in the quark mass due to QED in our chosen renormalisation scheme.

δa_μ is scheme dependent, this fact must be kept in mind when comparing results for the QED correction to a_μ from different groups.

In contrast the total quantity, a_μ, is scheme independent and can be compared across different groups after extrapolating to infinite volume and zero lattice spacing.

An alternative renormalisation prescription called the GRS scheme (after its proposers) has been used by the ETM collaboration in the past [179, 180]. In the GRS scheme the quark masses and strong coupling have their values in QCD and QCD+QED matched at 2 GeV in the $\overline{\text{MS}}$ scheme.

The electromagnetic coupling, α, will also renormalise and this too could introduce scheme ambiguities. However these corrections, from the running of α, are $\mathcal{O}(\alpha^2)$ and so can be safely neglected.

4.3 Simulation details

We measured correlators on gauge field ensembles generated with the Highly Improved Staggered Quark (HISQ) action with 2+1+1 flavours of dynamical sea quarks and physical pion masses [38]. In order to take the continuum limit we took measurements on 3 ensembles with lattice spacings of 0.15, 0.12, and 0.09 fm. These HISQ ensembles were generated by the MILC collaboration with updated properties determined by the HPQCD collaboration [134, 181]. Their specifications are given in table 4.2. The lattice spacing is fixed from $w_0 = 0.1715(9)$ fm [79].

name	L^3xT	w_0/a	$M_\pi L$	M_π (MeV)	N_{cfg}
very coarse	32^3x48	1.13215(35)	3.30	134.73(71)	1844
coarse	48^3x64	1.41490(60)	3.88	132.73(70)	967
fine	64^3x96	1.95180(70)	3.66	128.34(68)	596

Table 4.2: Properties of the gauge field ensembles, made available to us by the MILC collaboration, used for our measurements [134]. The relative lattice spacings, w_0/a, and pion masses were determined in [181].

We measure pseudoscalar and vector meson correlators with equal mass, oppositely charged quarks and antiquarks, so that all the correlators are neutral overall.

To calculate the correlators we read an archived dynamical SU(3) gauge configuration and a quenched U(1) gauge configuration before multiplying the U(1) links fields into the SU(3) link fields, and gauge smearing as usual. The calculation then proceeds like an ordinary lattice QCD measurement, propagators are computed with specified source and sink operators and then tied into meson correlators.

We use stochastic wall sources projected onto the appropriate spin-taste quantum numbers. For the vector current we use the $\gamma_i \otimes \gamma_i$ operators, and for the pseudoscalar current we use the $\gamma_5 \otimes \gamma_5$ operator. These are both local operators, this is important in the case of the vector operator as it is non-conserved and requires renormalising with a renormalisation factor Z_V. The required Z_V, and their QED corrections, have been calculated by HPQCD [50, 130].

In order to avoid the increased statistical noise and greater resource demand incurred by simulating at the light quark mass, $m_l \equiv$

$1/2(m_u + m_d)$, we measure with valence quarks at multiples of m_l. We measure at $3/5/7m_l$ as well as the strange quark mass, m_s, on each ensemble. We use a multi-shift solver so that for each charge all the masses can be solved in a single iterative process. As it is not prohibitively expensive we also measure at the physical m_u and m_d on the very coarse ensemble. The correlators measured, including the quark masses and electric charges, are summarised in table 4.3.

name	Charges (e)	Quark masses (am_q)	sources
vc	±2/3,±1/3,0	0.001524, 0.003328, 0.007278, 0.01213, 0.01698, 0.0677	16
c	±2/3,±1/3,0	0.00552, 0.0092, 0.01288, 0.0527	16
f	±2/3,±1/3,0	0.0036, 0.006, 0.0084, 0.0364	16

Table 4.3: The valence quark masses and charges used to compute the pseudoscalar and vector meson correlators.

Effective mass plots are shown in figure 4.9. As we are using the staggered formalism we choose a definition of the effective mass that smooths out the staggered oscillations by comparing only time slices $2a$ apart,

$$M_{\text{eff}}(t) = \frac{1}{2a}\left\{ \cosh^{-1}\left(\frac{G(t-1)}{G(T/2)}\right) - \cosh^{-1}\left(\frac{G(t+1)}{G(T/2)}\right)\right\}. \quad (4.20)$$

The inverse cosh terms are used instead of the typical logs to take better account of backward propagating states [182]. As expected the pseudoscalar effective masses are very well behaved with long plateaus, and the vector effective masses are noisier, though they too have easily identifiable plateaus.

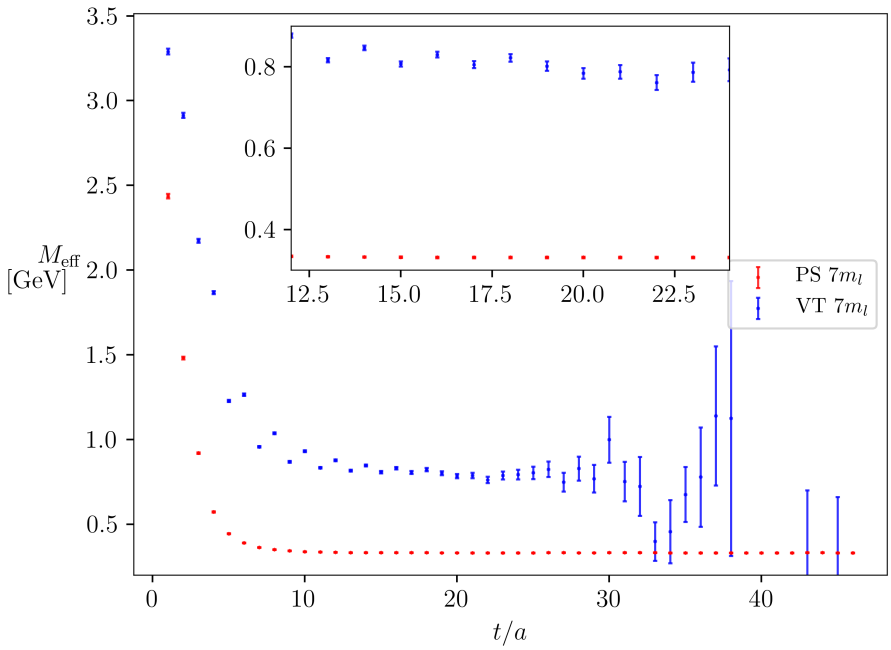

Figure 4.9: Effective mass plots for the pseudoscalar and vector correlators at $7m_l$ on the fine ensemble. The size of the errors are emphasised by the zoomed in subset shown on the inset axes.

We measure three sets of correlators, one uncharged where the SU(3) link fields are not multiplied by U(1) fields, and two charged with opposite electric charges. All the correlators are overall electrically neutral. As we are working in the Strong isospin symmetric limit this amounts to calculating correlators where the quark and antiquark swap charges. We calculate two sets of correlators in this way as the charged correlators are noisier than the uncharged correlators. This is due to the presence of a QED noise term proportional to the electric charge, e, in the propagator. To suppress this noise term we average over the two correlators with opposite charges.

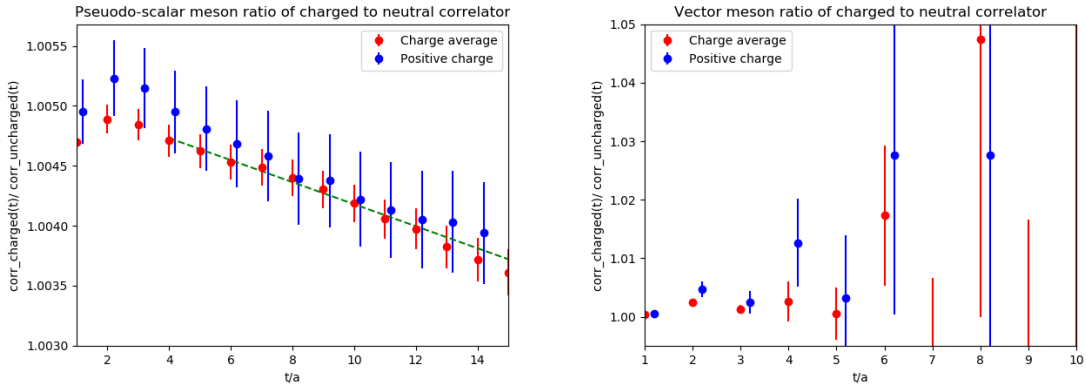

Figure 4.10: The variation with time of the ratio of the charged to neutral correlators with and without charge averaging, pseudoscalar on top and vector on the bottom. The oscillations in the vector correlator are an artefact of the staggered formalism.

To show that this charge averaging procedure leads to a marked reduction in uncertainty at the correlator level we can plot the correlators before and after charge averaging, and compare the uncertainties. This is shown in figure 4.10 for the pseudoscalar and vector correlators at the m_d on the very coarse ensemble. It is clear that charge averaging reduces the uncertainty in the pseudoscalar correlator by a factor of 2 or more, far beyond the $\sqrt{2}$ reduction we expect from doubling the statistics. This improvement holds over onto the noisier vector correlator.

We use 16 time sources on each field configuration to improve the statistics. All other things being equal this would increase the resources needed to run the simulations by a factor of 16. To mitigate this we use the truncated solver method (TSM). We take 16 sloppy solves with a residual of 10^{-3} and 1 precise solve with a residual of 10^{-6} before averaging over all the solves using the TSM equation 2.21. In figure 4.11 we show the variation in time of the fractional error of a m_u correlator on the very coarse ensemble with different combina-

tions of sloppy and precise solves. Included are the single time source correlators from sloppy and precise solves, the average over the sloppy solves, and the corrected correlator from the full TSM average. The fractional error is larger for a single source versus multiple sources, as we would expect. Comparing the fractional errors in the average over just the sloppy solves and the full corrected average we see no significant difference. This indicates that the sloppy solves are not systematically biased relative to the precise solve.

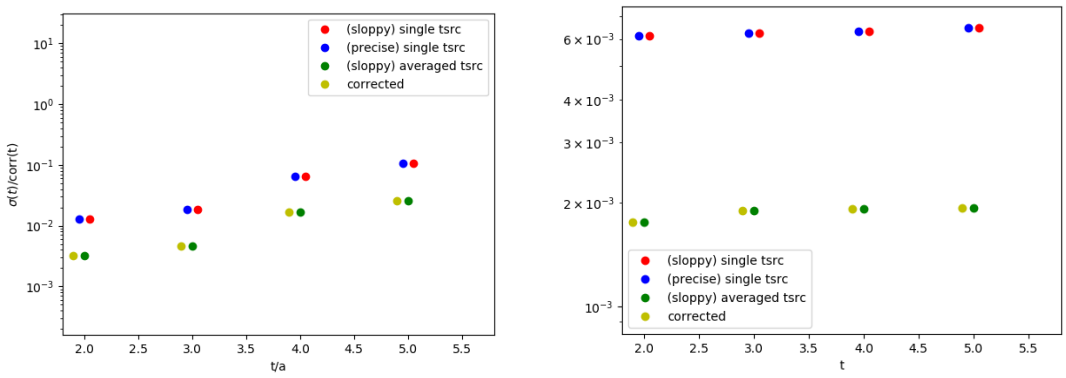

Figure 4.11: The fractional error on the very coarse ensemble of charge-averaged vector (left) and pseudoscalar (right) correlators as a function of time for different numbers of sources.

$L^3 \times T$	L[fm]	m_l/m_s	N_{cfgs}
$24^3 \times 64$	2.93	1/10	400
$40^3 \times 64$	4.89	1/10	100
$48^3 \times 64$	5.82	1/27	694

Table 4.4: Ensembles used in our finite volume study. The second column gives the spatial length of the lattices in fermi. The third column gives the ratio of the light quark mass to the strange quark mass. The fourth column lists the number of configurations used in our analysis.

4.4 Fitting Procedure

In keeping with the practices of the larger collaboration we blind our analysis at the correlator level. This is done by multiplying all the correlator elements by the same randomly chosen, hidden number between 0.95 and 1.05. This number is saved to disk and hashed so it can not be read easily or by mistake. Certain crosschecks, like the ϕ meson mass, are done with unblinded correlators. At some point in the near future the whole analysis will be unblinded, as that time has not been reached the main results of this work, $\delta a_\mu^{(s)}$ and $\delta a_\mu^{(l)}$, are presented in their blinded form.

When using equation 4.12 to calculate a_μ we encounter a problem with noise in the tail of the correlator. The uncertainty in the correlator grows exponentially with time. These noisier late-time points lead to larger uncertainties in the polarisation function and a_μ. In the past the collaboration has mitigated this problem by replacing the correlator data with fitted model data beyond a particular time slice, t^* [168, 91]. The sum in equation 4.12 is also truncated at t_{cut}. After replacement the correlator has the form,

$$C(t) = \begin{cases} C_{\text{data}}(t) & t \leq t^* \\ C_{\text{model}}(t) & t_{\text{cut}} \geq t > t^* \\ 0 & t > t_{\text{cut}}. \end{cases} \tag{4.21}$$

The vector correlators are fitted to a sum of exponentials,

$$C_{\text{model}}(t) = \sum_{i=0}^{N} a_i^2(e^{-E_i t} + e^{-E_i(T-t)}) + (-1)^t a_{i,o}^2(e^{-E_{i,o} t} + e^{-E_{i,o}(T-t)}), \tag{4.22}$$

where the a's and E's are the amplitudes and energies of the states included in the model. The terms with subscript o describe the oscillating states that are present in the vector correlator in the staggered formalism. The terms with exponent $T - t$ are needed in the model because the correlators are periodic. There are $N + N = 2N$ states in this model with $2N + 2N = 4N$ parameters. The oscillating terms are dropped for the pseudoscalar fits. In contrast to our hybrid analysis here all the fits are single channel.

We have a series of choices when deciding what subsection of the correlator we wish to fit. When fitting the vector we try to exclude as little correlator data as possible in order to capture information about the whole correlator. This is important as we don't want to miss out on any late-time behaviour and means we are willing to trade precision on the ground state for precision on the excited states. In practice we fit all the points in the range $[t_{\text{min}}, T-1-t_{\text{min}}]$, with t_{min} small. We use the Python libraries `g2tools, corrfitter, lsqfit` to do the fits [89, 183, 184]. The fit parameters and goodness-of-fit results are shown in table 4.5.

ensemble	fit range	svdcut	$\overline{\chi}^2$/Q	with noise*
Vector fits				
very coarse	[3-20]	5.4e-11	0.8/0.99	0.96/0.65
coarse	[4-28]	8.3e-07	0.41/1	0.99/0.52
fine	[4-40]	7.2e-05	0.2/1	0.96/0.73
Pseudoscalar fits				
very coarse	[2-23]	0.0007	0.32/1	0.80/0.99
coarse	[2-31]	0.011	0.12/1	0.81/0.99
fine	[2-47]	0.061	0.1/1	0.72/1

Table 4.5: Fit parameters and goodness-of-fit results for the vector and pseudoscalar fits.

In figure 4.12 we show that the vector fits are stable on the very coarse ensemble when varying t_{min}, and this behaviour is replicated on the other ensembles.

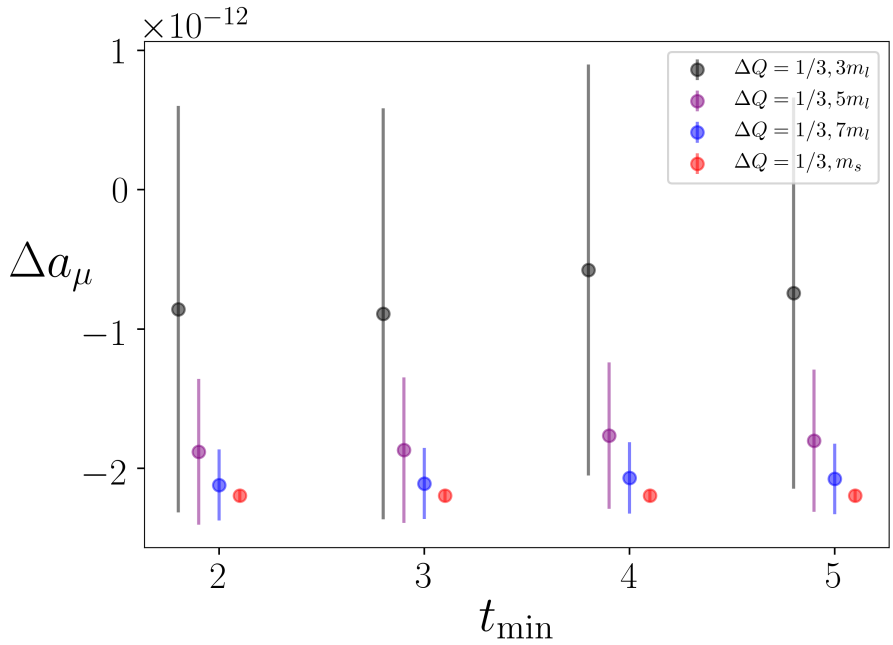

Figure 4.12: How Δa_μ varies with t_{min} and quark mass on the very coarse ensemble with $\Delta Q = 1/3$.

If measurements on adjacent or nearby configurations are not independent then the data has to be binned in order to remove autocorrelations. The binned data set is formed from the original by averaging adjacent configurations in bins of size N_B, leaving N_{cfg}/N_B configurations. Figure 4.13 shows the uncertainty in the bare QED correction stays the same size as the bin size is increased on the 0.15fm ensemble from one to eight. We observe similar behaviour on the other ensembles and across all quark masses and electric charges. We conclude from this that the extent of autocorrelations in the data is minimal, and choose a global bin size of 2.

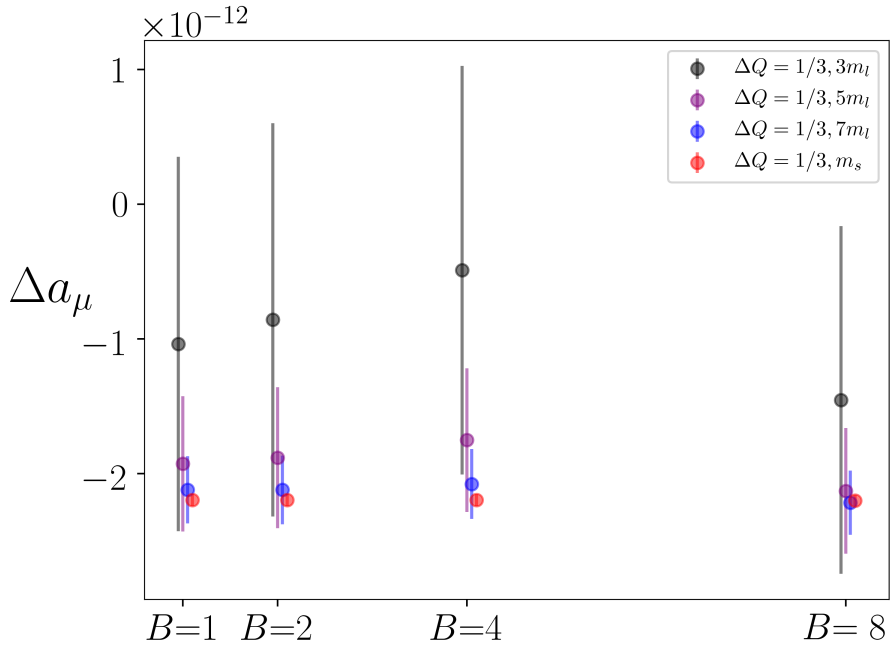

Figure 4.13: How Δa_μ varies with bin size and quark mass on the very coarse ensemble with $\Delta Q = 1/3$.

We apply an SVD cut to the data before fitting. The SVD cut is determined by comparing the eigenvalues of bootstrapped copies of the correlation matrix and the original correlation matrix. This is illustrated in figure 4.14 where the suggested SVD cut is given by the red dotted line and is placed where the bootstrap-averaged eigenvalues

fall below a certain fraction of the original eigenvalues, given by the dotted horizontal line. The SVD cuts on our ensembles are given in table 4.5. As one might expect, the SVD cuts are smallest on the very coarse ensemble and largest on the fine ensemble. Greater statistics allows the smaller eigenvalues of the correlation matrix to be accurately estimated.

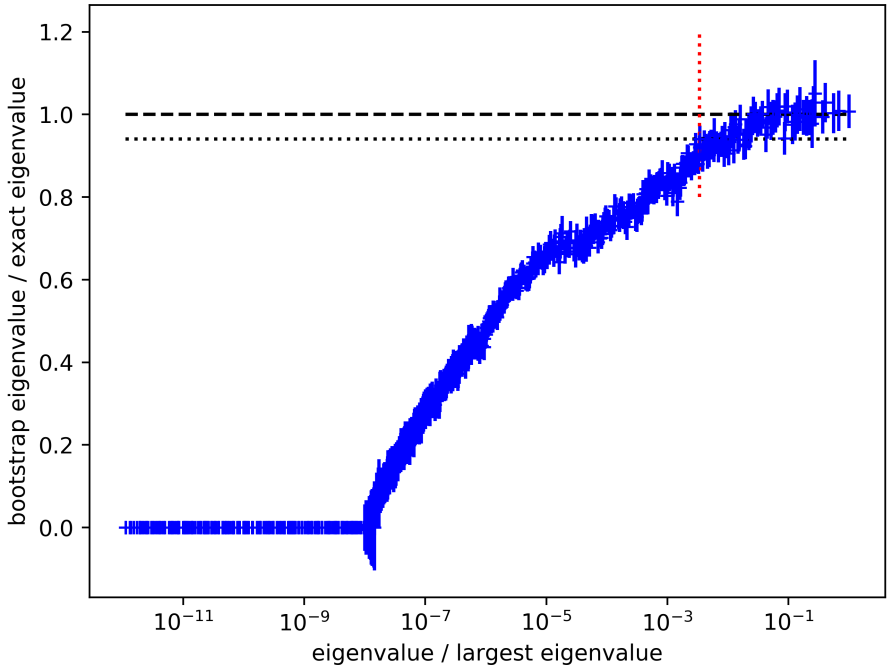

Figure 4.14: Comparison of eigenvalues of the bootstrapped and total correlation matrix for the vector correlator on the fine ensemble.

The introduction of new parameters, t^* and t_{cut}, will give rise to new systematic errors. Increasing t^* lowers the systematic error and increases the statistical error on a_μ. To investigate this we can vary the values of t^* and t_{cut} and examine the effect on the size and error of various quantities. Figure 4.15 shows how the fractional error in a_μ on the very coarse ensemble increases as we increase t^*. This behaviour is expected as the more noisy late time points are included in the transformation to the polarisation function. From figure 4.15 it is also

clear that, for a given number of configurations, the smaller the quark mass the greater the fractional error. Lighter quark masses lead to a much steeper increase in the fractional error of the correlator. There is an especially sharp deterioration between $3m_l$ and the physical point. The error in the physical up and down quark correlators renders them unusable much beyond 1.5 fm, which is why model replacement is needed when calculating the light connected HVP.

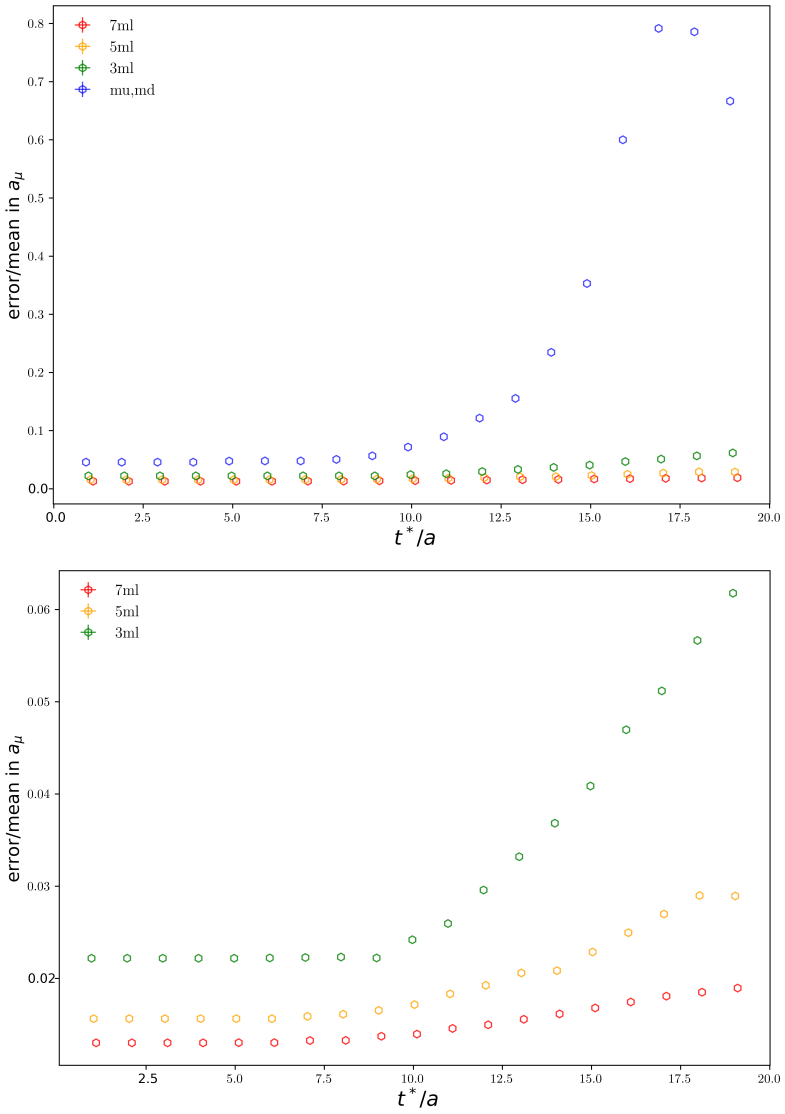

Figure 4.15: The fractional error of a_μ on the very coarse ensemble as a function of t^* for different quark masses. The lower pane is a zoomed in version of the upper pane and omits the physical point fractional error.

In the course of studying the dependence of Δa_μ on t^* and t_{cut} we have discovered that it may not be necessary to replace the data with a model. Instead we can simply take the sum in equation 4.11 up to the midpoint of the lattice. Figure 4.16 illustrates why we may do this by plotting the cumulative QED correction as a function of time while also varying t^*. Increasing t^* from 2 fm to 3.5 fm, the midpoint of the lattice, does not significantly change the value of Δa_μ although the uncertainty does increase a small amount.

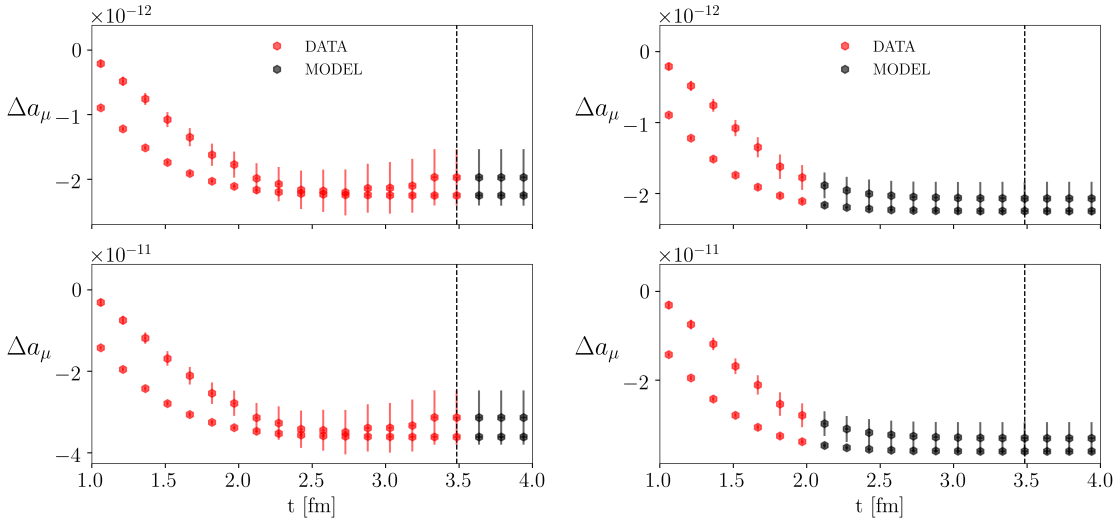

Figure 4.16: The cumulative QED correction to a_μ as a function of time at m_s and $7m_l$ on the very coarse ensemble. On the RHS $t^* = 2$fm and on the LHS $t^* = 3.5$fm. The midpoint of the lattice is indicated by a dashed line. The upper plots are for the $\Delta Q = 1/3$ corrections, the bottom are the $\Delta Q = 2/3$ corrections.

Δa_μ also does not change significantly as the sum is extended out to times greater than the midpoint of the lattice, as can be seen by the plateaus after the vertical dashed lines in figure 4.16. Both of these observations suggest we only need to include measured correlator data up to the midpoint of the lattice, no need for fits, model replacement, or extension in the time direction. If the correlators have period T the

input, $C(t)$, into equation 4.11 is

$$C(t) = \begin{cases} C_{\text{data}}(t) & t \leq T/2 \\ 0 & t > T/2 \quad . \end{cases} \tag{4.23}$$

4.5 Results

The QED corrections at equal bare quark mass, Δa_μ are shown in figure 4.17. The uncertainty of Δa_μ increases when the size of the charge is doubled and, as expected, grows rapidly with decreasing quark mass. It is also clear from figure 4.17 that the $\Delta Q = 1/3$ and $\Delta Q = 2/3$ corrections are highly correlated, not unexpected as the random wall source generated for the neutral correlator is reused for both the charged correlators. This is also why the results across the quark masses are correlated, with decreasing correlation the larger the quark mass difference.

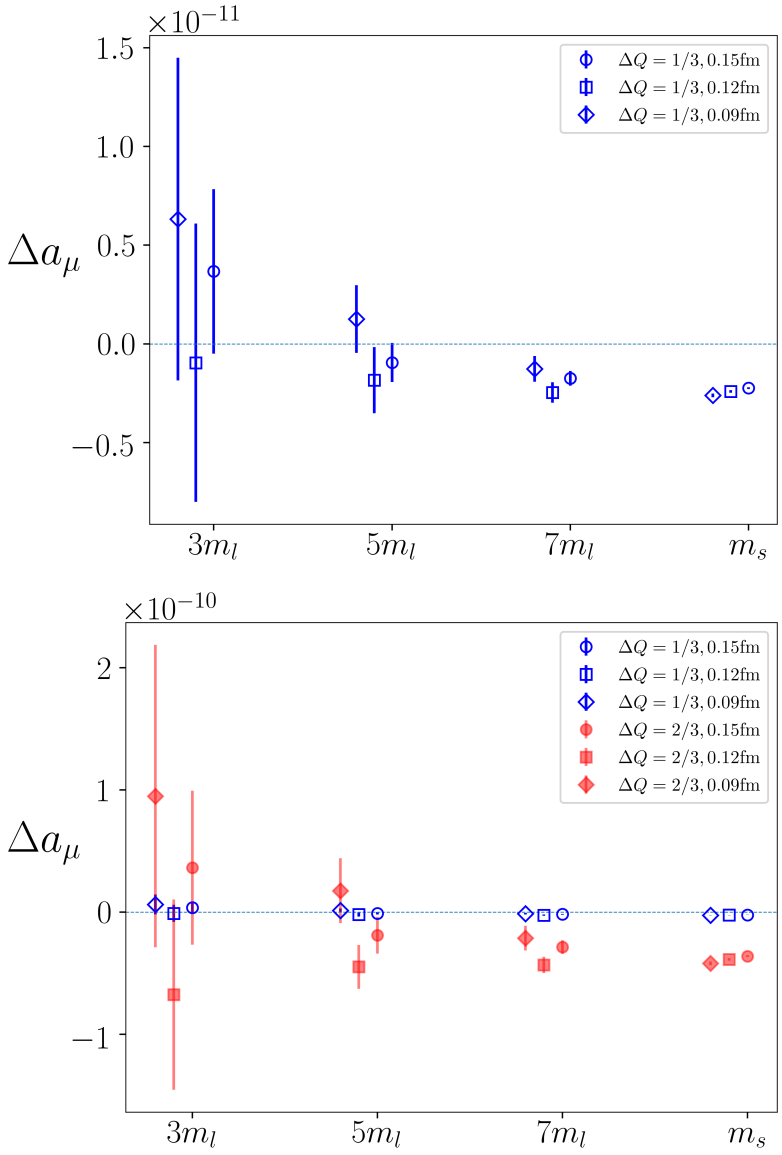

Figure 4.17: The non-renormalised QED corrections to a_μ for all the ensembles and quark masses. The top plot just shows the difference of the neutral and down-like ($Q = -1/3$) correlators, the bottom shows both the down-like and up-like ($Q = 2/3$) differences.

As a validation of our correlator data we can compute the values of simple hadronic observables, meson masses and decay constants, and compare to experiment and other lattice measurements. The strange vector correlator has the observed ϕ meson associated to its ground state. The energy of the ground state is one of the parameters of the fit and can be read off straight away and the vector decay constant is simply related to the ground state amplitude. The ϕ mass

and decay constant on our ensembles are plotted in figure 4.18. For the definition of the decay constant see equation 3.10 of chapter 3. The decay constant needs to be renormalised with a renormalisation factor, Z_V. These factors were calculated previously by HPQCD non-perturbatively in the RI-SMOM scheme [185]. Our results show good agreement with a prior HPQCD calculation across our ensembles and is consistent with experiment.

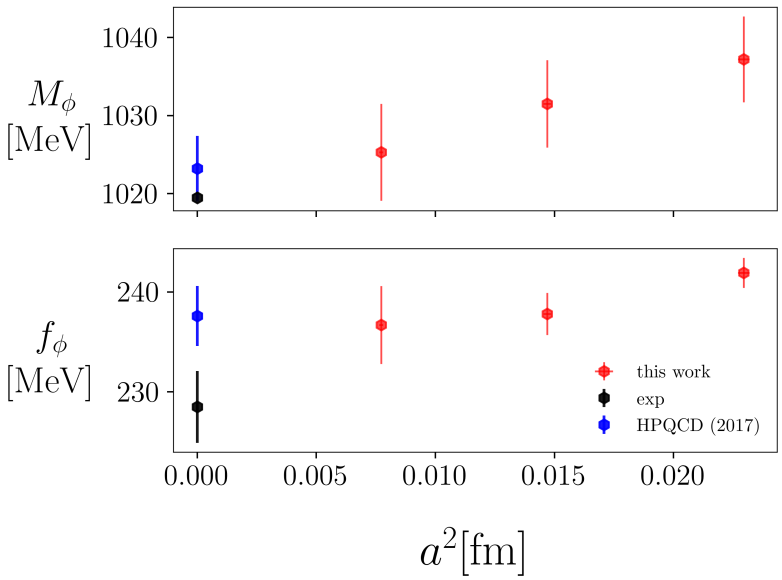

Figure 4.18: The measured mass, M_ϕ, and decay constant, f_ϕ, of the ground state of the vector meson correlators measured at the strange quark mass on each ensemble. These results are in line with the previous HPQCD result and experiment [186, 16].

The ground states of the $3/5/7m_l$ correlators do not correspond to physical states against which we can compare masses and decay constants. To make such a comparison we would need to perform a chiral extrapolation on our results. A simple extrapolation was performed on the PS ground state energy and the results agreed with the experimental π_0 mass. The light quark and strange quark masses were tuned to reproduce physical observables so, in a sense, we are

validating the tuning here.

Before examining the QED correction to the connected light HVP we examine the correction to the connected strange HVP. The reasons for this are twofold; the vector current-current measurements were taken at the physical strange quark mass, so no extrapolation in the quark mass is needed; and fewer configurations are required to distinguish the effect of QED at heavier quark masses.

4.5.1 The strange quark contribution

In order to assess the magnitude of possible QED finite volume effects on $\Delta a_\mu^{(s)}$ we computed vector correlators on ensembles with varying spatial volumes. For this analysis we re-use the coarse correlators we calculated on the physical ensemble and add two ensembles with a similar lattice spacing and unphysically heavy pions, see table 4.4. The largest ensemble is around twice as long as the smallest ensemble and therefore has around 8 times the volume. We can define the ratio of a quantity with and without QED,

$$R^0_{\text{QED}}[X] \equiv \frac{X[\text{QCD+qQED}]}{X[\text{QCD}]} \quad \text{at fixed } am_s, \tag{4.24}$$

and look at how this ratio varies with lattice volume. Figure 4.19 shows how $\Delta a_\mu^{(s)}$ and $R^0_{\text{QED}}[a_\mu^{(s)}]$ vary with the inverse lattice size, $1/L_s$. It is clear from figure 4.19 that QED FVE on $\Delta a_\mu^{(s)}$ are negligible for the statistics and size of ensembles used. Even with the unphysical (for the strange quark) larger electric charge $Q_s = -2/3$ the maximum deviation is only slightly above 1σ.

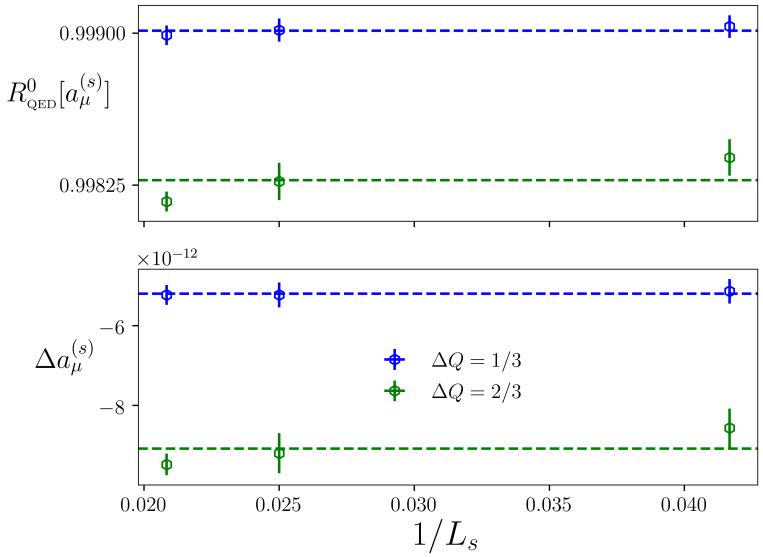

Figure 4.19: How $R^0_{\rm QED}[a_\mu^{(s)}]$ and $\Delta a_\mu^{(s)}$ vary with inverse spatial lattice extent for $\Delta Q = -1/3, 2/3$. The dashed lines are the mean of the three values.

The strange quark contribution makes up around 7% of a_μ. The QED contribution, $\delta a_\mu^{(s)}$, to $a_\mu^{(s)}$ is obtained by taking the $Q = 0$ and $Q = -1/3$ strange vector correlators and computing $a_\mu^{(s)}$ and Δa_μ, before applying the EM renormalisation via equation 4.17 to obtain δa_μ. We note that the scheme adjustment on the fine ensemble is very noisy, this is because the chiral extrapolation of the PS mass to m_l needed to get the quark mass shift, δ_d, is less constrained on the fine ensemble. After the scheme adjustment the continuum limit needs to be taken. As the HISQ action has lattice artefacts of $\mathcal{O}(a^2)$ the data is fit to a simple function, linear in a^2, before taking the $a \to 0$ limit. The extrapolation function used is,

$$\delta a_\mu^{(s)}(a^2) = c_0(1 + c_1(a\Lambda)^2), \tag{4.25}$$

where the c_i are parameters to be fitted, a is the lattice spacing, and

we multiply a by the QCD scale Λ, which we take as 0.5 GeV, in order to make c_1 dimensionless.

The extrapolation in a^2 is plotted in figure 4.20 and the fitted parameters are listed in table 4.6. The fit is satisfactory with goodness of fit parameters $\overline{\chi}^2 = 0.21$ for the $a_\mu^{(s)}$ extrapolation and $\overline{\chi}^2 = 0.0014$ for the $\delta a_\mu^{(s)}$ extrapolation. From figure 4.20 it is clear the slope in a^2 is mild and the posterior for c_1 is consistent with a horizontal band.

param	prior	posterior
$\delta a_\mu^{(s)}$		
c_0	$0(1)\times 10^{-10}$	$-0.0092(81)\times 10^{-10}$
c_1	0(100)	0.3(6.4)
$a_\mu^{(s)}$		
c_0	$0(1)\times 10^{-8}$	$54.38(80)\times 10^{-10}$
c_1	0(1)	-0.22(14)

Table 4.6: Priors and fitted results for the parameters of the continuum extrapolations of $\delta a_\mu^{(s)}$ and $a_\mu^{(s)}$.

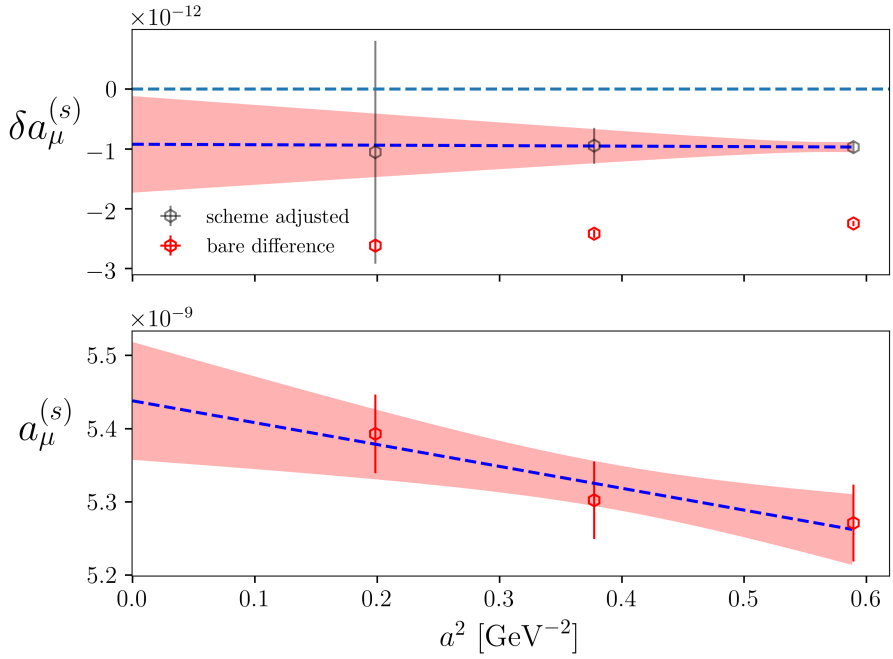

Figure 4.20: The continuum extrapolations of $\delta a_\mu^{(s)}$ and $a_\mu^{(s)}$. See equation 4.25 and table 4.6 for the fit function and fitted parameter values.

The extrapolated continuum values are,

$$\begin{aligned} \delta a_\mu^{(s)} &= -0.0092(81)\times 10^{-10} \\ a_\mu^{(s)} &= 54.38(80)\times 10^{-10}\,, \end{aligned} \tag{4.26}$$

where we remind the reader that these are blinded results. Our computed absolute uncertainty, 0.0081×10^{-10}, contributes a tiny amount to the overall uncertainty of a_μ.

4.5.2 The light quark contribution contribution

The light quark contribution to a_μ comes from quark loops formed from up and down quarks. We work in the Strong isospin symmetric limit where the up and down quarks have the same mass (in QCD), $m_l = 0.5(m_u^{\text{phys}} + m_d^{\text{phys}})$. $a_\mu^{(l)}$ makes up the lion's share, around 90%, of the total value of a_μ. Since measurements at the physical pion mass are expensive (in time and resources) and noisy we measure vector correlators at $3/5/7m_l$ before extrapolating to $a = 0$ and $m_q = m_l$.

The procedure to obtain $\delta a_\mu^{(l)}$ is essentially the same as that described above for $\delta a_\mu^{(s)}$. To aid the calculation we split up $\delta a_\mu^{(l)} = \delta a_\mu^{(u)} + \delta a_\mu^{(d)}$. $\delta a_\mu^{(d)}$ is calculated using the $Q = 0, 1/3$ correlators and $\delta a_\mu^{(u)}$ is calculated from the $Q = 0, 2/3$ correlators. To find the physical value of $\delta a_\mu^{(l)}$ we do a combined chiral-continuum extrapolation for each piece before adding them together. We fit our data to the

following functional form,

$$\begin{aligned} \delta a_\mu^{(d)}(a^2, m_q/m_l) &= c_0(1 + c_1(a\Lambda)^2 + c_2 m_q/m_l) \\ \delta a_\mu^{(u)}(a^2, m_q/m_l) &= c_0(1 + c_1(a\Lambda)^2 + c_2 m_q/m_l), \end{aligned} \tag{4.27}$$

which has a similar form to the extrapolation used for the strange quark contribution. The $c_2 m_q/m_l$ term controls the extrapolation in quark mass. We again use $\Lambda = 0.5$ GeV. We are fitting 6 parameters to 3 masses $\times$ 3 ensembles $\times$ 2 (u/d) = 18 pieces of data. We fit all 6 parameters simultaneously to account for correlations between measurements on the same ensemble.

We plot both the continuum and chiral extrapolations of $\delta a_\mu^{(u)}, \delta a_\mu^{(d)}$ in figure 4.21 and list the fitted values of the c_i in table 4.7.

param	prior	posterior
$\delta a_\mu^{(u)}$		
c_0	$0(1)\times 10^{-9}$	$-1.2(1.6)\times 10^{-11}$
c_1	0(1)	-0.17(86)
c_2	0(1)	0.06(23)
$\delta a_\mu^{(d)}$		
c_0	$0(1)\times 10^{-10}$	$-0.5(1.0)\times 10^{-12}$
c_1	0(1)	-0.06(94)
c_2	0(1)	0.14(51)

Table 4.7: Priors and fitted results for the parameters of the chiral-continuum extrapolation of $\delta a_\mu^{(l)}$. See equations 4.27 for fit function.

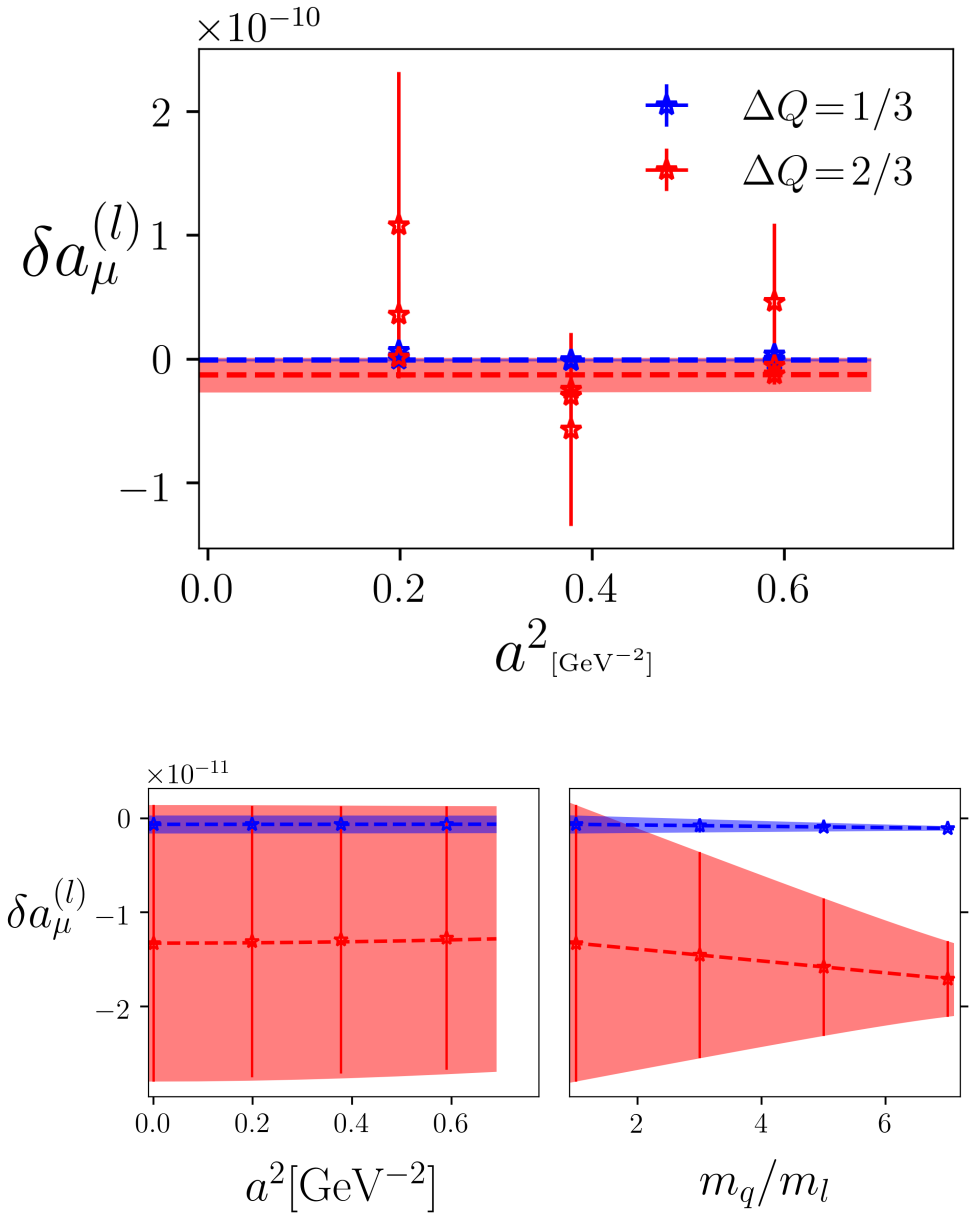

Figure 4.21: The chiral-continuum extrapolations of $\delta a_\mu^{(u)}$ (red) and $\delta a_\mu^{(d)}$ (blue). Bottom left is the extrapolation in the lattice spacing at $m_q/m_l = 1$ and on bottom right is the extrapolation in quark mass at $a = 0$, see equations 4.27 and table 4.7. The top plot shows the results at each lattice spacing and quark mass along with the extrapolation in the lattice spacing at $m_q/m_l = 1$.

Our extrapolated value for the quenched QED correction to the light connected HVP is

$$\delta a_\mu^{(l)}(a^2 = 0, m_q/m_l = 1) = -1.3(1.5) \times 10^{-11} \,. \tag{4.28}$$

If the correlations between quark masses and charges are turned off we find an extrapolated $\delta a_\mu^{(l)} = 1.9(3.4) \times 10^{-11}$.

4.6 Conclusions

We have used staggered quarks, gluon fields generated with the HISQ action, and U(1) fields generated with the QED_L prescription to measure vector correlators at a series of lattice spacings and light quark masses. From these correlators we have computed the QED corrections to the light and strange connected HVPs. Our continuum and chiral extrapolated results complement and extend previous work by the HPQCD/MILC/Fermilab Lattice collaborations [138, 168, 169, 91, 187].

Our results suggest the total QED correction to the connected HVP is small, with an absolute uncertainty less than 1×10^{-10}. This is well below the threshold necessary (but not sufficient) for sub percent precision on the total HVP ($\leq 5 \times 10^{-10}$), which is the goal of ongoing efforts by the joint HPQCD/MILC/Fermilab Lattice collaboration. Meeting this goal will ensure the theory uncertainty of the HVP contribution to a_μ is competitive with the experimental uncertainty determined by the E989 and J-PARC collaborations.

Comparing our results with other groups' is complicated by the scheme dependence of the QED correction and by the fact that our analysis is blinded. The blinding effect should not change the final result by a large amount, say an order of magnitude, because the numerical factor used to multiply the correlator is close to one. The

scheme dependence of δa_μ is larger at m_s, and less important for the light connected HVP where it is of a comparable size to the statistical uncertainty. Therefore, with those qualifiers in mind, we can attempt to compare our results to other groups, focusing on the sign and size of the correction, and the size of the errors. We discuss the main results of this work at the strange and light quark masses in turn. All the numerical values are given in units of 10^{-10} (i.e. multiplied by 10^{10}).

4.6.1 The strange quark contribution

Our blinded continuum extrapolated value for $a_\mu^{(s)}$ is 54.38(80). This value comes from an extrapolation of the pure QCD data, the QCD+QED number is the same to two decimal places. Our result is plotted in figure 4.22, along with the values determined by other groups: The earlier HPQCD value of 53.41(49) was also determined with staggered quarks and the HISQ action [138]; the ETM value of 53.1(2.5) was determined with the Iwasaki action for the gluons and Wilson Twisted Mass action for the quarks [180]; the RBC/UKQCD value of 53.2(0.4) was calculated using the DBW2 gauge action and domain wall valence quarks [188]; the BMW value of 53.393(89) was determined using staggered quarks and the `4stout` action [77]. All these calculations used at least three lattice spacings, except for the RBC/UKQCD value which had two. Only ETM did not use ensembles with physical pions. The relative precision of the BMW value is due to improved scale setting through w_0 and large statistics at 6 lattice spacings down to 0.064 fm. These results are shown in figure 4.22, where there is clearly excellent agreement between all the results for $a_\mu^{(s)}$. That a wide variety

of independent lattice calculations, using different quark formulations and actions, agree on the value of $a_\mu^{(s)}$ should give us confidence in the robustness of our result and suggests the strange connected HVP is well understood on the lattice.

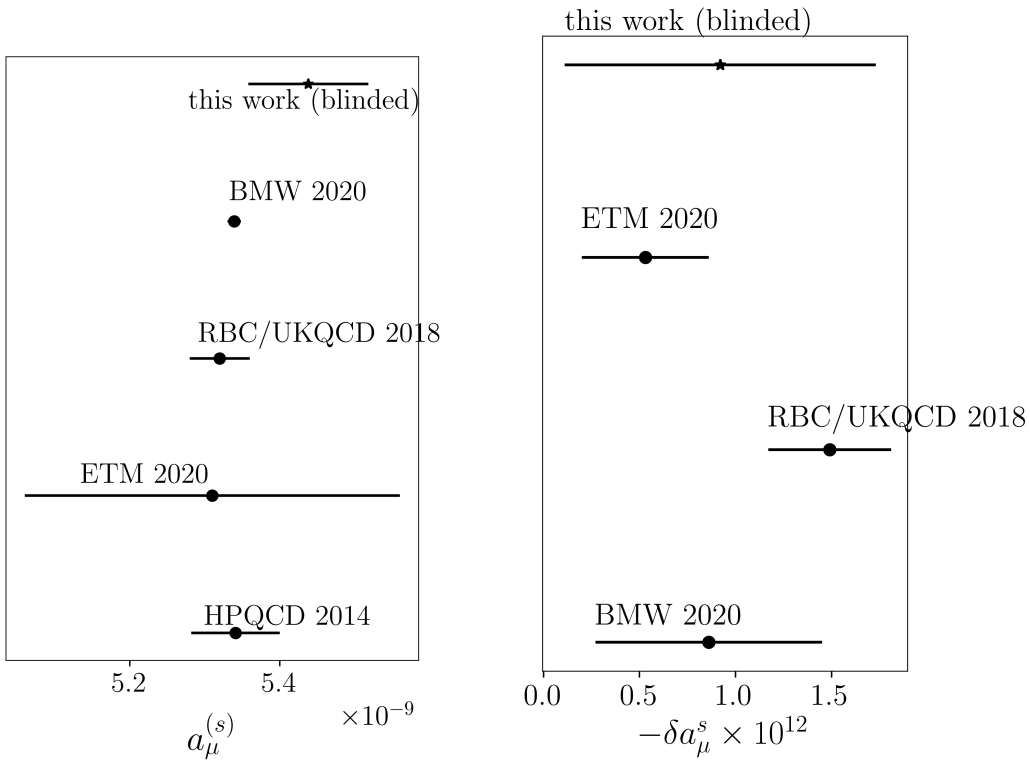

Figure 4.22: Comparison of our extrapolated value for $a_\mu^{(s)}$ and $\delta a_\mu^{(s)}$ with its determination by other groups.

Our blinded result for the QED correction to the strange connected HVP is $\delta a_\mu^{(s)} = -0.0092(81)$. This is also plotted in figure 4.22 with other groups' determinations. Although the computational strategy varies from group to group, they all also used the QED_L prescription. The ETM value of $-0.0053(30)$ was determined with an equal quark mass (GRS) renormalisation scheme [189]. The RBC/UKQCD value of $-0.0149(32)$ was determined by calculating individual Feynman diagrams perturbatively [188]. The BMW collaboration computed their value of $-0.0086(59)$ by measuring derivatives with respect to electric

charge of fermionic determinants [77]. It is notable that all these results have the same negative sign and are of a similar size. The BMW value is computed in the same Dashen-inspired scheme we use and so would be directly comparable were it not for the blinding.

4.6.2 The light quark contribution

The light connected part of the HVP is the largest piece and has the largest uncertainty. We do not present extrapolated results for $a_\mu^{(l)}$ as it has large taste-breaking and FV corrections, and is not the focus of this work. A separate effort is underway to reduce its uncertainty to the required sub percent level with physical point measurements.

Our blinded result for the QED correction to the light connected HVP is $\delta a_\mu^{(l)} = -0.13(15)$. This is plotted in figure 4.23 with other groups' results. These results are from the same papers cited above for the $\delta a_\mu^{(s)}$ values. The ETM value of 1.1(1.0) is a chiral-continuum extrapolation using measurements with pion masses down to 210 MeV. The RBC/UKQCD measurement was done at the physical point and one lattice spacing only, and yielded a value of 5.9(5.9). The BMW collaboration computed a value of $-1.23(50)$ in a similar manner to this work, measuring at multiples of the light quark mass κm_l ($\kappa = 3, 5, 7, 9, 11$), before performing a chiral-continuum extrapolation.

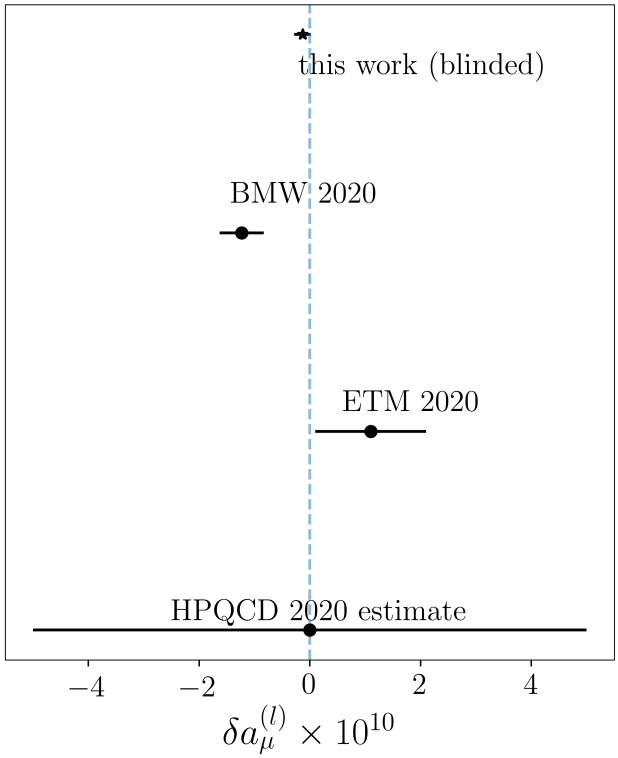

Figure 4.23: Comparison of our extrapolated value for $\delta a_\mu^{(l)}$ against its determination by other groups.

Our result for $\delta a_\mu^{(l)}$ suggests the estimate for the QED correction by the HPQCD, MILC, and Fermilab lattice collaboration in [91] was too conservative. Our result, with the caveat that it is blinded, has a large relative uncertainty in line with other calculations, but a small absolute uncertainty. This appears to be due to the presence of correlations between measurements on the same configuration, and is evidenced by the increase in the absolute uncertainty of $\delta a_\mu^{(l)}$ by a factor of 2.3 when these correlations are ignored.

4.6.3 Future Work

There are three areas of improvement of the present work: The lack of lattices with spacings below 0.09 fm, the lack of measurements with

valence quarks at m_l, and the omission of QED in the sea.

Adding measurements on ensembles with smaller lattice spacings would allow a better controlled continuum extrapolation. This is a straightforward extension of this work as the MILC collaboration already have gluon field ensembles available at 0.06 fm and below. The authors of [90] have suggested that 0.06 fm and finer ensembles are necessary for a controlled extrapolation in a^2 when using staggered quarks, though it is unclear whether this applies to QED corrections. Adding a finer ensemble, ideally at 0.06 fm, would also enable us to drop the very coarse 0.15 fm ensemble from our extrapolations.

The smallest quark mass we simulated at on all three ensembles was $3m_l$, which corresponds to a pion mass of $\sim$ 230 MeV. These measurements required around 300,000 GPU-core hours of computer time. It is clear from the size of the uncertainty of the RBC/UKQCD determination of $\delta a_\mu^{(l)} = 5.9(5.9)$ that simulating at the physical point would require an order of magnitude more resources and/or significant algorithmic improvements to meet our target uncertainty. A standalone calculation of the QED corrections at the physical point is therefore, absent algorithmic improvements, infeasible. However, it may be that simulating closer to the physical point, say at $2m_l$, ought to be considered (we note that the physical down quark mass is around $4m_l/3$ and the up mass is around $2m_l/3$).

Ultimately future calculations of QED corrections to the HVP, and lattice observables generally, will include QED in the sea directly. Such a calculation is a natural extension of this work. Although it will make little impact on the values of the quantities we've considered

(as suggested by estimates from PT and the BMW calculation) it makes the interpretation of the results conceptually simpler as QED effects are included to all orders in the valence and sea sectors. The major drawback is that new dynamical QCD+QED ensembles must be generated, and this is a time and resource intensive process. Even so, that process will provide valuable experience for the inevitable subsequent lattice calculations that require the inclusion of dynamical QED. Starting this process sooner rather than later may be wise as it is a matter of when not if precision lattice calculations switch over.

Bibliography

[1] M. E. Peskin and D. V. Schroeder, *An Introduction to Quantum Field Theory*. Addison-Wesley, Reading, USA, 1995.

[2] M. Maggiore, *A Modern Introduction to Quantum Field Theory*. 2005.

[3] M. Creutz, *Quarks, gluons and lattices*. Cambridge Monographs on Mathematical Physics. Cambridge Univ. Press, Cambridge, UK, June, 1985.

[4] T. DeGrand and C. E. Detar, *Lattice Methods for Quantum Chromodynamics*. 2006.

[5] J. Smit, *Introduction to Quantum Fields on a Lattice: 'a robust mate'*, vol. 15. Cambridge University Press, Jan., 2011.

[6] F. Zwicky, "On the masses of nebulae and of clusters of nebulae," *Astrophysical Journal* **86** (Oct., 1937) 217. tex.adsnote: Provided by the SAO/NASA Astrophysics Data System tex.adsurl: https://ui.adsabs.harvard.edu/abs/1937ApJ....86..217Z.

[7] V. C. Rubin and J. Ford, W. Kent, "Rotation of the andromeda nebula from a spectroscopic survey of emission regions," *Astrophysical Journal* **159** (Feb., 1970) 379. tex.adsnote: Provided by the SAO/NASA Astrophysics Data System tex.adsurl: https://ui.adsabs.harvard.edu/abs/1970ApJ...159..379R.

[8] P. J. E. Peebles and B. Ratra, "The Cosmological Constant and Dark Energy," *Rev. Mod. Phys.* **75** (2003) 559–606. _eprint: astro-ph/0207347.

[9] L. Perivolaropoulos and F. Skara, "Challenges for ΛCDM: An update,". http://arxiv.org/abs/2105.05208.

[10] M. Gell-Mann, "The Eightfold Way: A Theory of strong interaction symmetry,".

[11] M. Gell-Mann, "A Schematic Model of Baryons and Mesons," *Phys. Lett.* **8** (1964) 214–215.

[12] G. Zweig, "An SU(3) model for strong interaction symmetry and its breaking. Version 2," in *DEVELOPMENTS IN THE QUARK THEORY OF HADRONS. VOL. 1. 1964 - 1978*, D. B. Lichtenberg and S. P. Rosen, eds., pp. 22–101. Feb., 1964.

[13] D. J. Gross and F. Wilczek, "Ultraviolet Behavior of Nonabelian Gauge Theories," *Phys. Rev. Lett.* **30** (1973) 1343–1346.

[14] H. D. Politzer, "Reliable Perturbative Results for Strong Interactions?," *Phys. Rev. Lett.* **30** (1973) 1346–1349.

[15] S. Weinberg, "Nonabelian Gauge Theories of the Strong Interactions," *Phys. Rev. Lett.* **31** (1973) 494–497.

[16] P. A. Zyla and others, "Review of Particle Physics," *PTEP* **2020** no. 8, (2020) 083C01.

[17] K. G. Wilson and J. Kogut, "The renormalization group and the expansion," *Physics Reports* **12** no. 2, (1974) 75–199.

[18] M. Creutz, "Diseases with rooted staggered quarks," *Proceedings of Science* **32** (2006) .

[19] W. I. Jay, A. Lytle, C. DeTar, A. X. El-Khadra, E. Gamiz, Z. Gelzer, S. Gottlieb, A. Kronfeld, J. Simone, and A. Vaquero, "B- and D-meson semileptonic decays with highly improved staggered quarks," in *PoS*, vol. LATTICE2021, p. 109. 2022. _eprint: 2111.05184.

[20] H. B. Nielsen and M. Ninomiya, "Absence of Neutrinos on a Lattice. 1. Proof by Homotopy Theory," *Nucl. Phys. B* **185** (1981) 20.

[21] K. G. Wilson, "Quarks and Strings on a Lattice," in *13th International School of Subnuclear Physics: New Phenomena in Subnuclear Physics*. Nov., 1975.

[22] H. B. Nielsen and M. Ninomiya, "No Go Theorem for Regularizing Chiral Fermions," *Phys. Lett. B* **105** (1981) 219–223.

[23] D. B. Kaplan, "A Method for simulating chiral fermions on the lattice," *Phys. Lett. B* **288** (1992) 342–347. _eprint: hep-lat/9206013.

[24] Y. Shamir, "Chiral fermions from lattice boundaries," *Nucl. Phys. B* **406** (1993) 90–106. _eprint: hep-lat/9303005.

[25] R. Narayanan and H. Neuberger, "A Construction of lattice chiral gauge theories," *Nucl. Phys. B* **443** (1995) 305–385. _eprint: hep-th/9411108.

[26] H. Neuberger, "Exactly massless quarks on the lattice," *Phys. Lett. B* **417** (1998) 141–144. _eprint: hep-lat/9707022.

[27] L. Susskind, "Lattice Fermions," *Phys. Rev. D* **16** (1977) 3031–3039.

[28] H. S. Sharatchandra, H. J. Thun, and P. Weisz, "Susskind fermions on a euclidean lattice," *Nuclear Physics, Section B* **192** no. 1, (1981) 205–236.

[29] H. Kluberg-Stern, A. Morel, O. Napoly, and B. Petersson, "Flavours of lagrangian Susskind fermions," *Nuclear Physics, Section B* **220** no. 4, (1983) 447–470.

[30] M. F. Golterman and J. Smit, "Self-energy and flavor interpretation of staggered fermions," *Nuclear Physics, Section B* **245** no. C, (1984) 61–88.

[31] G. Parisi and Y. c. Zhang, "STAGGERED FERMIONS AND ROTATION GAUGE INVARIANCE," *Nucl. Phys. B* **230** (1984) 97–108.

[32] D. Verstegen, "Symmetry properties of fermionic bilinears in lattice QCD," *Nuclear Physics, Section B* **249** no. 4, (1985) 685–703.

[33] M. F. Golterman, "Staggered mesons," *Nuclear Physics, Section B* **273** no. 3-4, (1986) 663–676.

[34] G. W. Kilcup and S. R. Sharpe, "A tool kit for staggered fermions," *Nuclear Physics, Section B* **283** no. C, (1987) 493–550.

[35] C. T. H. Davies and others, "High precision lattice QCD confronts experiment," *Phys. Rev. Lett.* **92** (2004) 022001. _eprint: hep-lat/0304004.

[36] K. Symanzik, "Continuum Limit and Improved Action in Lattice Theories. 1. Principles and phi**4 Theory," *Nucl. Phys. B* **226** (1983) 187–204.

[37] G. Curci, P. Menotti, and G. Paffuti, "Symanzik's Improved Lagrangian for Lattice Gauge Theory," *Physics Letters B* **130** no. 3, (1983) 205–208.

[38] E. Follana, Q. Mason, C. Davies, K. Hornbostel, G. P. Lepage, J. Shigemitsu, H. Trottier, and K. Wong, "Highly improved staggered quarks on the lattice with applications to charm physics," *Physical Review D - Particles, Fields, Gravitation and Cosmology* **75** no. 5, (2007) 1–21. http://arxiv.org/abs/hep-lat/0610092%0Ahttp://dx.doi.org/10.1103/PhysRevD.75.054502.

[39] S. Naik, "On-shell Improved Lattice Action for QCD With Susskind Fermions and Asymptotic Freedom Scale," *Nucl. Phys. B* **316** (1989) 238–268.

[40] M. Creutz, "Chiral anomalies and rooted staggered fermions," *Physics Letters, Section B: Nuclear, Elementary Particle and High-Energy Physics* **649** no. 2-3, (2007) 230–234.

[41] S. Dürr, "Theoretical issues with staggered fermion simulations," *Proceedings of Science* **20** no. July, (2005) .

[42] S. R. Sharpe, "Rooted staggered fermions: Good, bad or ugly?," *Proceedings of Science* **32** (2006) .

[43] A. S. Kronfeld, "Lattice gauge theory with staggered fermions: how, where, and why (not)," *Proceedings of Science* **42** (2007) .

[44] M. Golterman, "QCD with rooted staggered fermions," *Proceedings of Science* **77** (2008) .

[45] W. Pauli and F. Villars, "On the Invariant regularization in relativistic quantum theory," *Rev. Mod. Phys.* **21** (1949) 434–444.

[46] G. 't Hooft and M. J. G. Veltman, "Regularization and Renormalization of Gauge Fields," *Nucl. Phys. B* **44** (1972) 189–213.

[47] G. Martinelli, C. Pittori, C. T. Sachrajda, M. Testa, and A. Vladikas, "A General method for nonperturbative renormalization of lattice operators," *Nucl. Phys. B* **445** (1995) 81–108. _eprint: hep-lat/9411010.

[48] E. Franco and V. Lubicz, "Quark mass renormalization in the MS-bar and RI schemes up to the NNLO order," *Nucl. Phys. B* **531** (1998) 641–651. _eprint: hep-ph/9803491.

[49] K. G. Chetyrkin and A. Retey, "Renormalization and running of quark mass and field in the regularization invariant and MS-bar schemes at three loops and four loops," *Nucl. Phys. B* **583** (2000) 3–34. _eprint: hep-ph/9910332.

[50] D. Hatton, C. T. Davies, G. P. Lepage, and A. T. Lytle, "Renormalizing vector currents in lattice QCD using momentum-subtraction schemes," *Physical Review D* **100** no. 11, (2019) 114513. https://doi.org/10.1103/PhysRevD.100.114513. Publisher: American Physical Society.

[51] C. Sturm, Y. Aoki, N. H. Christ, T. Izubuchi, C. T. C. Sachrajda, and A. Soni, "Renormalization of quark bilinear operators in a momentum-subtraction scheme with a nonexceptional subtraction point," *Phys. Rev. D* **80** (2009) 014501. _eprint: 0901.2599.

[52] P. A. M. Dirac, "The quantum theory of the electron,".

[53] S. Tomonaga, "On a relativistically invariant formulation of the quantum theory of wave fields," *Prog. Theor. Phys.* **1** (1946) 27–42.

[54] R. P. Feynman, "Space - time approach to quantum electrodynamics," *Phys. Rev.* **76** (1949) 769–789.

[55] R. P. Feynman, "Mathematical formulation of the quantum theory of electromagnetic interaction," *Phys. Rev.* **80** (1950) 440–457.

[56] J. S. Schwinger, "On Quantum electrodynamics and the magnetic moment of the electron," *Phys. Rev.* **73** (1948) 416–417.

[57] F. J. Dyson, "The Radiation theories of Tomonaga, Schwinger, and Feynman," *Phys.Rev.* **75** (1949) 486–502. https://inspirehep.net/literature/573.

[58] A. Duncan, E. Eichten, and H. Thacker, "Electromagnetic splittings and light quark masses in lattice QCD," *Physical Review Letters* **76** no. 21, (1996) 3894–3897.

[59] M. G. Endres, A. Shindler, B. C. Tiburzi, and A. Walker-Loud, "Massive photons: an infrared regularization scheme for lattice QCD+QED," *Phys. Rev. Lett.* **117** no. 7, (2016) 072002. _eprint: 1507.08916.

[60] B. Lucini, A. Patella, A. Ramos, and N. Tantalo, "Charged hadrons in local finite-volume QED+QCD with C$^{\$}$ boundary conditions," *JHEP* **02** (2016) 076. _eprint: 1509.01636.

[61] M. Hansen, B. Lucini, A. Patella, and N. Tantalo, "Simulations of QCD and QED with C* boundary conditions," *EPJ Web Conf.* **175** (2018) 09001. _eprint: 1710.08838.

[62] M. Hayakawa and S. Uno, "QED in finite volume and finite size scaling effect on electromagnetic properties of hadrons," *Prog. Theor. Phys.* **120** (2008) 413–441. _eprint: 0804.2044.

[63] D. Hatton, C. T. H. Davies, and G. P. Lepage, "QED interaction effects on heavy meson masses from lattice QCD+QED," *Physical Review D* **102** no. 9, (Nov., 2020) 094514. http://arxiv.org/abs/2009.07667. arXiv: 2009.07667.

[64] D. Hatton, C. T. Davies, G. P. Lepage, and A. T. Lytle, "Renormalization of the tensor current in lattice QCD and the J / tensor decay constant," *Physical Review D* **102** no. 9, (2020) 94509. https://doi.org/10.1103/PhysRevD.102.094509. Publisher: American Physical Society.

[65] D. Hatton, C. T. H. Davies, J. Koponen, G. P. Lepage, and A. T. Lytle, "Determination of $\overline{m}_b/\overline{m}_c$ and $\overline{m}_b$ from $n_f=4$ lattice QCD$+$QED,". http://arxiv.org/abs/2102.09609.

[66] D. Hatton, C. T. Davies, J. Koponen, G. P. Lepage, and A. T. Lytle, "Bottomonium precision tests from full lattice QCD: Hyperfine splitting, i leptonic width, and b quark contribution to e+e- →hadrons," *Physical Review D* **103** no. 5, (2021) 1–16. http://arxiv.org/abs/2101.08103.

[67] N. Metropolis, A. W. Rosenbluth, M. N. Rosenbluth, A. H. Teller, and E. Teller, "Equation of state calculations by fast computing machines," *The Journal of Chemical Physics* **21** no. 6, (1953) 1087–1092.

[68] W. K. Hastings, "Monte Carlo sampling methods using Markov chains and their applications," *Biometrika* **57** no. 1, (Apr., 1970) 97–109. https://doi.org/10.1093/biomet/57.1.97.

[69] A. Joseph, *Markov Chain Monte Carlo Methods in Quantum Field Theories: A Modern Primer*. 2019. http://arxiv.org/abs/1912.10997%0Ahttp://dx.doi.org/10.1007/978-3-030-46044-0. Publication Title: arXiv Issue: December ISSN: 23318422.

[70] U. Wolff, "Monte Carlo errors with less errors," *Comput. Phys. Commun.* **156** (2004) 143–153. _eprint: hep-lat/0306017.

[71] B. D. Palma, M. Erba, L. Mantovani, and N. Mosco, "A Python program for the implementation of the -method for Monte Carlo simulations," *Computer Physics Communications* (2018) . http://www.sciencedirect.com/science/article/pii/S0010465518302534.

[72] C. DeTar, "Generating the quenched U(1) gauge field," Apr., 2020.

[73] R. Sommer, "Scale setting in lattice QCD," *PoS* **LATTICE2013** (2014) 015. _eprint: 1401.3270.

[74] M. Lüscher, "Properties and uses of the Wilson flow in lattice QCD," *JHEP* **08** (2010) 071. _eprint: 1006.4518.

[75] M. Luscher, "Trivializing maps, the Wilson flow and the HMC algorithm," *Commun. Math. Phys.* **293** (2010) 899–919. _eprint: 0907.5491.

[76] S. Borsanyi and others, "High-precision scale setting in lattice QCD," *JHEP* **09** (2012) 010. _eprint: 1203.4469.

[77] S. Borsanyi, Z. Fodor, J. N. Guenther, C. Hoelbling, S. D. Katz, L. Lellouch, T. Lippert, K. Miura, L. Parato, K. K. Szabo, F. Stokes, B. C. Toth, C. Torok, and L. Varnhorst, "Leading hadronic contribution to the muon magnetic moment from lattice QCD," *Nature* **593** no. 7857, (2021) 51–55.

[78] C. T. Davies, E. Follana, I. D. Kendall, G. P. Lepage, and C. McNeile, "Precise determination of the lattice spacing in full lattice QCD," *Physical Review D - Particles, Fields, Gravitation and Cosmology* **81** no. 3, (2010) 1–15.

[79] R. J. Dowdall, C. T. H. Davies, G. P. Lepage, and C. McNeile, "Vus from pi and K decay constants in full lattice QCD with physical u, d, s and c quarks," *Phys. Rev. D* **88** (2013) 074504. _eprint: 1303.1670.

[80] A. Bazavov and others, "Gradient flow and scale setting on MILC HISQ ensembles," *Phys. Rev. D* **93** no. 9, (2016) 094510. _eprint: 1503.02769.

[81] H. J. Rothe, *Lattice Gauge Theories : An Introduction (Fourth Edition)*, vol. 43. World Scientific Publishing Company, 2012.

[82] M. R. Hestenes and E. Stiefel, "Methods of conjugate gradients for solving linear systems," *Journal of research of the National Bureau of Standards* **49** (1952) 409–435.

[83] A. Frommer, "Linear systems solvers: Recent developments and implications for lattice computations," *Nucl. Phys. B Proc. Suppl.* **53** (1997) 120–126. _eprint: hep-lat/9608074.

[84] G. S. Bali, S. Collins, and A. Schafer, "Effective noise reduction techniques for disconnected loops in Lattice QCD," *Comput. Phys. Commun.* **181** (2010) 1570–1583. _eprint: 0910.3970.

[85] G. P. Lepage, "The Analysis of Algorithms for Lattice Field Theory," in *Theoretical Advanced Study Institute in Elementary Particle Physics*. June, 1989.

[86] G. P. Lepage, B. Clark, C. T. Davies, K. Hornbostel, P. B. Mackenzie, C. Morningstar, and H. Trottier, "Constrained curve fitting," *Nuclear Physics B - Proceedings Supplements* **106-107** (2002) 12–20. ISBN: 9781467300346.

[87] B. Blossier, M. D. Morte, G. V. Hippel, T. Mendes, and R. Sommer, "On the generalized eigenvalue method for energies and matrix elements in lattice field theory," *Journal of High Energy Physics* **2009** no. 4, (2009) .

[88] R. J. Dowdall, C. T. H. Davies, R. R. Horgan, G. P. Lepage, C. J. Monahan, J. Shigemitsu, and M. Wingate, "Neutral B-meson mixing from full lattice QCD at the physical point," *Phys. Rev. D* **100** no. 9, (2019) 094508. _eprint: 1907.01025.

[89] P. Lepage, "gplepage/corrfitter: corrfitter version 8.1.1," Nov., 2020. https://zenodo.org/record/4281296.

[90] C. Aubin, T. Blum, M. Golterman, and S. Peris, "The muon anomalous magnetic moment with staggered fermions: is the lattice spacing small enough?". _eprint: 2204.12256.

[91] C. T. H. Davies and others, "Hadronic-vacuum-polarization contribution to the muon's anomalous magnetic moment from four-flavor lattice QCD," *Phys. Rev. D* **101** no. 3, (2020) 034512. _eprint: 1902.04223.

[92] S. K. Choi and others, "Observation of a narrow charmonium-like state in exclusive $B^\pm \to K^\pm \pi^+ \pi^- J/\psi$ decays," *Phys. Rev. Lett.* **91** (2003) 262001. _eprint: hep-ex/0309032.

[93] B. Aubert and others, "Study of the $B \to J/\psi K^- \pi^+ \pi^-$ decay and measurement of the $B \to X(3872) K^-$ branching fraction," *Phys. Rev. D* **71** (2005) 071103. _eprint: hep-ex/0406022.

[94] A. Ali, J. S. Lange, and S. Stone, "Exotics: Heavy pentaquarks and tetraquarks," *Progress in Particle and Nuclear Physics, Vol 63, No 1* **97** (2017) 123–198. arXiv: 1706.00610 [hep-ph] Number: DESY-17-071.

[95] F.-K. Guo, C. Hanhart, U.-G. Meißner, Q. Wang, Q. Zhao, and B.-S. Zou, "Hadronic molecules," *Reviews of Modern Physics* **90** no. 1, (2018) 015004. arXiv: 1705.00141 [hep-ph].

[96] N. Brambilla, W. K. Lai, J. Segovia, J. Tarrús Castellà, and A. Vairo, "Spin structure of heavy-quark hybrids," *Physical Review D* **99** no. 1, (2019) 1–10.

[97] N. A. Campbell, A. Huntley, and C. Michael, "Heavy quark potentials and hybrid mesons from SU(3) lattice gauge theory," *Nuclear Physics B* **306** (1988) 51–62. Number: LTH 178.

[98] P. Lacock, C. Michael, P. Boyle, and P. Rowland, "Hybrid mesons from quenched QCD," *Physics Letters, Section B: Nuclear, Elementary Particle and High-Energy Physics* **401** no. 3-4, (1997) 308–312.

[99] C. Bernard, T. Burch, E. B. Gregory, D. Toussaint, C. DeTar, J. Osborn, S. Gottlieb, U. M. Heller, and R. Sugar, "Lattice calculation of [Formula Presented] hybrid mesons with improved Kogut-Susskind fermions," *Physical Review D - Particles, Fields, Gravitation and Cosmology* **68** no. 7, (2003) 1–26.

[100] Y. Ma, W. Sun, Y. Chen, M. Gong, and Z. Liu, "A Color Halo Scenario of Charmonium-like Hybrids," *arXiv* no. 1, (2019) 1–5. http://arxiv.org/abs/1910.09819.

[101] C. Bernard, T. Blum, T. A. DeGrand, C. DeTar, S. Gottlieb, U. M. Heller, J. Hetrick, C. McNeile, B. Sugar, D. Toussaint, and M. Wingate, "Hybrid mesons in quenched lattice QCD," *Nuclear Physics B - Proceedings Supplements* **60** no. 1-2, (1998) 61–64.

[102] G. K. Cheung, C. O'Hara, G. Moir, M. Peardon, S. M. Ryan, C. E. Thomas, D. Tims, and For the Hadron Spectrum Collaboration, "Excited and exotic charmonium, Ds and D meson spectra for two light quark masses from lattice QCD," *Journal of High Energy Physics* **2016** no. 12, (2016) .

[103] M. Chanowitz and S. Sharpe, "Hybrids: Mixed States of Quarks and Gluons," *Nuclear Physics B* **222** (1983) 211–244.

[104] J. J. Dudek and R. G. Edwards, "Hybrid Baryons in QCD," *Phys. Rev. D* **85** (2012) 054016. _eprint: 1201.2349.

[105] M. Creutz, "Monte Carlo Study of Quantized SU(2) Gauge Theory," *Phys. Rev. D* **21** (1980) 2308–2315.

[106] L. A. Griffiths, C. Michael, and P. E. Rakow, "Mesons with excited glue," *Physics Letters B* **129** no. 5, (1983) 351–356.

[107] S. Perantonis and C. Michael, "Static Potentials and Hybrid Mesons from pure SU(3) Lattice Gauge Theory," *Nuclear Physics B* **347** (1990) 854–868.

[108] K. J. Juge, J. Kuti, and C. J. Morningstar, "Ab Initio Study of Hybrid b gb Mesons," *Physical Review Letters* **82** no. 22, (1999) 4400–4403.

[109] X. Liao and T. Manke, "Excited charmonium spectrum from anisotropic lattices,". http://arxiv.org/abs/hep-lat/0210030.

[110] M. Peardon, J. Bulava, J. Foley, C. Morningstar, J. Dudek, R. G. Edwards, B. Joó, H. W. Lin, D. G. Richards, and K. J. Juge, "Novel quark-field creation operator construction for hadronic physics in lattice QCD," *Physical Review D - Particles, Fields, Gravitation and Cosmology* **80** no. 5, (2009) .

[111] J. J. Dudek, R. G. Edwards, N. Mathur, and D. G. Richards, "Charmonium excited state spectrum in lattice QCD," *Physical Review D - Particles, Fields, Gravitation and Cosmology* **77** no. 3, (2008) .

[112] L. Liu, G. Moir, M. Peardon, S. M. Ryan, C. E. Thomas, P. Vilaseca, J. J. Dudek, R. G. Edwards, B. Joó, and D. G. Richards, "Excited and exotic charmonium spectroscopy from lattice QCD," *Journal of High Energy Physics* **2012** no. 7, (2012) .

[113] C. Schlosser and M. Wagner, "Hybrid static potentials in SU(3) lattice gauge theory at small quark-antiquark separations," *Phys. Rev. D* **105** no. 5, (2022) 054503. _eprint: 2111.00741.

[114] A. Chodos, R. L. Jaffe, K. Johnson, C. B. Thorn, and V. F. Weisskopf, "A New Extended Model of Hadrons," *Phys. Rev. D* **9** (1974) 3471–3495.

[115] T. Barnes, "Colored Quark and Gluon Constituents in the MIT Bag Model," *Nucl. Phys. B* **158** (1979) 171–188.

[116] K. J. Juge, J. Kuti, and C. J. Morningstar, "Bag picture of the excited QCD vacuum with static QQ source," *Nuclear Physics B - Proceedings Supplements* **63** no. 1-3, (1998) 543–545. http://arxiv.org/abs/hep-lat/9709132%0Ahttp://dx.doi.org/10.1016/S0920-5632(97)00828-1.

[117] N. Isgur and J. E. Paton, "A flux tube model for hadrons in QCD," *Physical Review D* **31** (1985) 2910. Number: Print-84-0830 (TORONTO).

[118] M. Berwein, N. Brambilla, J. Tarrús Castellà, and A. Vairo, "Quarkonium hybrids with nonrelativistic effective field theories," *Physical Review D - Particles, Fields, Gravitation and Cosmology* **92** no. 11, (2015) .

[119] R. Oncala and J. Soto, "Heavy Quarkonium Hybrids: Spectrum, Decay and Mixing," *Phys. Rev. D* **96** no. 1, (2017) 14004.

[120] N. Brambilla, G. Krein, J. Tarrús Castellà, and A. Vairo, "Born-Oppenheimer approximation in an effective field theory language," *Physical Review D* **97** no. 1, (2018) 1–16.

[121] W. Chen, R. T. Kleiv, T. G. Steele, B. Bulthuis, D. Harnett, J. Ho, T. Richards, and S.-L. Zhu, "Mass Spectrum of Heavy Quarkonium Hybrids," *JHEP* **09** (2013) 019. _eprint: 1304.4522.

[122] C. McNeile, C. Michael, and P. Pennanen, "Hybrid meson decay from the lattice," *Physical Review D - Particles, Fields, Gravitation and Cosmology* **65** no. 9B, (2002) 945051–945059.

[123] J. J. Dudek, R. G. Edwards, M. J. Peardon, D. G. Richards, and C. E. Thomas, "Highly excited and exotic meson spectrum from dynamical lattice QCD," *Physical Review Letters* **103** no. 26, (2009) 2–5.

[124] C. Michael, "Quarkonia and hybrids from the lattice," *PoS* **hf8** (1999) 001. _eprint: hep-ph/9911219.

[125] P. R. Page, "Why hybrid meson coupling to two S wave mesons is suppressed," *Phys. Lett. B* **402** (1997) 183–188. _eprint: hep-ph/9611375.

[126] C. McNeile, C. Michael, and K. J. Sharkey, "Flavor singlet mesons in QCD," *Physical Review D* **65** no. 1, (2002) 145081–145086.

[127] G. Barucca and others, "PANDA Phase One," *Eur. Phys. J. A* **57** no. 6, (2021) 184. _eprint: 2101.11877.

[128] A. Hamdi, "Search for exotic states in photoproduction at GlueX," *Journal of Physics: Conference Series* **1667** no. 1, (2020) 2–6. http://arxiv.org/abs/1908.11786.

[129] R. J. Dowdall, C. T. Davies, T. C. Hammant, and R. R. Horgan, "Precise heavy-light meson masses and hyperfine splittings from lattice QCD including charm quarks in the sea," *Physical Review D - Particles, Fields, Gravitation and Cosmology* **86** no. 9, (2012) 1–19.

[130] D. Hatton, C. T. H. Davies, B. Galloway, J. Koponen, G. P. Lepage, and A. T. Lytle, "Charmonium properties from lattice QCD+QED : Hyperfine splitting, J/ψ leptonic width, charm quark mass, and a^c_μ," *Phys. Rev. D* **102** no. 5, (2020) 054511. _eprint: 2005.01845.

[131] J. J. Dudek, R. G. Edwards, and C. E. Thomas, "Exotic and excited-state radiative transitions in charmonium from lattice QCD," *Physical Review D - Particles, Fields, Gravitation and Cosmology* **79** no. 9, (2009) 1–33.

[132] E. Follana, A. Hart, C. T. Davies, and Q. Mason, "Low-lying Dirac spectrum of staggered quarks," *Physical Review D - Particles, Fields, Gravitation and Cosmology* **72** no. 5, (2005) 1–17. http://arxiv.org/abs/hep-lat/0507011%0Ahttp://dx.doi.org/10.1103/PhysRevD.72.054501.

[133] A. Bazavov, C. Bernard, C. Detar, W. Freeman, S. Gottlieb, U. M. Heller, J. E. Hetrick, J. Laiho, L. Levkova, M. Oktay, J. Osborn, R. L. Sugar, D. Toussaint, and R. S. Van De Water, "Scaling studies of QCD with the dynamical highly improved staggered quark action," *Physical Review D - Particles, Fields, Gravitation and Cosmology* **82** no. 7, (2010) 1–36.

[134] A. Bazavov, C. Bernard, J. Komijani, C. Detar, L. Levkova, W. Freeman, S. Gottlieb, R. Zhou, U. M. Heller, J. E. Hetrick, J. Laiho, J. Osborn, R. L. Sugar, D. Toussaint, and R. S. Van De Water, "Lattice QCD ensembles with four flavors of highly improved staggered quarks," *Physical Review D - Particles, Fields, Gravitation and Cosmology* **87** no. 5, (2013) 1–19.

[135] P. Boyle, A. Yamaguchi, G. Cossu, and A. Portelli, "Grid: A next generation data parallel C++ QCD library,". _eprint: 1512.03487.

[136] B. A. Galloway, *Properties of charmonium and bottomonium from lattice QCD with very fine lattices*. PhD thesis.

[137] C. Detar and S. H. Lee, "Variational method with staggered fermions," *Physical Review D - Particles, Fields, Gravitation and Cosmology* **91** no. 3, (2015) 1–21.

[138] B. Chakraborty, C. T. Davies, G. C. Donald, R. J. Dowdall, J. Koponen, G. P. Lepage, and T. Teubner, "Strange and charm quark contributions to the anomalous magnetic moment of the muon," *Physical Review D - Particles, Fields, Gravitation and Cosmology* **89** no. 11, (2014) 1–8.

[139] G. C. Donald, C. T. H. Davies, R. J. Dowdall, E. Follana, K. Hornbostel, J. Koponen, G. P. Lepage, and C. McNeile, "Precision tests of the J/ψ from full lattice QCD: mass, leptonic width and radiative decay rate to η_c," *Phys. Rev. D* **86** (2012) 094501. _eprint: 1208.2855.

[140] B. Azhothkaran and N. V. K, "Decay Constants of S Wave Heavy Quarkonia," *International Journal of Theoretical Physics* **59** no. 7, (2020) 2016–2028. Publisher: International Journal of Theoretical Physics.

[141] Y. Chen, W. F. Chiu, M. Gong, L. C. Gui, and Z. F. Liu, "Exotic vector charmonium and its leptonic decay width," *Chinese Physics C* **40** no. 8, (2016) 1–9.

[142] G. S. Bali, S. Collins, and C. Ehmann, "Charmonium spectroscopy and mixing with light quark and open charm states from nF=2 lattice QCD," *Physical Review D - Particles, Fields, Gravitation and Cosmology* **84** no. 9, (2011) .

[143] C. W. Bernard and others, "Quenched hadron spectroscopy with improved staggered quark action," *Phys. Rev. D* **58** (1998) 014503. _eprint: hep-lat/9712010.

[144] M. Luscher, "Volume Dependence of the Energy Spectrum in Massive Quantum Field Theories. 2. Scattering States," *Commun. Math. Phys.* **105** (1986) 153–188.

[145] M. Luscher, "Volume Dependence of the Energy Spectrum in Massive Quantum Field Theories. 1. Stable Particle States," *Commun. Math. Phys.* **104** (1986) 177.

[146] D. J. Wilson, R. A. Briceno, J. J. Dudek, R. G. Edwards, and C. E. Thomas, "Coupled $\pi\pi, K\barK$ scattering in P-wave and the resonance from lattice QCD," *Phys. Rev. D* **92** no. 9, (2015) 094502. _eprint: 1507.02599.

[147] Z. Fu, "Preliminary lattice study of meson decay width," *JHEP* **07** (2012) 142. _eprint: 1202.5834.

[148] Z. Fu and L. Wang, "Studying the resonance parameters with staggered fermions," *Phys. Rev. D* **94** no. 3, (2016) 034505. _eprint: 1608.07478.

[149] A. J. Woss, J. J. Dudek, R. G. Edwards, C. E. Thomas, and D. J. Wilson, "Decays of an exotic 1-+ hybrid meson resonance in QCD," *Physical Review D* **103** no. 5, (2021) 1–33.

[150] M. Dalla Brida, L. Giusti, T. Harris, and M. Pepe, "Multi-level Monte Carlo computation of the hadronic vacuum polarization contribution to (g2)," *Physics Letters, Section B: Nuclear, Elementary Particle and High-Energy Physics* **816** no. 0, (2021) . http://arxiv.org/abs/2007.02973.

[151] T. Aoyama and others, "The anomalous magnetic moment of the muon in the Standard Model," *Phys. Rept.* **887** (2020) 1–166. _eprint: 2006.04822.

[152] E.-H. Chao, R. J. Hudspith, A. Gérardin, J. R. Green, H. B. Meyer, and K. Ottnad, "Hadronic light-by-light contribution to $(g-2)_\mu$ from lattice QCD: a complete calculation,". http://arxiv.org/abs/2104.02632.

[153] B. Abi and others, "Measurement of the Positive Muon Anomalous Magnetic Moment to 0.46 ppm," *Phys. Rev. Lett.* **126** no. 14, (2021) 141801. _eprint: 2104.03281.

[154] R. M. Carey and others, "New measurement of the anomalous magnetic moment of the positive muon," *Phys. Rev. Lett.* **82** (1999) 1632–1635.

[155] G. W. Bennett and others, "Measurement of the positive muon anomalous magnetic moment to 0.7 ppm," *Phys. Rev. Lett.* **89** (2002) 101804. _eprint: hep-ex/0208001.

[156] T. Albahri, A. Anastasi, A. Anisenkov, K. Badgley, S. Baeßler, I. Bailey, V. A. Baranov, E. Barlas-Yucel, T. Barrett, A. Basti, F. Bedeschi, M. Berz, M. Bhattacharya, H. P. Binney, P. Bloom, J. Bono, E. Bottalico, T. Bowcock, G. Cantatore, R. M. Carey, B. C. Casey, D. Cauz, R. Chakraborty, S. P. Chang, A. Chapelain, S. Charity, R. Chislett, J. Choi, Z. Chu, T. E. Chupp, S. Corrodi, L. Cotrozzi, J. D. Crnkovic, S. Dabagov, P. T. Debevec, S. Di Falco, P. Di Meo, G. Di Sciascio, R. Di Stefano, A. Driutti, V. N. Duginov, M. Eads, J. Esquivel, M. Farooq, R. Fatemi, C. Ferrari, M. Fertl, A. T. Fienberg, A. Fioretti, D. Flay, E. FrleŽ, N. S. Froemming, J. Fry, C. Gabbanini, M. D. Galati, S. Ganguly, A. Garcia, J. George, L. K. Gibbons, A. Gioiosa, K. L. Giovanetti, P. Girotti, W. Gohn, T. Gorringe, J. Grange, S. Grant, F. Gray,

S. Haciomeroglu, T. Halewood-Leagas, D. Hampai, F. Han, J. Hempstead, A. T. Herrod, D. W. Hertzog, G. Hesketh, A. Hibbert, Z. Hodge, J. L. Holzbauer, K. W. Hong, R. Hong, M. Iacovacci, M. Incagli, P. Kammel, M. Kargiantoulakis, M. Karuza, J. Kaspar, D. Kawall, L. Kelton, A. Keshavarzi, D. Kessler, K. S. Khaw, Z. Khechadoorian, N. V. Khomutov, B. Kiburg, M. Kiburg, O. Kim, Y. I. Kim, B. King, N. Kinnaird, E. Kraegeloh, A. Kuchibhotla, N. A. Kuchinskiy, K. R. Labe, J. Labounty, M. Lancaster, M. J. Lee, S. Lee, S. Leo, B. Li, D. Li, L. Li, I. Logashenko, A. Lorente Campos, A. Lucà, G. Lukicov, A. Lusiani, A. L. Lyon, B. Maccoy, R. Madrak, K. Makino, F. Marignetti, S. Mastroianni, J. P. Miller, S. Miozzi, W. M. Morse, J. Mott, A. Nath, H. Nguyen, R. Osofsky, S. Park, G. Pauletta, G. M. Piacentino, R. N. Pilato, K. T. Pitts, B. Plaster, D. Počanić, N. Pohlman, C. C. Polly, J. Price, B. Quinn, N. Raha, S. Ramachandran, E. Ramberg, J. L. Ritchie, B. L. Roberts, D. L. Rubin, L. Santi, C. Schlesier, A. Schreckenberger, Y. K. Semertzidis, D. Shemyakin, M. W. Smith, M. Sorbara, D. Stöckinger, J. Stapleton, C. Stoughton, D. Stratakis, T. Stuttard, H. E. Swanson, G. Sweetmore, D. A. Sweigart, M. J. Syphers, D. A. Tarazona, T. Teubner, A. E. Tewsley-Booth, K. Thomson, V. Tishchenko, N. H. Tran, W. Turner, E. Valetov, D. Vasilkova, G. Venanzoni, T. Walton, A. Weisskopf, L. Welty-Rieger, P. Winter, A. Wolski, and W. Wu, "Measurement of the anomalous precession frequency of the muon in the Fermilab Muon g-2 Experiment," *Physical Review D* **103** no. 7, (2021) 72002. https://doi.org/10.1103/PhysRevD.103.072002. Publisher: American Physical Society.

[157] Y. Sato, "Muon g-2/EDM experiment at J-PARC," *PoS* **KMI2017** (2017) 006.

[158] S. J. Brodsky and E. de Rafael, "Suggested Boson-Lepton Pair Couplings and the Anomalous Magnetic Moment of the Muon," *Physical Review* **168** no. 5, (Apr., 1968) 1620–1622. https://link.aps.org/doi/10.1103/PhysRev.168.1620. Publisher: American Physical Society.

[159] T. Blum, "Lattice Calculation of the Lowest-Order Hadronic Contribution to the Muon Anomalous Magnetic Moment," *Physical Review Letters* **91** no. 5, (July, 2003) 052001. https://link.aps.org/doi/10.1103/PhysRevLett.91.052001. Publisher: American Physical Society.

[160] T. Blum, "Lattice calculation of the lowest order hadronic contribution to the muon anomalous magnetic moment: an update with Kogut-Susskind fermions," *Nuclear Physics B - Proceedings Supplements* **129-130** (Mar., 2004) 904–906. https://linkinghub.elsevier.com/retrieve/pii/S092056320302749X.

[161] K. G. Chetyrkin, J. H. Kuhn, and M. Steinhauser, "Three loop polarization function and O (alpha-s**2) corrections to the production of heavy quarks," *Nucl. Phys. B* **482** (1996) 213–240. _eprint: hep-ph/9606230.

[162] X. Feng, S. Hashimoto, G. Hotzel, K. Jansen, M. Petschlies, and D. B. Renner, "Computing the hadronic vacuum polarization function by analytic continuation," *Phys. Rev. D* **88** (2013) 034505. _eprint: 1305.5878.

[163] H. Horch, *Lattice QCD studies of observables extracted from the hadronic vacuum polarization*. PhD Thesis, Mainz U., Nov., 2016.

[164] D. Bernecker and H. B. Meyer, "Vector Correlators in Lattice QCD: Methods and applications," *Eur. Phys. J. A* **47** (2011) 148. _eprint: 1107.4388.

[165] C. Aubin, T. Blum, C. Tu, M. Golterman, C. Jung, and S. Peris, "Light quark vacuum polarization at the physical point and contribution to the muon g-2," *Physical Review D* **101** no. 1, (2020) 1–28. http://arxiv.org/abs/1905.09307.

[166] T. Blum, N. Christ, M. Hayakawa, T. Izubuchi, L. Jin, C. Jung, and C. Lehner, "Hadronic Light-by-Light Scattering Contribution to the Muon Anomalous Magnetic Moment from Lattice QCD," *Phys. Rev. Lett.* **124** no. 13, (2020) 132002. _eprint: 1911.08123.

[167] C. Alexandrou and others, "Lattice calculation of the short and intermediate time-distance hadronic vacuum polarization contributions to the muon magnetic moment using twisted-mass fermions,". _eprint: 2206.15084.

[168] B. Chakraborty, C. T. Davies, P. G. De Oliveira, J. Koponen, G. P. Lepage, and R. S. Van De Water, "Hadronic vacuum polarization contribution to a from full lattice QCD," *Physical Review D* **96** no. 3, (2017) 1–14.

[169] B. Chakraborty, C. T. Davies, C. Detar, A. X. El-Khadra, E. Gámiz, S. Gottlieb, D. Hatton, J. Koponen, A. S. Kronfeld, J. Laiho, G. P. Lepage, Y. Liu, P. B. Mackenzie, C. McNeile, E. T. Neil, J. N. Simone, R. Sugar, D. Toussaint, R. S. Van De Water, and A. Vaquero, "Strong-Isospin-Breaking Correction to the Muon Anomalous Magnetic Moment from Lattice QCD at the Physical Point," *Physical Review Letters* **120** no. 15, (2018) 152001. https://doi.org/10.1103/PhysRevLett.120.152001. Publisher: American Physical Society.

[170] C. T. H. Davies and others, "Windows on the hadronic vacuum polarisation contribution to the muon anomalous magnetic moment,". _eprint: 2207.04765.

[171] G. Colangelo, A. X. El-Khadra, M. Hoferichter, A. Keshavarzi, C. Lehner, P. Stoffer, and T. Teubner, "Data-driven evaluations of Euclidean windows to scrutinize hadronic vacuum polarization," *Phys. Lett. B* **833** (2022) 137313. _eprint: 2205.12963.

[172] C. Lehner and A. S. Meyer, "Consistency of hadronic vacuum polarization between lattice QCD and the R ratio," *Physical Review D* **101** no. 7, (2020) .

[173] B. Chakraborty, C. T. Davies, J. Koponen, G. P. Lepage, and R. S. Van De Water, "Higher-order hadronic-vacuum-polarization contribution to the muon g-2 from lattice QCD," *Physical Review D* **98** no. 9, (2018) 22–24. http://arxiv.org/abs/1806.08190.

[174] M. Di Carlo, M. T. Hansen, N. Hermansson-Truedsson, and A. Portelli, "Relativistic, model-independent determination of electromagnetic finite-size effects beyond the point-like approximation,". _eprint: 2109.05002.

[175] J. Bijnens, J. Harrison, N. Hermansson-Truedsson, T. Janowski, A. Jüttner, and A. Portelli, "Electromagnetic finite-size effects to the hadronic vacuum polarization," *Physical Review D* **100** no. 1, (2019) 14508. https://doi.org/10.1103/PhysRevD.100.014508. Publisher: American Physical Society.

[176] S. Borsanyi and others, "Isospin splittings in the light baryon octet from lattice QCD and QED," *Phys. Rev. Lett.* **111** no. 25, (2013) 252001. _eprint: 1306.2287.

[177] S. Basak, A. Bazavov, C. Bernard, C. Detar, L. Levkova, E. Freeland, S. Gottlieb, A. Torok, U. M. Heller, J. Laiho, J. Osborn, R. L. Sugar, D. Toussaint, R. S. Van De Water, and R. Zhou, "Lattice computation of the electromagnetic contributions to kaon and pion masses," *Physical Review D* **99** no. 3, (2019) 34503. https://doi.org/10.1103/PhysRevD.99.034503. Publisher: American Physical Society.

[178] Y. Aoki and others, "FLAG Review 2021,". _eprint: 2111.09849.

[179] J. Gasser, A. Rusetsky, and I. Scimemi, "Electromagnetic corrections in hadronic processes," *Eur. Phys. J. C* **32** (2003) 97–114. _eprint: hep-ph/0305260.

[180] D. Giusti, V. Lubicz, G. Martinelli, F. Sanfilippo, and S. Simula, "Strange and charm HVP contributions to the muon ($g - 2)$ including QED corrections with twisted-mass fermions," *JHEP* **10** (2017) 157. _eprint: 1707.03019.

[181] C. T. H. Davies, C. E. DeTar, A. X. El-Khadra, E. Gámiz, S. Gottlieb, D. Hatton, A. S. Kronfeld, J. Laiho, G. P. Lepage, Y. Liu, P. B. Mackenzie, C. McNeile, E. T. Neil, T. Primer, J. N. Simone, D. Toussaint, R. S. Van de Water, A. Vaquero, and S. Yamamoto, "The hadronic vacuum polarization of the muon from four-flavor lattice QCD," pp. 0–6. 2019. http://arxiv.org/abs/1912.04382.

[182] M. Ammer and S. Dürr, "Details of a staggered fermion data analysis," *Proceedings of Science* **363** no. June, (2019) 0–6. http://arxiv.org/abs/1910.11046.

[183] P. Lepage and C. Gohlke, "gplepage/lsqfit: lsqfit version 12.0," Aug., 2021. https://zenodo.org/record/5202760.

[184] P. Lepage, C. Gohlke, and D. Hackett, "gplepage/gvar: gvar version 11.9.3," Aug., 2021. https://zenodo.org/record/5202756.

[185] D. Hatton, C. T. Davies, G. P. Lepage, and A. T. Lytle, "Vector current renormalisation in momentum subtraction schemes using the HISQ action," in *Proceedings of Science*, vol. 363, pp. 0–6. 2019. http://arxiv.org/abs/1908.10116.

[186] B. Chakraborty, C. T. Davies, G. C. Donald, J. Koponen, and G. P. Lepage, "Nonperturbative comparison of clover and highly improved staggered quarks in lattice QCD and the properties of the ϕ meson," *Physical Review D* **96** no. 7, (2017) 1–20.

[187] S. Lahert, C. DeTar, A. El-Khadra, E. Gámiz, S. Gottlieb, A. Kronfeld, E. Neil, C. T. Peterson, and R. Van de Water, "Hadronic vacuum polarization of the muon on 2+1+1-flavor HISQ ensembles: an update," in *38th International Symposium on Lattice Field Theory*. Dec., 2021. _eprint: 2112.11647.

[188] T. Blum, P. A. Boyle, V. Gülpers, T. Izubuchi, L. Jin, C. Jung, A. Jüttner, C. Lehner, A. Portelli, and J. T. Tsang, "Calculation of the hadronic vacuum polarization contribution to the muon anomalous magnetic moment," *Phys. Rev. Lett.* **121** no. 2, (2018) 022003. _eprint: 1801.07224.

[189] D. Giusti, V. Lubicz, G. Martinelli, F. Sanfilippo, and S. Simula, "Isospin-breaking corrections to the muon magnetic anomaly in Lattice QCD," p. 063. 2020.